Design of the BGO-OD Tagging System and Test of a Detector Prototype

von
Georg Siebke

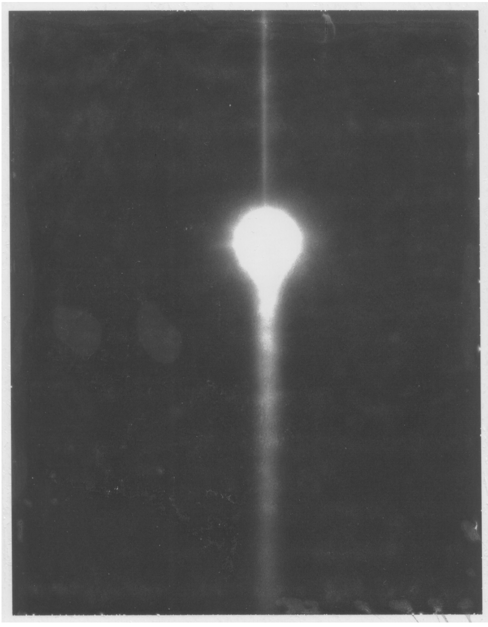

Diplomarbeit in Physik

angefertigt im
Physikalischen Institut

vorgelegt der
Mathematisch-Naturwissenschaftlichen Fakultät
der
Rheinischen Friedrich-Wilhelms-Universität Bonn

Bonn, November 2010

Das Bild auf der Titelseite zeigt ein Photo des Elektronenstrahls hinter dem Magneten der Photonenmarkierungsanlage. Siehe Kapitel 6.4.2.

Ich versichere, dass ich diese Arbeit selbständig verfasst und keine anderen als die angegebenen Quellen und Hilfsmittel benutzt sowie die Zitate kenntlich gemacht habe.

Georg Siebke

Referent: Prof. Dr. Hartmut Schmieden
Koreferent: Prof. Dr. Kai-Thomas Brinkmann

Zusammenfassung

Auch wenn das Verhalten der kleinsten bekannten Materiebausteine, der Quarks, bei hohen Energien sehr gut verstanden ist, so gibt es noch immer ungelöste Fragen auf der Ebene der Hadronen, mit Protonen und Neutronen als prominentesten Vertretern. Um deren Struktur weiter zu erforschen, wird zur Zeit das BGO-OD-Experiment am Elektronenbeschleuniger ELSA in Bonn aufgebaut. Ziel des Experimentes ist die Anregung von Nukleonen z.B. in einem Flüssigwasserstofftarget mittels hochenergetischer Photonen. Die bei dem Zerfall des angeregten Nukleons entstehenden Teilchen werden zum einen im zentralen BGO-Ball nachgewiesen, der sensitiv auf geladene und ungeladene Teilchen ist. Die Spuren von nahe der Strahlrichtung emittierten geladenen Teilchen können im Vorwärtsspektrometer gemessen werden, dessen zentrale Komponente ein offener Dipolmagnet ist. Dieser ermöglicht die Bestimmung von Ladung und Impuls der Zerfallsprodukte. Zur Erzeugung hochenergetischen Photonen wird der aus ELSA extrahierte Elektronenstrahl auf einen Radiator (z.B. aus Kupfer) gelenkt, wobei manche der Elektronen Energie in Form von *Bremsstrahlung* verlieren. Über die Messung der Elektronenenergie in einem speziellen Magnetspektrometer wird indirekt die Energie der Photonen bestimmt. Die Kombination aus Radiator, Magnet und dem *Hodoskop*, das die Elektronen im Spektrometer ortsaufgelöst nachweist, heißt *Photonenmarkierungsanlage* (Tagging-System).

Thema dieser Arbeit war die Konzeption des Hodoskops sowie die Konstruktion und der experimentelle Test eines Prototyps. Realisiert wurde das Hodoskop mit überlappenden Szintillatorstreifen, ausgelesen durch Photomultiplier. Die Grundlage für den Entwurf bildete eine Simulation zur Vorhersage der Bahnen der im Radiator gestreuten Elektronen im Magnetfeld. Mithilfe dieser Simulation ist es möglich, die *Fokalebene* des Magneten zu bestimmen. Im Idealfall wird ein Detektor in dieser Ebene installiert, da dort die Energiebestimmung der Elektronen unabhängig vom Eintrittswinkel in den Magneten ist. Aufgrund der räumlichen Gegebenheiten kann allerdings nur ein Teil des Hodoskops in der Fokalebene platziert werden. Der andere Teil wird stattdessen vertikal, annähernd senkrecht zur Fokalebene angeordnet. Dies limitiert die durch die Granularität des Hodoskops beschränkte Energieauflösung der Photonenmarkierung weiter. Bedingt durch die geringer werdende Dispersion, muss darüber hinaus an zwei Stellen in der vertikalen Ebene die Energieauflösung verschlechtert werden. Mit der Simulation dieser Detektoranordnung wird der Einfluss der Platzierung außerhalb der Fokalabene untersucht.

Der im Rahmen der Arbeit aufgebaute Prototyp umfasst neun Kanäle aus dem Vertikalteil des Hodoskops im Bereich eines Sprungs der Auflösung. Dieser Bereich wurde gewählt, da sich hier die mechanische Konstruktion am schwierigsten darstellt. Weiterhin ermöglicht die Wahl des Bereiches hoher Elektronenenergien eine Überprüfung der Ratenfestigkeit des Detektors, die wesentlich für das BGO-OD-Experiment ist. Die mechanische Konstruktion des Prototypen erlaubt es, einzelne Photomultiplier und Szintillatorstreifen auszutauschen, ohne dabei die Energiekalibration des Hodoskops zu beeinflussen. Der Prototyp wurde während zweier Tests hinter den Tagging-Magneten des CB-Experiments und des BGO-OD-Experiments untersucht. Dabei wurde gezeigt, dass eine Detektionseffizienz von 99 % und mehr erreicht werden kann und eine Rate von 50 MHz, hochgerechnet auf den gesamten Detektor, ohne signifikante Verluste möglich ist. Des Weiteren wurde die Funktion eines FPGA-Moduls getestet, das Koinzidenzen zwischen benachbarten Szintillatorstreifen erkennt und daraus ein Signal für den Trigger generiert. Der Prototyp-Detektor erfüllt die Designziele hervorragend und kann als Grundlage für den Bau des gesamten Hodoskops dienen.

Contents

List of Tables

List of Figures

1 Introduction

"Measure what is measurable,
and make measurable what is not so."
Galileo Galilei, 1564–1642

100 years ago, in 1910, Thomson proposed his atomic model in which the atom consisted of an equally distributed mass and positive charge within which the electrons moved around as particles. The charge of these electrons was shown to be opposite equal to the charge of a singly ionised atom. The prior year, 1909, Geiger and Marsden had determined that α particles impinging on a gold foil are scattered with angles larger than $90°$. In 1911, Rutherford showed that the observed rate of large angle scattering of α particles is inconsistent with Thomson's model. Instead, the mass of the atom has to be concentrated in a pointlike hard nucleus leading to the cross section $\mathrm{d}\sigma \sim \sin^{-4}(\theta/2)$, where θ is the scattering angle. Only two years later, in 1913, Bohr developed his model of the dynamics of the atom, incorporating quantum theory. Using this model it was possible to predict discrete excited electron energy states which were observed in the *spectroscopy* of hydrogen. About 50 years later, experiments done by Hofstadter showed that the cross section for the elastic scattering of electrons off gold is smaller than predicted for a pointlike nucleus. This led to the introduction of a form factor into the cross section formula, describing the charge distribution of the nucleus. The inelastic scattering of electrons off the nucleus showed that the nucleus can itself be excited and that it consists of nucleons (protons and neutrons). It did not take long to discover that the nucleons also possess excited states (like the Δ resonance) and thus are not pointlike. Eventually the nucleons were found to be made of two different *quark flavours*, the up and the down quark (today, four more quark *flavours* are known: charm, strange, top and bottom). Beside nucleons, other *baryons* are known, all made of three quarks. In addition to baryons, there are the mesons, consisting of one quark and one anti-quark. The simplest mesons, made of up and down quarks, are the pions.

All quarks come in three different *colour charges*, which are charges of the *strong interaction*. This interaction is responsible for the binding of the nucleus, too, as it consists only of positively charged protons and electrical neutral neutrons. Without the attractive force of the strong interaction between nucleons to counterbalance the electromagnetic interaction, stable nuclei could not exist. The strong interaction, however, differs from the electromagnetic interaction by an important fact: While the coupling strength α_e of the electromagnetic interaction decreases for larger distances, the coupling strength α_s of the strong interaction increases. This implies two phenomena: When looking at small distances (corresponding to a large momentum transfer Q^2), the quarks inside the nucleons are quasi free, since $\alpha_\mathrm{s} \ll 1$. This behaviour is called *asymptotic freedom*. In this region, the interaction of quarks is well understood and described within perturbative QCD, the gauge theory of the colour interaction. For distances about the size of the nucleons (small Q^2, $\alpha_\mathrm{s} > 1$), the quarks are *confined*, making it impossible to describe the excitation spectra of the nucleons within perturbative QCD. Various models have been developed to describe the excitation spectra. Not all questions have been answered. E.g., the models predict that the number of predicted excited states is much larger than the number of the observed states.

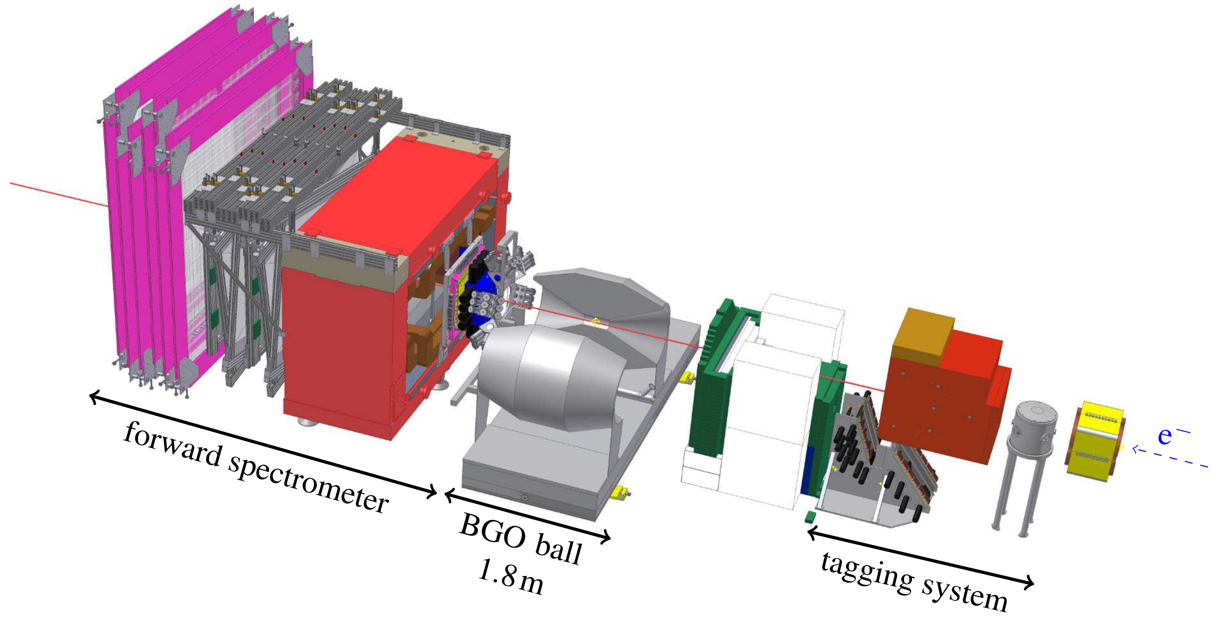

Figure 1. Overview of the BGO-Open Dipole experiment. The shown tagging detector belongs to the old SAPHIR tagging system. Based on [Wal10].

To further examine the excitation spectra of the nucleons, the BGO-OD[1] experiment (Figure 1) is currently set up at the electron stretcher accelerator ELSA in Bonn. It is funded by the DFG[2] within the Transregional Collaborative Research Centre 16: "Subnuclear Structure of Matter". To excite the nucleons, real photons of an energy of up to about 3 GeV are shot onto a liquid hydrogen or deuterium target. The decay products of the excited states are detected in a spectrometer, almost covering 4π of solid angle. The central detector, the BGO ball, is made of 480 bismuth germanate (BGO)[3] crystals. It can detect charged and uncharged particles. The forward spectrometer consists of different detectors for charged particles and the spectrometer magnet (the OD, open dipole). It is used to measure the tracks and the momenta of charged particles emitted in forward direction. The photons are produced in the *tagging system*, using the high energetic electron beam of ELSA. Figure 2 shows an overview of the electron accelerator. Unpolarised and polarised electrons are produced in the LINAC1 and LINAC2 respectively. They are then accelerated in the booster synchroton and the subsequent stretcher ring to a maximum energy of $E_0 = 3.5\,\mathrm{GeV}$. The beam can then be extracted to the BGO-OD or Crystal Barrel (CB) experiment.

Among different experiments studying similar questions, two different tagging methods are used: the Bremsstrahlung tagging and the Compton backscattering technique. For the BGO-OD experiment, Bremsstrahlung tagging is used. By shooting electrons onto a thin (about 100 µm) radiator, they are scattered and lose energy in the form of photons. The energy of the photons can be inferred through the detection of the electrons in a magnetic spectrometer. Table 1 shows an overview of different similar experiments, their tagging method, maximum photon

[1]BGO = Bismuth germanate, OD= Open Dipole
[2]Deutsche ForschungsGemeinschaft (German Research Foundation)
[3]$Bi_4Ge_3O_{12}$

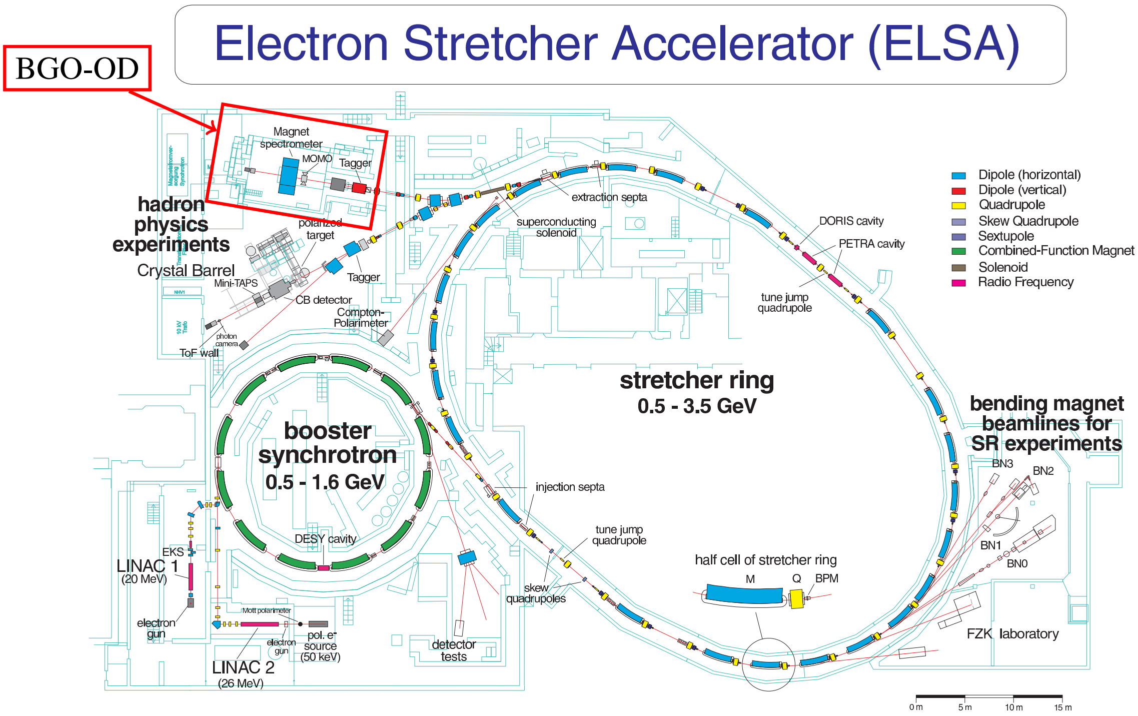

Figure 2. Overview of the Electron Stretcher Accelerator (ELSA) [els10a]. Some components of the BGO-OD experiment are missing in this picture.

energy, photon rate, and the tagged range of the photon energy. The concept of photon tagging will be described in detail in Chapter 2.4.

This thesis covers the development of the tagging hodoscope. This part of the tagging system detects the electrons which were scattered during the Bremsstrahlung process. The focus of the study is primarily on the part which detects high energetic electrons and is exposed to the highest rates. The readout electronics is developed in [Mes10]. The Bremsstrahlung target is part of [Bel10]. After describing the basics in Chapter 2, the requirements for the new tagging system are defined in Chapter 3. Based on the requirements, the general design for the detector is developed in Chapter 4. The building of a small prototype is described in chapter 5.

Experiment	Method	$E_{\gamma,\,\mathrm{max}}/\mathrm{GeV}$	$n_\gamma/\mathrm{s}^{-1}\,\mathrm{MeV}^{-1}$	$E_\gamma/E_{\gamma,\,\mathrm{max}}/\%$
CLAS (JLab) [FP09a]	Brems.	6.0	10^4	20–95
SAPHIR (ELSA) [SBB+94]	Brems.	2.8	10^3	32–93
CB (ELSA) [CMA+09]	Brems.	3.2	10^4	9–91
LEPS (SPring-8) [lep10]	Compton	2.4	10^3	60–100
GRAAL (ESRF) [BAA+97]	Compton	1.7	10^3	33–100
A2 (MAMI C) [MKA+08]	Brems.	1.5	10^5	5–93
MAX-Lab [O'R10, Bru10]	Brems.	2.0	10^5	6–90

Table 1. Properties of different photon tagging systems. n_γ is the approximate photon rate. See also [FP09a] for all entries except for MAX-Lab.

The in beam testing is presented in Chapter 6. Chapter 7 covers the analysis of the experimental data. Finally, a short summary is given in chapter 8, followed by a conclusion.

2 Basics of the Underlying Physical Processes

2.1 System of Units and Symbols

Throughout this work, the natural system of units will be used, which is defined by

$$\hbar = c = 1. \tag{1}$$

Especially during theoretical calculations, also

$$m_{\mathrm{e}} = 1 \tag{2}$$

to further simplify complex expressions. When using only the equivalence $\hbar = c = 1$,

$$[\text{energy}] = [\text{momentum}] = [\text{mass}] = [\text{length}]^{-1} = [\text{time}]^{-1} \quad (\text{MeV units}). \tag{3}$$

When also using $m_{\mathrm{e}} = 1$,

$$[\text{energy}] = [\text{momentum}] = [\text{mass}] = [\text{length}] = [\text{time}] = 1. \tag{4}$$

The following symbols will be used in this section:

$E_0,\ \mathbf{p_0}$ = initial energy and momentum of the electron
$E,\ \mathbf{p}$ = energy and momentum of the scattered electron
$k,\ \mathbf{k}$ = energy and momentum of the emitted photon
$\beta_0,\ \beta$ = velocity of incident and scattered electron; unless otherwise quoted, $\beta_0 \simeq \beta \simeq 1$
$\theta_0,\ \theta$ = angles of $\mathbf{p}_0$ and $\mathbf{p}$ with respect to $\mathbf{k}$
ϕ = angle between the planes $(\mathbf{p}_0,\ \mathbf{k})$ and $(\mathbf{p},\ \mathbf{k})$
$\mathrm{d}\Omega_k$ = element of solid angle $\sin\theta_0 \mathrm{d}\theta_0 \mathrm{d}\phi$ in the direction of $\mathbf{k}$
$\mathrm{d}\Omega_p$ = element of solid angle $\sin\theta \mathrm{d}\theta \mathrm{d}\phi$ in the direction of $\mathbf{p}$
$\mathbf{q}$ = momentum transferred to the nucleus, $\mathbf{q} = \mathbf{p}_0 - \mathbf{p} - \mathbf{k}$
θ_{MS} = RMS of the angle for multiple scattering projected onto a plane
X_0 = radiation length (for copper, $X_0 = 1.42\,\mathrm{cm}$)
α = Fine structure constant, $\alpha \simeq 1/137$

2.2 Bremsstrahlung

The process which is responsible for the emission of photons when electrons travel through material is called *Bremsstrahlung*. When an electron of momentum $\mathbf{p}_0$ traverses the Coulomb field of a nucleus, there is a certain chance for it to be scattered, leading to the radiation of a photon of momentum $\mathbf{k}$ (see Figure 3). The nucleus is needed to take the recoil momentum $\mathbf{q}$. Otherwise, this process would be kinematically impossible due to momentum and energy conservation. Only the *incoherent* Bremsstrahlung will be discussed here. In the *coherent* Bremsstrahlung process, the electrons are scattered in a crystal. The recoil momentum is then absorbed by the lattice, just as in the Mößbauer effect (see e.g. [Sie76]). The process of coherent

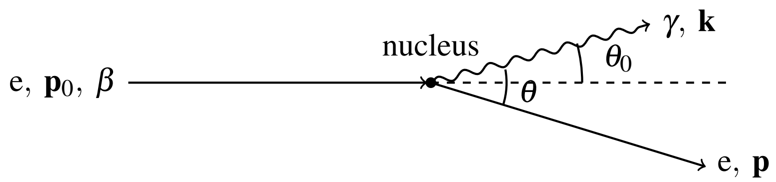

Figure 3. Kinematics of the Bremsstrahlung process. The incoming electron is scattered in the electric field of the nucleus. During the scattering process, a Bremsstrahlung photon is emitted.

Bremsstrahlung strongly depends on the orientation of the momentum transfer $\mathbf{q}$ with respect to the reciprocal lattice of the crystal. This technique can be used to produce linear polarised photons (for more details, see e.g. [EBB$^+$09, Tim69, Bel10]).

It is not useful to derive the complete quantum mechanical cross section here. A more qualitative approach will be used (see e.g. [Gre00], more details in [Jac06]).

2.2.1 Energy Distribution

Instead of viewing the electrons as incident on some material, they will be considered at rest, while the nuclei of the target material are considered to be moving with high velocity in the direction of the electrons. The electromagnetic field of the moving nuclei can be handled as a distribution of low energy photons, given by the Weizsäcker Williams distribution [Jac06] ($m_\mathrm{e} = 1$, as in all following calculations):

$$\frac{\mathrm{d}N_\gamma(k)}{\mathrm{d}k} \simeq \frac{2\alpha}{\pi}\frac{1}{\beta^2}\frac{1}{k}\left[\ln\left(\frac{2\cdot 1.123\, E\beta^2}{k}\right) - \frac{\beta^2}{2}\right]. \tag{5}$$

The nuclei have Z protons. Since the photons are soft, their phase does not change significantly within the size of the nuclei. Therefore, the amplitudes for each proton can be added coherently, leading to factor of Z^2 for the total cross section. The cross section for the scattering of a single (soft) photon off the electron is the Thomson cross section

$$\sigma_\mathrm{T} = \frac{8\pi}{3}\alpha^2. \tag{6}$$

The Bremsstrahlung cross section is then the product of the photon distribution and the Thomson cross section:

$$\mathrm{d}\sigma_k \simeq Z^2 \frac{\mathrm{d}N_\gamma}{\mathrm{d}k}\sigma_\mathrm{T}\,\mathrm{d}k, \tag{7}$$

$$\mathrm{d}\sigma_k \simeq \frac{16}{3}Z^2\alpha^3\frac{\mathrm{d}k}{k}\left[\ln\left(\frac{2\cdot 1.123\, E\beta^2}{k}\right) - \frac{\beta^2}{2}\right]. \tag{8}$$

The quantum mechanical approach in the Born approximation uses the Feynman diagrams of Figure 4. It results in the following for the cross section differential in the photon energy (extreme relativistic case, $E_0,\ E,\ k \gg 1$) [KM59]:

$$\mathrm{d}\sigma_k = 4Z^2\alpha^3\frac{\mathrm{d}k}{k}\left[1 + \left(\frac{E}{E_0}\right)^2 - \frac{2}{3}\frac{E}{E_0}\right]\left[\ln\left(\frac{2EE_0}{k}\right) - \frac{1}{2}\right]. \tag{9}$$

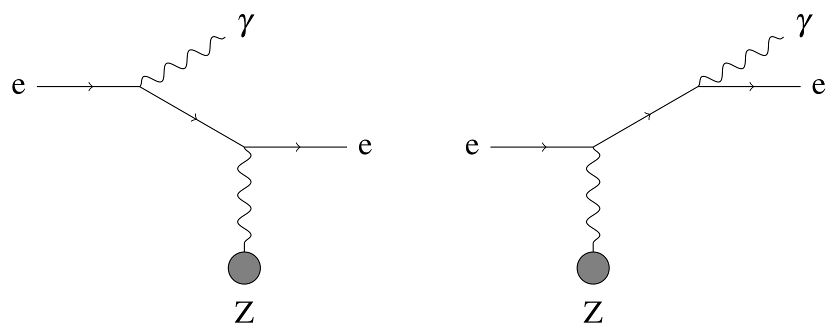

Figure 4. Feynman graphs for Bremsstrahlung.

Thus, the simple approach is very close to the more exact quantum mechanical derivation. Since the exact shape is not needed for the present work, the energy distribution will mostly be approximated by

$$\mathrm{d}\sigma_k \sim \frac{\mathrm{d}k}{k}. \tag{10}$$

2.2.2 Angular Distribution

The formula for the cross section, which is differential in photon and electron emission angles, is given in [KM59]:

$$\begin{aligned}
\mathrm{d}\sigma_{k,\theta_0,\theta,\phi} = \frac{Z^2\alpha^3}{4\pi^2}\frac{\mathrm{d}k}{k}\frac{p}{p_0}\frac{\mathrm{d}\Omega_k\,\mathrm{d}\Omega_p}{q^4}\Bigg\{ & \frac{p^2\sin^2\theta}{(E-p\cos\theta)^2}\left(4E_0^2-q^2\right) \\
& +\frac{p_0^2\sin^2\theta_0}{(E_0-p_0\cos\theta_0)^2}\left(4E^2-q^2\right)-\frac{2pp_0\sin\theta\sin\theta_0\cos\phi\left(4EE_0-q^2\right)}{(E-p\cos\theta)(E_0-p_0\cos\theta_0)} \\
& +\frac{2k^2\left(p^2\sin^2\theta+p_0^2\sin^2\theta_0-2pp_0\sin\theta\sin\theta_0\cos\phi\right)}{(E-p\cos\theta)(E_0-p_0\cos\theta_0)}\Bigg\},
\end{aligned} \tag{11}$$

$$q^2 = p^2+p_0^2+k^2-2p_0k\cos\theta_0+2pk\cos\theta-2p_0p(\cos\theta\cos\theta_0+\sin\theta\sin\theta_0\cos\phi). \tag{12}$$

Using this as a starting point, it can be derived [BLP71] that the photon and the secondary electron move forwards in a narrow cone with an apex angle

$$\delta \simeq \frac{1}{E_0}, \tag{13}$$

also called the characteristic angle. For a beam energy of $E_0 = 3200\,\mathrm{MeV}$, this means

$$\delta \simeq 0.16\,\mathrm{mrad}. \tag{14}$$

2.2.3 Limitations of the Born Approximation

The Born approximation requires that the kinetic energies of the initial and final electron are large enough to fulfil [KM59]

$$\frac{2\pi Z\alpha}{\beta_0} \ll 1, \quad \frac{2\pi Z\alpha}{\beta} \ll 1. \tag{15}$$

For $\beta_0 \simeq \beta \simeq 1$ and a radiator made of copper ($Z = 26$), $2\pi Z\alpha/\beta = 1.33$. Consequently, this approximation can be expected to deviate from the exact behaviour by a small amount.

For extreme relativistic energies, the screening of the field of the nucleus by the electrons of the atomic shell has to be taken into account. Using the atomic form factor

$$F(q,\, Z) = \frac{4\pi}{Ze}\int \rho(r)\left(\frac{\sin qr}{qr}\right) r^2 \mathrm{d}r, \tag{16}$$

where $\rho(r)$ is the electron charge distribution, the cross section formulas 9 and 11 can be corrected by simply multiplying $\mathrm{d}\sigma$ by $[1-F]^2$. Using a Thomas-Fermi model for the atom, the amount of screening can be expressed in terms of γ, defined as

$$\gamma = \frac{100k}{E_0 E Z^{\frac{1}{3}}}. \tag{17}$$

This number is close to the ratio of the radius of the atom $r_\mathrm{a} \simeq 1/(\alpha Z^{1/3})$ and the maximum impact parameter, which for relativistic energies, is $r_\mathrm{max} = q_\mathrm{min}^{-1} = (p_0 - p - k)^{-1} \simeq 2E_0E/k$. If the maximum impact parameter is much larger than the radius of the atom ($\gamma \simeq 0$), the charge of the nucleus is completely screened. If it it close to the radius of the nucleus ($\gamma \gg 0$), the complete charge Ze is seen by the electron. Assuming an incident electron energy of $E_0 = 3200\,\mathrm{MeV}$ and $5\,\%E_0 < k,\ E < 95\,\%E_0$, it follows that $3\times10^{-4} < \gamma < 0.01$, corresponding to almost complete screening. In this case, the cross section may be approximated by [KM59]

$$\mathrm{d}\sigma_k = 4Z^2\alpha^3\frac{\mathrm{d}k}{k}\left\{\left[1+\left(\frac{E}{E_0}\right)^2 - \frac{2}{3}\frac{E}{E_0}\right]\ln\left(183Z^{-\frac{1}{3}}\right) + \frac{1}{9}\frac{E}{E_0}\right\}. \tag{18}$$

2.3 Multiple Scattering

The main process responsible for deflections of incident electrons is *multiple scattering*. It is caused by many small angle scattering processes, mainly in the Coulomb field of the nuclei. Neglecting few large angle deflections, the angular distribution may be approximated as Gaussian with an RMS value which is given by [LD91]:

$$\theta_\mathrm{MS} = \frac{13.6\,\mathrm{MeV}}{p_0}\sqrt{\frac{x}{X_0}}\left[1+0.038\ln\left(\frac{x}{X_0}\right)\right]. \tag{19}$$

θ_MS is the RMS deflection angle of the scattering projected to a plane. The RMS angle in the space is given by $\theta_\mathrm{MS}^\mathrm{space} = \sqrt{2}\theta_\mathrm{MS}$. Here, x/X_0 is the thickness of the scattering medium measured in radiation lengths.

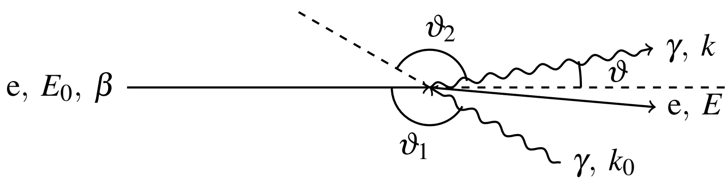

Figure 5. Kinematics of the Compton backscattering process.

2.4 Principle of Photon Tagging

As already pointed out in Section 1, there are mainly two different methods for producing highly energetic photon beams: Bremsstrahlung tagging and Compton backscattering. Both methods make use of a scattering process with accelerated electrons and for both, the scattered electron is momentum analysed to infer the photon energy and the time of production, i.e. *tag* the photon. The two methods are presented next in general terms. Then, the method of Bremsstrahlung tagging is described in more detail.

2.4.1 Methods of Photon Production

Compton Backscattering

It is possible to produce a beam of high energy photons by Compton scattering laser light against highly energetic electrons, e.g. those produced in a storage ring [BAA$^+$97, BCD$^+$90]. When laser light with energy k_0 is incident on the electron beam at an angle of about $\vartheta_1 \simeq 180°$, it is scattered backwards close to the direction of the incoming electrons. Using ϑ_2 as the angle of the scattered photon with respect to the incoming photon beam, and ϑ as the angle of the scattered photons with respect to the electron beam (see Figure 5), the energy k of the scattered photon is [DBB$^+$00]:

$$k = k_0 \frac{1 - \beta \cos \vartheta_1}{1 - \beta \cos \vartheta + (k_0/E_0)(1 - \cos \vartheta_2)}. \tag{20}$$

In the extreme relativistic case, $\beta \simeq 1,\ E_0 \gg 1,\ \vartheta_1 \simeq \vartheta_2 \simeq 180°,\ \vartheta \ll 1$, equation 20 can be approximated as

$$k = \frac{4E_0^2 k_0}{1 + 4E_0 k_0 + (E_0 \vartheta)^2}. \tag{21}$$

The energy of the scattered photon is highly dependent on the emission angle. When collimating the photon beam, it is still necessary to use a tagging method to obtain the photon energy exactly. For Compton backscattered photons, two tagging methods exist: internal and external. For internal tagging, the scattered electrons are momentum analysed by the magnets of the storage ring. The detectors are located very close to the main orbit of the storage ring. For external tagging, the scattered electrons are removed from the storage ring by an additional magnetic field and are analysed by an external tagging spectrometer, similar to the Bremsstrahlung tagging.

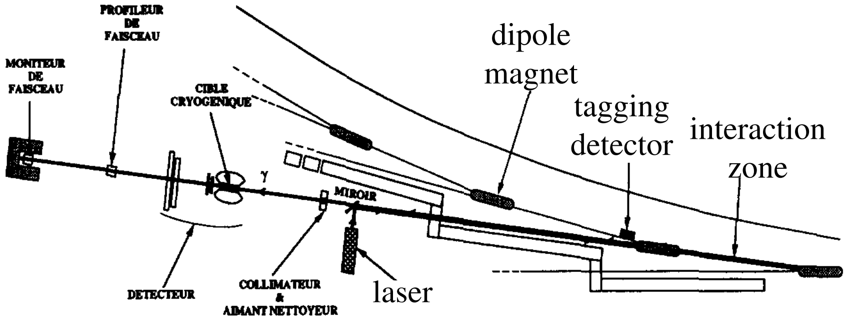

Figure 6. Layout of the GRAAL beamline [BAA+97].

The method of internal tagging is e.g. used in the GRAAL[4] experiment at the ESRF[5] in Grenoble [BAA+97] (see Figure 6). An argon laser produces photons with wavelengths of 351 nm and 514 nm. The laser photons interact with the electron beam between two bending magnets over a distance of 6.5 m. During the backscattering on the $E_0 = 6\,\mathrm{GeV}$ electrons, the photons acquire a maximum energy of $k_{\mathrm{max}} = 1.5\,\mathrm{GeV}$. The scattered electrons are deflected by the bending magnet and are separated by at most 56 mm from the electron beam. The detector for the scattered electrons is located directly after the bending magnet, at a minimum distance of 14 mm to the beam.

Bremsstrahlung Tagging

With Bremsstrahlung tagging, the electron impinges on a thin (about 100 µm) *radiator* foil made of a high Z material, e.g., copper. The electrons emit Bremsstrahlung radiation with a certain probability when traversing this foil and are then guided into the *spectrometer magnet*. Their deflection in the magnetic field depends on their energy loss during the Bremsstrahlung process. By detecting the electrons spatially resolved in the *tagging spectrometer*, their energy and thus the energy of the photons can be deduced.

There are three main differences of the photon spectra between the two methods:

(1) It is apparent from Table 1 that the photon rates achieved with Bremsstrahlung tagging are (at the present state) much higher ($10^5\,\mathrm{s}^{-1}\,\mathrm{MeV}^{-1}$) than the rates achieved with Compton backscattering ($10^3\,\mathrm{s}^{-1}\,\mathrm{MeV}^{-1}$).

(2) With Compton backscattering, is it easily possible to produce highly polarised photon beams. When using linear or circularly polarised laser light, the backscattered photon are also linear or circularly polarised. The degree of polarisation can be up to 100 % for the maximum photon energy. The maximum polarisation is in principle only limited by the polarisation of the laser beam [BAA+97].

To produce polarized photons with a Bremsstrahlung tagging system, coherent Bremsstrahlung is used. Instead of an amorphous radiator like copper, a crystal, e.g. diamond,

[4]GRenoble Anneau Accèlèrateur Laser
[5]European Synchrotron Radiation Facility

has to be used and precisely aligned with respect to the beam direction [EBB+09]. For present experiments, the maximum degree of polarisation that can be reached is about 80 %.

(3) The energy spectrum of Compton backscattered photons is rather flat, compared to the $dN_\gamma \sim dE_\gamma/E_\gamma$ shape of the Bremsstrahlung spectrum. By collimating the photon beam, low energy photons can be removed, resulting in a high energy photon beam.

For the BGO-OD experiment, the Bremsstrahlung method will be used. This method proved to work fine for all other experiments which are/were run at ELSA (e.g. CB [FP09a] and SAPHIR [Bur96]) and provides the highest photon rates. In order to switch to Compton backscattering, the acceleration facility would have to be modified, which would raise the expenses by an unacceptable amount.

2.4.2 Elements of a Bremsstrahlung Tagging System

The complete tagging system[6] consists of three distinct parts: the radiator, the tagging magnet, and the tagging hodoscope. A schematic of such a tagging system is shown in figure 7. The primary electron beam enters from the left and hits the radiator. Some electrons will undergo Bremsstrahlung and lose a varying amount of energy which depends on the cross section (see Section 2.2). The scattered electrons as well as the remaining primary beam are then deflected by the tagging magnet into the tagging hodoscope and the beam dump, respectively. Usually, the tagging magnet is simply a dipole magnet. The beam dump does not belong directly to the tagging system but is needed to stop the primary beam. For more information on the beam dump, see e.g. [Els07].

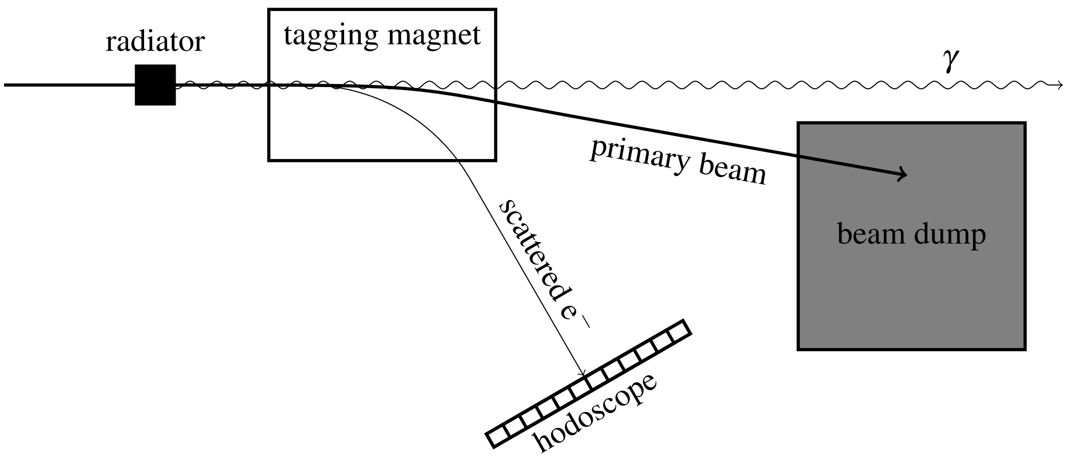

Figure 7. General scheme of a Bremsstrahlung tagging system. For a description, see the text.

[6] from this point, when referring to tagging system, it is always meant a Bremsstrahlung tagging system

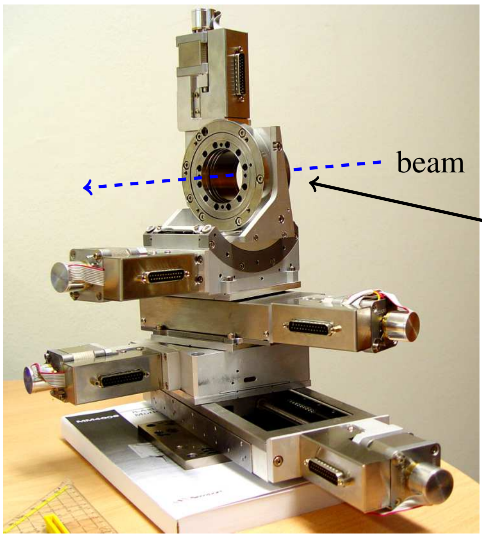

(a)

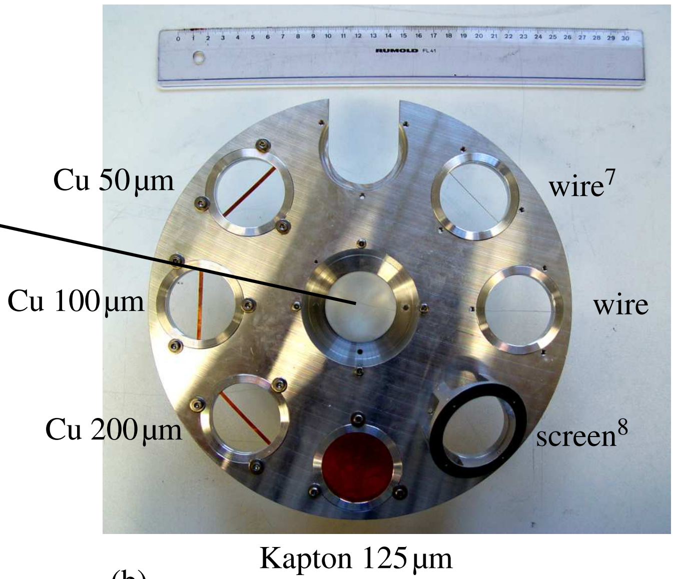

(b)

Figure 8. The Goniometer (a) and the different radiators (b). The bottom and the middle stage move perpendicular to the beam direction (horizontal and vertical). The top stage rotates the plate around the beam axis, the other two stages rotate it perpendicular to the beam axis. The radiator plate is mounted back to back onto the goniometer .

The Radiator

First, the electron beam hits the radiator. During their transit through the material, the electrons undergo Bremsstrahlung with a certain probability, resulting in a specific energetic and angular distribution (see Section 2.2). For the BGO-OD experiment, multiple different radiators and parts for beam diagnostics are mounted on a round plate sitting on a *goniometer*. A goniometer is an instrument consisting of different motorised stages, allowing for a precise positioning and alignment of the radiator plate in multiple dimensions. The high precision is mainly needed for the alignment of a diamond which is used for coherent Bremsstrahlung. Currently, a new goniometer (Figure 8 (a)), consisting of two linear and three rotation stages is installed [Bel10]. Figure 8 (b) shows the plate with the different radiators. The indicated beam direction corresponds to the use of the diamond radiator. Otherwise, one of the other radiators can be moved into the beam by the bottom linear stage and the top rotation stage.

Three different copper radiators (50 µm, 100 µm and 200 µm) will be used to generate incoherent Bremsstrahlung. Their thickness, measured in radiation lengths, is $x/X_0 = 3.5\times10^{-3}$, 7.0×10^{-3} and 14.0×10^{-3}. Horizontal and vertical wires are used to measure the profile of the electron beam. By moving them through the beam and measuring the rate of Bremsstrahlung electrons, the beam structure can be inferred. With the aid of the luminescent Chromox screen, the electron beam can be directly observed. In the centre hole, the diamond will be mounted.

[7] used for beam scans

[8] Chromox screen for an optical inspection of the beam

The Tagging Magnet

The scattered electrons are vertically deflected in the magnetic field of the *tagging magnet*. The BGO-OD experiment uses a magnet identical to the one used in the CB experiment. It is a dipole magnet from Brown-Bovery Switzerland (type MC). It can be operated with currents up to 1500 A, corresponding to a maximum field value of $B = 2.0\,\mathrm{T}$.

For each beam energy, the current in the magnet is adjusted in a way that the primary electron beam is always deflected by the same angle to enter the beam dump. For BGO-OD, this angle is $\alpha_{\mathrm{tag}} = 7.8°$[9], for CB, this angle is $\alpha_{\mathrm{tag}} = 9.0°$ [FP09a]. The effect of a constant magnetic field on relativistic particles is given by

$$\frac{\mathrm{d}\mathbf{v}}{\mathrm{d}t} = \sqrt{\alpha}\mathbf{v} \times \frac{\mathbf{B}}{E_0}. \tag{22}$$

This expression depends only on the ratio $\mathbf{B}/E_0$. As long as the magnetic field increases linearly with the current, the required current is proportional to the energy of the primary electron beam. For currents of up to 800 A, the deviation from the linear behaviour is smaller than 1 % [FP09a].

The field map of the CB tagging magnet has been measured for five different energies of the primary electron beam [Bal10]. Since the BGO-OD tagging magnet is operated with a lower magnetic field for the same energies, the field map has to be scaled accordingly using the ratio of the currents in the two magnets. This is possible at least for beam energies up to $E_0 = 2400\,\mathrm{MeV}$, because the currents are then smaller than 700 A. This is discussed in more detail in Section 4.3.

Another important feature of a dipole magnet (like the tagging magnet) is its focussing ability. Electrons which do not enter the magnet at a central axis, the z-axis, are deflected towards this axis. Hence, the magnet acts like a lens on the electron beam. One reason for this focussing is the *fringe field* of the magnet. The magnetic field inside of the magnet is almost constant in a certain range. Outside of this range, it ramps down to zero over a characteristic distance. In the absence of sources (electric currents) the following equations holds:

$$\nabla \times \mathbf{B} = \mathbf{0}, \quad \nabla \cdot \mathbf{B} = 0. \tag{23}$$

Hence, the change of one component of the magnetic field induces also a change of the other components. If the field B_0 inside of the magnet points into the y-direction, there are also finite contributions to the x and z components at the exits of the magnet [Gre00]:

$$B_x \sim -xy\left(\partial_z^2 B_y\right) \tag{24}$$

$$B_z \sim y\left(\partial_z B_y\right) \tag{25}$$

The fringe fields B_x and B_z vanish at the centre axis and focus electrons of the same energy into a small spot, the *focal point* (for more details, see [Gre00]). The plane consisting of the focal points for different electron energies is the *focal plane*. It will be calculated in Section 4.4.

The Tagging Hodoscope

Finally, the scattered and deflected electrons enter the *tagging hodoscope*. From the detected position one obtains the scattered electron's energy and thus the Bremsstrahlung photon

[9] this number is calculated from the simulation, see also Section 4.3

energy, given the primary electron energy. It is obvious that the placement of the hodoscope into the focal plane of the tagging magnet increases the energy resolution. There are different possible detectors to detect the deflected electrons:

(1) Scintillation counters using plastic scintillator and photomultiplier tubes offer a fast and precise measurement of the timing of incoming electrons. Plastic scintillators can have a rise time of about 0.5 ns, photomultiplier tubes have a transit time of some ns and a jitter of $\Delta t \simeq 0.5\,\mathrm{ns}$ [Leo94]. It is easily possible to manufacture plastic scintillator bars in the desired sizes down to certain limit, given by the size of the PMTs and the required light output.

(2) In contrast to scintillation counters, MWPCs[10] offer a high spatial resolution of 100 µm and smaller [Gre00]. However, the timing resolution is not suitable to be used as reference. Assume a wire spacing of 2 mm and a drift velocity of $10\,\mathrm{cm\,\mu s^{-1}}$. Then, the time between the transit of the electron and the arrival of the ionisation electrons at the anode, where most of the gas amplification takes place, can differ by $\Delta t \simeq 1\,\mathrm{mm}/10\,\mathrm{cm\,\mu s^{-1}} = 10\,\mathrm{ns} \gg \Delta t_{\mathrm{PMT}}$. It is, however, possible to use a MWPC and scintillation counter together and measure position and time separately. This method was used for the SAPHIR tagging system TOPAS II [Bur96].

(3) Detectors making use of Čerenkov radiation are very fast, since the light is emitted almost instantaneously when the electron traverses the material. This light can be detected using PMTs. The downside is that these detectors have to be rather big to maintain a sufficient light output, which strongly affects the spatial resolution. A lead glass Čerenkov detector is for example employed in the CB Møller Polarimeter [Kam10].

For the BGO-OD tagging system, the first method is chosen. The use of a combined system of an MWPC and large scintillator bars limits the maximum electron rate which can be detected, because each single PMT sees a substantial fraction of the total rate and the MWPC already saturates at small rates. When using smaller scintillator bars, the total rate can be increased. At the same time, the spatial resolution of the scintillator bars can be improved sufficiently, so no additional position resolving detector is needed. A positive side effect is the lower cost of a single detector compared to a combined system. To further increase the resolution at the low photon energy limit, one can think of an additional scintillating fibre detector as used for the CB tagging system [FP09a].

2.5 Detector Components

The functionality of plastic scintillator and photomultiplier tubes (PMTs) is explained in more detail in this section.

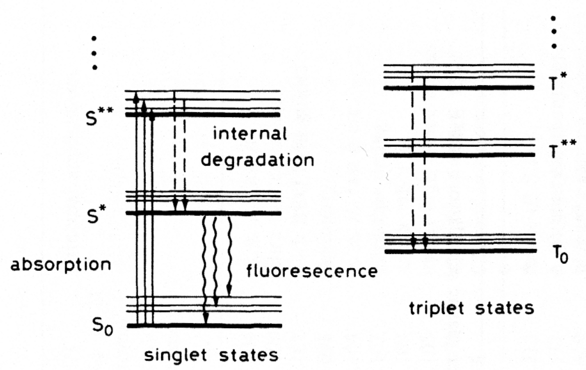

Figure 9. Energy level diagram of an organic scintillator molecule [Leo94].

2.5.1 Scintillators

A plastic scintillator is actually an organic scintillator dissolved in a plastic solvent. Common solvents are PS[11] and PVT[12].

A charged particle traversing through plastic scintillation material deposits ionisation energy in the solvent. This energy is transferred very quickly to the actual scintillator, e.g. p-Terphenyl[13], PBD[14] and PBO[15]. The scintillator gets excited to a triplet state (T^*, T^{**}, …) or to a singlet state (S^*, S^{**}, …) (see Figure 9). These states all decay to the S^* state via *internal degradation*, without emitting radiation. The S^* state decays radiatively with a high probability to a vibrational state of S_0. Since the energy of the radiated photon is smaller than the distance between S_0 and S^*, the scintillator is transparent to its own radiation. Usually, a secondary scintillator like POPOP[16] is added to shift the wavelength of the radiation to a more suitable value in the visible range (about 420 nm [Gre00]).

The light output of a scintillation material, i.e. the number of emitted photons, is typically measured relative to the light output of anthracene (an organic crystal). In anthracene, an electron loses in average $\varepsilon_{\mathrm{ant}} \simeq 60\,\mathrm{eV}$ per emitted photon. The light output of plastic scintillators lies around 60 % of anthracene, so that $\varepsilon_{\mathrm{pl}} \simeq 100\,\mathrm{eV}$ [Leo94].

2.5.2 Photomultiplier Tubes

A photomultiplier tube (PMT) is a device which is able to convert very faint light pulses (down to single photons) into an electric signal. A simple layout is shown in Figure 10. After the photons pass through the input window (faceplate), they hit the photocathode. Due to the photoelectric effect, photoelectrons are emitted. The probability for a single photon to produce

[10] Multi Wire Proportional Chambers

[11] PolyStyrene, trichloro(nitro)methane, CCl_3NO_2 [che10]

[12] PolyvinylToluene, 1-ethenyl-2-methylbenzene; 1-ethenyl-3-methylbenzene; 1-ethenyl-4-methylbenzene, C_{27}H30 [che10]

[13] 1,4-di(phenyl)benzene, $C_{18}H_{14}$ [che10]

[14] 2-phenyl-5-(4-phenylphenyl)-1,3,4-oxadiazole, $C_{20}H_{14}N_2O$ [che10]

[15] 1-pyridin-3-ylbutan-1-on, $C_9H_{11}NO$ [che10]

[16] 5-phenyl-2-[4-(5-phenyl-1,3-oxazol-2-yl)phenyl]-1,3-oxazole, $C_{24}H_{16}N_2O_2$ [che10]

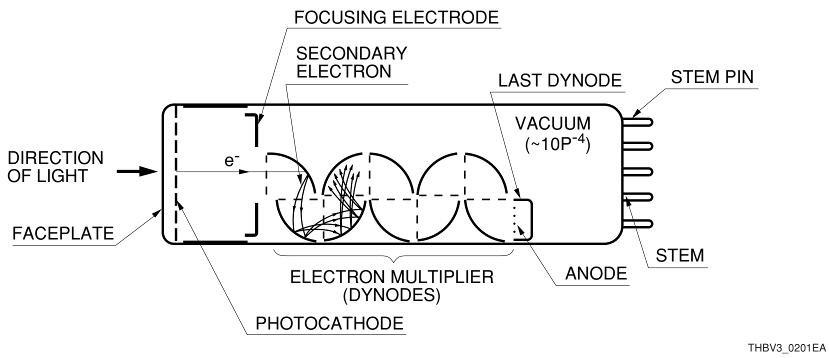

Figure 10. Construction of a Photomultiplier Tubes [Ham07].

an electron is called the quantum efficiency. The quantum efficiency depends strongly on its wavelength. The maximum quantum efficiency is typically about 25 %. Next, *dynodes* are connected to different high voltages in a way that the voltage increases along the flight path of the electrons. This way, the electrons from the photocathode are accelerated until they hit the first dynode and produce more free electrons. This is repeated several times, until the electrons are collected at the anode. The total gain or multiplication of the PMT is the number of output electrons divided by the number of photons. Gains of about 10^7 can be achieved. There are other kinds of dynode layouts, but the amplification principle is the same for all PMTs. Because the gain depends strongly on the focussing of the electrons onto the dynodes, already weak magnetic field can lead to a decrease of gain by distorting the flight path of the electrons. To shield the PMT from external magnetic fields, a layer of high permeable metal, e.g. Mumetal[17], can be wrapped about the tube. This shielding should be longer as the PMT itself and exceed the photocathode by at least the radius of the shielding [Ham07].

The dynode voltages are usually obtained with a simple voltage divider circuit which is connected to a single high voltage source (about 0.5 kV–2 kV). The combination of the socket which holds the PMT and the voltage divider is called a *socket assembly*. It has at least two connections, the high voltage input and the signal output.

2.5.3 Light Collection and Efficiency

Because the shape of the scintillator generally differs from the shape of the PMT window, they cannot be connected together directly. Instead, a light guide, often made of PMMA[18], is put between them. If properly designed, the light is totally reflected inside of the light guide with the result that the light is efficiently transferred from the scintillator to the PMT. The critical angle θ_c for total reflection has to be kept in mind when designing the shape of such a light guide. If a kink exist that has a smaller angle than θ_c, some photons will escape the light guide.

[17] a nickel-iron alloy with a very high magnetic permeability $\mu > 50000$
[18] Poly(methyl methacrylate), e.g. "Plexiglas"

The efficiency of a complete scintillation counter (PMT and scintillator bar) is determined by the number of electrons that finally reach the anode of the PMT. The efficiency depends on different parameters of all three components. This is illustrated in the following example. The density of a plastic scintillator is roughly $\rho = 1\,\mathrm{g/cm^3}$. For a scintillator thickness of $x = 0.5\,\mathrm{cm}$, the mean energy deposit of a minimum ionising particle (MIP) is $\Delta E = 2\,\mathrm{MeV g/cm^2} \cdot x\rho = 1\,\mathrm{MeV}$, corresponding to 10^4 scintillation photons ($\varepsilon = 100\,\mathrm{eV}$). Because the light is emitted isotropically, only a fraction of the photons are emitted in a direction that is totally reflected. This fraction is

$$\frac{\Delta\Omega}{4\pi} = \int_0^{2\pi} \mathrm{d}\phi \int_0^{90^\circ-\theta_\mathrm{c}} \mathrm{d}\theta \sin\theta = \frac{1}{2}(1-\sin\theta_\mathrm{c}) \simeq 0.2, \tag{26}$$

for plastic with $\theta_\mathrm{c} = 39^\circ$. Further photons are lost in the light guide if the cross section of the scintillator bar A is bigger than the cross section of the area A' which is coupled to the PMT. Then, at most A'/A photons are transmitted [Leo94]. For a scintillator width of $2\,\mathrm{cm}$ (the thickness is $0.5\,\mathrm{cm}$) and a diameter of the photo cathode of $8\,\mathrm{mm}$, the ratio A'/A is approximately 0.5, and about $10^4 \cdot 0.2 \cdot 0.5 = 1000$ photons will reach the PMT. With a mean quantum efficiency of $\sim 10\,\%$, about 100 electrons will be released in the photocathode. This number fluctuates statistically, but the probability that none or only a few electrons are produced is close to zero. Hence, in most cases a detectable electric signal will be generated, implying an efficiency of the scintillation counter close to $100\,\%$.

In this example, the loss of light in the coupling between light guide and scintillator and PMT respectively was neglected. For wavelengths larger than $350\,\mathrm{nm}$ the transmission of different cyanoacrylate glues and silicone is close to $100\,\%$, so in most cases no light is lost [Leb02]. More photons can however be lost if the emission spectrum of the scintillator and the transmission spectrum of light guide and the window of the PMT do not match up. Furthermore, a flawed, or non polished surface of the scintillator and the light guide, as well as air between the different components (e.g. in the glue film), leads to additional losses, which potentially lead to an efficiency smaller than $100\,\%$. Moreover, electrons which hit only an edge of the scintillator will produce less photons in the first place and are detected with a lower efficiency.

3 Requirements of the BGO-OD Tagging System

Several aspects have to be considered when designing the tagging system for the BGO-OD experiment. The experiment itself makes demands on the energy resolution and the precision of the timing. An additional emphasis is placed on a straightforward and easily maintainable system, as the tagging system has to be always completely ready for operation. The largest constraint for the detector design is the spatial situation. Only a limited amount of space is available between the tagging magnet and the beam dump.

3.1 Spatial Restrictions

The arrangement of the tagging magnet and the beam dump could only be changed by a major rebuilding of the experimental site and therefore provides a fixed restriction for the design of the tagging system. Figure 11 shows a drawing of the tagging magnet and the beam dump, the latter constituting the main spatial restriction. The magnet is oriented in a way such that the electrons entering from the left are deflected towards the ground. As explained in Section 4.4, its focal plane is almost parallel to the bottom side and lies closely below it. That implies that the focal points for high energetic electrons lie within the beam dump or even beyond, so that only a part of the tagging hodoscope can be placed into the focal plane. The remaining part has to be located in front of the beam dump, above the focal plane. Electrons which lost only a small amount of energy during the Bremsstrahlung process will be very close to the primary beam at this distance to the magnet, as both the scattered electrons and the primary beam are deflected by nearly the same angle.

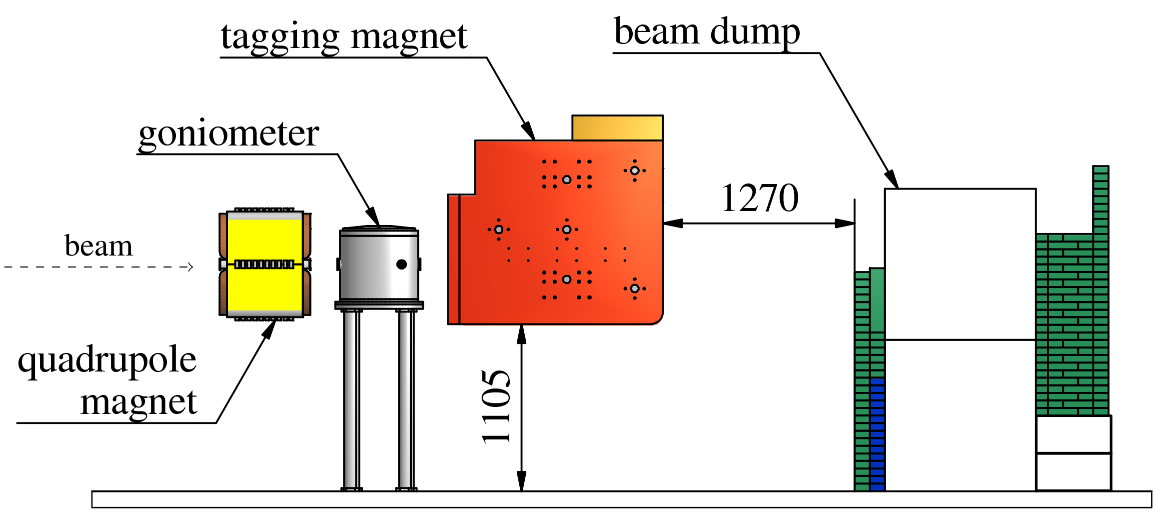

Figure 11. Side view of the available space for the tagging system. The electron beam enters from the left. Distances are given in mm (scale 1:50). Based on [Wal10].

3.2 Energy Range and Resolution

Ideally, the tagged energy range should be as large as possible to cover a maximum photon energy range for a single energy of the primary beam. It is still possible to deactivate single channels when a higher amount of high energetic photons is needed and the extracted electron current is increased. The channels for the low energetic photons may then saturate due to the larger rate ($\mathrm{d}\sigma \sim \mathrm{d}E_\gamma/E_\gamma$) and therefore are not used in this case.

At the small electron energy end, the range is limited by the dimensions of the magnet. Very low energetic electrons are deflected so strongly that they do not leave the magnet and cannot be detected. At the high electron energy end, the range is limited due to the primary beam. The primary beam must not hit the hodoscope under any circumstances, but has to fly into the beam dump. If it hits parts of the detector, it will illuminate the complete system due to the large amount of multiple scattering, simply because of the huge intensity compared to the electrons which underwent Bremsstrahlung. To maximise the range towards this end, the mechanical construction should not exceed the detector channel which is closest to the primary beam.

Besides other factors, e.g. the condition of the primary beam, the energy resolution of the hodoscope is limited by the physical width of the scintillator bars. The smaller the bars are, the better is the spatial resolution and thus the energy resolution. The *energy width* ΔE_γ is defined as the span which is covered by one detector channel, so that photons between $E_\gamma \pm \Delta E_\gamma/2$ cannot be distinguished. For a beam energy of $E_0 = 3200\,\mathrm{MeV}$, an energy width between $20\,\mathrm{MeV}$ ($0.6\,\%E_0$) and $50\,\mathrm{MeV}$ ($1.5\,\%E_0$) is targeted. The actual resolution σ_{E_γ} is different from ΔE_γ and does not only depend on geometrical factors. This is explained in more detail in Section 4.6.

3.3 Rate Stability and Timing

To provide enough statistics for the BGO-OD experiment, the tagging system has to be able to tag photons with a rate of at least $n_\mathrm{full} = 10\,\mathrm{MHz}$ over the complete energy range without significant losses. This is roughly the rate which could be achieved with other tagging systems at ELSA. Since only a small fraction of the photons produced in the radiator leads to an interesting interaction in the target, even higher rates of $n_\mathrm{full} = 50\,\mathrm{MHz}$ or more are desirable to further improve the situation. For example, the total cross section for the reaction $\gamma\mathrm{p} \to \Sigma^+\mathrm{K}^0$ is at most $\sigma_\mathrm{tot} \simeq 0.5\,\mu\mathrm{b}$ for a photon energy around $E_\gamma \simeq 1400\,\mathrm{MeV}$ [Ewa10]. About $5\,\%$ of all tagged photons have an energy between $1300\,\mathrm{MeV}$ and $1500\,\mathrm{MeV}$, assuming that all photons between $10\,\%E_0$ and $90\,\%E_0$ are tagged. Using a liquid hydrogen target of $x = 2\,\mathrm{cm}$ length ($\rho = 0.07\,\mathrm{g\,cm^{-3}}$), the reaction rate is

$$n \simeq \sigma_\mathrm{tot}\,\rho\,x\frac{N_A}{A}\cdot 5\,\%\,n_\mathrm{full} \simeq 0.02\,\mathrm{s}^{-1}, \tag{27}$$

where N_A is the Avogadro constant and $A = 1\,\mathrm{g\,mol^{-1}}$ is the atomic weight of hydrogen. Hence, at a tagging rate of $50\,\mathrm{MHz}$, there will be only roughly one reaction per minute in the specified energy range, justifying the need for as high tagging rates as possible.

Due to the geometrical composition of the hodoscope, the differences in the time of flight for electrons of different energies are small and can be precisely predicted, as they all move approximately at the speed of light. If the transit time in the scintillator and the PMT fluctuates only by a small amount, it is possible to calibrate the timing of the tagging system very accurately. This turns the tagging system into a suitable candidate for the timing reference of the complete experiment, since the time when the Bremsstrahlung photon hits the target is calculated easily.

3.4 Maintenance

The different components of the tagging system undergo an ageing process when they are irradiated. After some years of operation, scintillators lose their ability to produce light and PMTs lose gain and become defective. If this happens, a certain energy range will not be tagged and a significant part of the total rate will be lost. Hence, it is important to assure a reliable operation of the tagging system and to exchange the particular part. This should be possible without changing the position of any other part and destroying the energy calibration [FP09a] of large parts of the complete system. Therefore, the hodoscope is designed in a way that enables to easily exchange single photomultiplier tubes and scintillator bars easily without disturbing other parts.

3.5 Background

The function of the tagging hodoscope is to detect the scattered electrons from the Bremsstrahlung process in the radiator, but not any other particles like for example neutrons which are backscattered from the beam dump [Els10b] and electrons which are scattered in the beam pipe.

To see the influence of backscattered neutrons, their detection efficiency is estimated. Since neutrons are not charged, their detection requires a hadronic interaction, mainly elastic scattering off protons. The cross section for elastic n-p scattering at $1\,\mathrm{MeV}$ is $\sigma \simeq 4\,\mathrm{b}$ and decreases for higher energies. The density of H-atoms per volume in plastic is $n \simeq 5 \times 10^{22}/\mathrm{cm}^3$, leading to a mean free path

$$L = \frac{1}{n\sigma} \simeq 5\,\mathrm{cm}. \tag{28}$$

For a thickness of $x = 40\,\mathrm{mm}$, as used for the SAPHIR tagging system TOPAS II [Bur96], the probability for a reaction is then $1 - \exp(-x/L) \simeq 55\,\%$. The recoil proton will produce scintillation light and the neutron will be detected. To reduce the neutron detection efficiency, the scintillator bars of the BGO-OD tagging system only have a thickness of $x = 5\,\mathrm{mm}$, reducing the reaction probability to approximately $10\,\%$. Together with the coincidence technique described below, the detection efficiency is smaller than $1\,\%$.

To reduce the efficiency for charged particles not involved in the Bremsstrahlung process, the scintillator bars are arranged at least half overlapping as in Figure 12. Electrons coming from the radiator will always hit two adjacent scintillator bars, while this is only the case for a part of the background electrons. Since electrons are detected with almost $100\,\%$ efficiency,

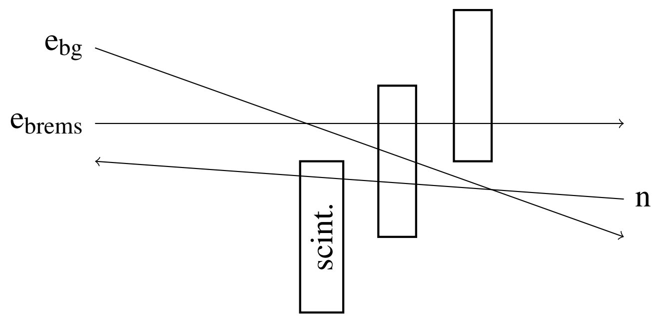

Figure 12. Function of overlapping scintillator bars. Bremsstrahlung electrons (e_{brems}) always hit the scintillator bars perpendicularly, background electrons (e_{bg}) may come from different directions. Neutrons (n) come out of the beam dump and go into the opposite direction.

only coincidences of two scintillator bars are counted. For neutrons, the detection efficiency is much lower, and the probability that one neutron induces a signal in two scintillator bars is even smaller, namely 1 % as estimated above.

3.6 Selected PMTs and Scintillator

Two different photomultiplier tubes are used for the tagging system: the Hamamatsu R7400U and the ET Enterprises 9111SB. Table 2 shows their most important properties. The R7400U was chosen because of its fast response, its compatibility for high rates [FP09b] and its small dimensions. It features a transit time delay of $\delta t_H = 5.4\,\mathrm{ns}$ with a spread of $\sigma t_H = 0.23\,\mathrm{ns}$. Thus, it is used for the low photon energy part, where rates are the highest and the scintillator bars are the smallest. The 9111SB has a slightly bigger outline and larger transit time delay of $\delta t_E = 15\,\mathrm{ns}$ with a spread of $\sigma t_H = 1.2\,\mathrm{ns}$. It is therefore used for the higher photon energies and lower rates. Both PMTs are sufficiently insensitive to magnetic fields, the R7400U due its dynode structure and the 9111SB due to a shielding with Mumetal. As socket assembly the Hamamatsu E5780 and the ET Enterprises E673ASN2 are used. Both are designed for use with a negative high voltage.

As scintillator, the Saint-Gobain BC-404[19] (see table 3) was chosen. It has a short rise time of 0.7 ns, comparable to the rise time of the R7400U, and thus allows for a very fast counting. Another possible choice was the BC-418[20], offering an even better timing. However, the substantial larger costs of the BC-418 did not justify this small benefit.

[19] equivalent to EJ-204 and NE-104
[20] equivalent to EJ-228 and Pilot-U

quantity	R7400U	9111SB
outline:		
diameter/mm	15.9	26.5
length/mm (w/o connector)	11.5	43
spectral response:		
range/nm	300–650	280–630
peak wavelength/nm	420	350
photocathode:		
material	bialkali	bialkali
quantum efficiency at peak	n/a	28 %
active diameter/mm	8	22
window material	borosilicate glass	borosilicate glass
dynodes:		
structure	metal channel	circular focussed
number of stages	8	10
maximum ratings:		
anode to cathode voltage/V	1000	1500
average anode current/mA	0.1	0.1
typical nominal characteristics:		
voltage/V	800	800
gain	7×10^5	7×10^5
anode sensitivity/$\mathrm{A\,lm^{-1}}$	50	50
timing:		
rise time/ns	0.78	1.8
transit time/ns	5.4	15
transit time spread/ns	0.23	1.2

Table 2. Properties of the Hamamatsu R7400U and the ET Enterprises 9111SB PMT [Ham04, ET 09].

quantity	BC-404
general:	
base	polyvinyltoluene
density/$\mathrm{g\,cm^{-3}}$	1.032
refractive index	1.58
scintillation properties:	
light output/%anthracene	68
rise time/ns	0.7
decay time/ns	1.8
pulse width, fwhm/ns	2.2
wavelength of max. emission/nm	408
light attenuation length/cm	140

Table 3. Properties of the Saint-Gobain BC-404 plastic scintillator [Sai05].

4 Detector Design

The design of the new tagging system is developed in two steps. First, the optimum arrangement of the single scintillation counters, without regarding the mechanical construction, is calculated in this chapter. The next chapter covers the actual mechanical design of a prototype detector, made to test the design before the complete hodoscope is built.

Due to the spatial limitations and the two types of photomultiplier tubes, the tagging hodoscope will consist of three different areas:

(1) The *focal plane detector* will be located almost parallel to the bottom side of the tagging magnet. Aside from the calculation of the focal plane itself, the construction of the hodoscope for this area will be easier than the design of the remaining detector, due to the large space which is available for each channel. This will be shown in section 4.4, where the focal plane is calculated. The focal plane detector will be built using the ET 9111SB PMT.

(2) The *vertical plane detector* will be located to the front side of the beam dump. The size of the scintillator bars is decreasing when going from the bottom in direction of the primary beam, whereas the electron rate increases. So, for the lower part of the vertical plane detector, the slightly larger ET 9111SB PMT will be used.

(3) The upper part of the vertical plane detector is exposed to the highest rates and needs small scintillator bars to achieve the desired resolution. This makes the Hamamatsu R7400U best suitable for this part.

In the next section, the software tools which are needed for the computation of the focal plane and other calculations are presented (Section 4.1). After introducing some general definitions (Section 4.2), the setup of the employed simulation is explained (Section 4.3). After the calculation of the focal plane in Section 4.4, the focus is laid on the design of the upper part of the focal plane detector, which is the most challenging problem. For this area, it is especially important to provide an easy maintenance because the probability for a failure increases with the electron rate impinging on the detector. For the remaining parts of the detector, the design can probably be adapted and simplified.

4.1 Software Tools

A lot of the calculations in this chapter rely on simulations to predict electron trajectories in the magnetic field of the tagging magnet. For all the simulations, the Explora package [SAA10] is used. The software provides functions to analyse experimental and simulated data and is able to simulate physical scenarios. The instructions for Explora are written in XML[21] files. One can access the various functions by using different XML tags. Each XML tag is based on one

[21] Extensible Markup Language

class[22] in the source code of Explora which is written in C++. This design makes it easy to extend Explora by additional modules (see Section 4.3).

The underlying simulation is not provided by Explora itself, but it can access the GEANT4 and the VMC Monte Carlo engines. VMC (Virtual Monte Carlo) [HAB+03] is an approach to make it easy to use different simulation engines without changing the complete source code. At the moment, it supports GEANT3 [CER93] and GEANT4 [AAA+03] and provides a unified interface for defining particles, detector layout and all other parameters. To swap the Monte Carlo engine, one has only to change one parameter. The implementation makes strong use of the ROOT framework [BR97], which simplifies the sharing of complex data between the VMC configuration and other programs using ROOT.

All programs which are used in this section are written in C++/ROOT or BASH script[23]. For all steps of the design in this section, ROOT scripts were coded. These can be used to repeat the calculations and simulations with different parameters, e.g. a different energy width. Only very few things have to be done manually.

4.2 General Remarks

To simplify the subsequent considerations, some general definitions and remarks are made in the following paragraphs.

Coordinate System

Independent of the orientation of the tagging magnet (which is different for CB and BGO-OD), the z-axis is defined by the direction of the incoming electron beam. The x-axis lies in the plane in which the electrons get deflected by the tagging magnet, perpendicular to the z-axis. The y-axis is chosen accordingly to get a right-handed coordinate system (see figure 13 (a)).

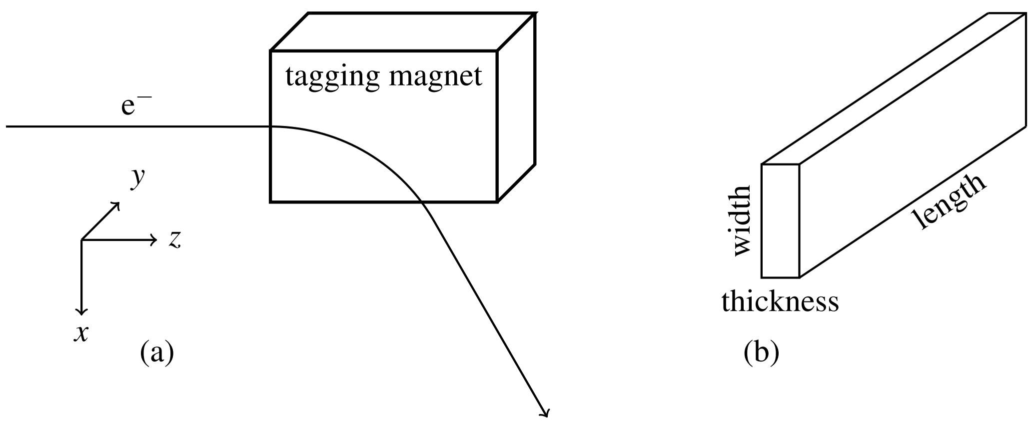

Figure 13. (a) Coordinate system used in the simulation. (b) Dimensions of scintillator bars.

[22] a construct in OOP (Object-oriented Programming) languages like C++ or Java
[23] Bourne-Again SHell, a command language interpreter

Scintillator Dimensions

The dimensions of the scintillator bar will be called as in Figure 13 (b). The *thickness* is given by the dimension of the material. The *width* and the *length* can be chosen in a wide range.

Beam Flaw

In the best of cases, all electrons enter the tagging magnet at the same point and their tracks are parallel to each other. To begin with, the electron beam hitting the Bremsstrahlung radiator is not perfect. It shows a finite spot size, and an angular divergence, due to the magnetic optics in the external beam line and due the emittance. The spot size is the geometrical size of the electron beam on the plane perpendicular to the direction of motion. It is approximated by the Gaussian widths σ_x^{spot} and σ_y^{spot} in vertical and horizontal direction. The angular divergence is defined by the Gaussian widths σ_x^{div} and σ_y^{div}. Approximate values for these properties are taken from [Els07], see there for more details.

When the electron beam hits the radiator, it undergoes further angular deflections due to multiple scattering, whereas the spot size is not influenced. All these deviations from the perfect beam will be summarized as *beam flaw*. Since also the angles for multiple scattering are approximated Gaussian (see equation 19), the resulting angular divergence is given by the quadratic sum of the beam divergence before hitting the radiator and the multiple scattering RMS angle. The beam properties calculated for the different radiators are shown in Table 4.

radiator	$\sigma_x^{\text{spot}}/\text{mm}$	$\sigma_y^{\text{spot}}/\text{mm}$	$\sigma_x^{\text{div}}/\text{mrad}$	$\sigma_y^{\text{div}}/\text{mrad}$	$\theta_{\text{MS}}/\text{mrad}$
no radiator	1.0	1.5	0.08	0.30	0.0
Cu 50 µm	1.0	1.5	0.26	0.39	0.25
Cu 100 µm	1.0	1.5	0.37	0.47	0.36
Cu 200 µm	1.0	1.5	0.51	0.58	0.50

Table 4. Beam spot size and angular divergence.

Channel

The term *channel* is used in two different meanings. On the one hand, a channel corresponds to a single scintillator bar and PMT. On the other hand, a channel refers to a temporal coincidence of two (or three) neighbouring scintillator bars, corresponding to a single electron energy. To avoid misunderstandings, the former will be called *s-channel* (single), the latter will be called *c-channel* (coincident).

4.3 Simulation of the Magnetic Field of the Tagging Magnet

To calculate the focal plane and to site the different s-channels, the electron trajectories for different energies have to be known. These can be calculated using a simulation of the tagging magnet. The simulation requires the measured field components of the used dipole magnet. Such a measurement was done for the CB tagging magnet [Bal10] for different primary beam energies (E_0 =1.6 GeV, 2.4 GeV, 2.6 GeV, 3.2 GeV and 3.5 GeV). As described in Section

2.4.2, the tagging magnet of the BGO-OD experiment is of the same type as the CB tagging magnet, but is driven with a smaller current. To get the according field for the BGO-OD tagging magnet, the measured values have to be scaled. For $E_0 = 2.4\,\mathrm{GeV}$, the current in the CB tagging magnet is $I_{\mathrm{CB}} = 669.62\,\mathrm{A}$, the current in the BGO-OD tagging magnet is $I_{\text{BGO-OD}} = 579.90\,\mathrm{A}$ [Fro10]. So all measured values for the magnetic field have to be multiplied by

$$c = \frac{I_{\text{BGO-OD}}}{I_{\mathrm{CB}}} = 0.8660 \tag{29}$$

to fit the BGO-OD tagging magnet. For higher beam energies, the magnetic field does not increase linearly with the current in the magnet, so that c will deviate from the ratio of the two currents. The simulations in this chapter all base on the field map for $E_0 = 3.2\,\mathrm{GeV}$, without scaling. Energies will always be quoted as fraction of E_0 and as an absolute number valid for $E_0 = 3.2\,\mathrm{GeV}$, e.g. $E = 10\,\%E_0$ $(320\,\mathrm{MeV})$.

To extract the electron trajectories from the simulation, virtual sensitive planes are placed below and behind the tagging magnet. When an electron hits one of these planes, information about its momentum $\mathbf{p}$ and its position $\mathbf{x}_0$ is stored. Using this information, the trajectory can be extrapolated easily for positions $\mathbf{x}$ at which the magnetic field can be neglected:

$$\mathbf{x} = \mathbf{x}_0 + l\mathbf{p}, \tag{30}$$

l being an arbitrary number (positive or negative). Figure 14 shows the general setting of the simulation. The magnet itself, the beam dump and the ground are only displayed for a better understanding, they are not implemented as real matter but as vacuum. Only the magnetic field and the two detector planes are considered in the simulation. The magnetic field is implemented by an already existing plugin for Explora. To model the beam properties, an additional plugin had to be created. This plugin can be configured to fit the particular needs by adjusting the following parameters:

startpoint: defines the point at which the electron is created. It is set to the position of the radiator.

phi, *theta*: define the direction of the electron in polar coordinates.

dphi, *dtheta*: define the beam divergence. To apply theses parameters, the vector $\mathbf{d}$ which defines the electron's direction is first rotated about $\mathbf{v} = \mathbf{d} \times \mathbf{e_z}$ by an angle α into the $x - y$ plane ($\mathbf{e_z}$ is the unit vector in z-direction). For this to work, *theta* must be different from 0 by an amount which can yet be negligible. $\mathbf{d}$ is then modified by adding random numbers to ϕ and θ. The random numbers follow a Gaussian distribution with $\sigma = dphi$ and $\sigma = dtheta$, respectively. After this transformation, $\mathbf{d}$ is rotated back by $-\alpha$ about $\mathbf{v}$.

dx, *dy*: define the size of the beam spot in x and y direction.

n: the number of electrons.

brems, *uniform*: Boolean values which define if the energy of the electrons is distributed according the Bremsstrahlung cross section $\mathrm{d}\sigma \sim \mathrm{d}E_\gamma / E_\gamma$ or if it is uniformly distributed.

interval: defines the energy range of the simulated electrons. If neither *brems* nor *uniform* is set, the energy for all electrons is set to the lower edge of the interval.

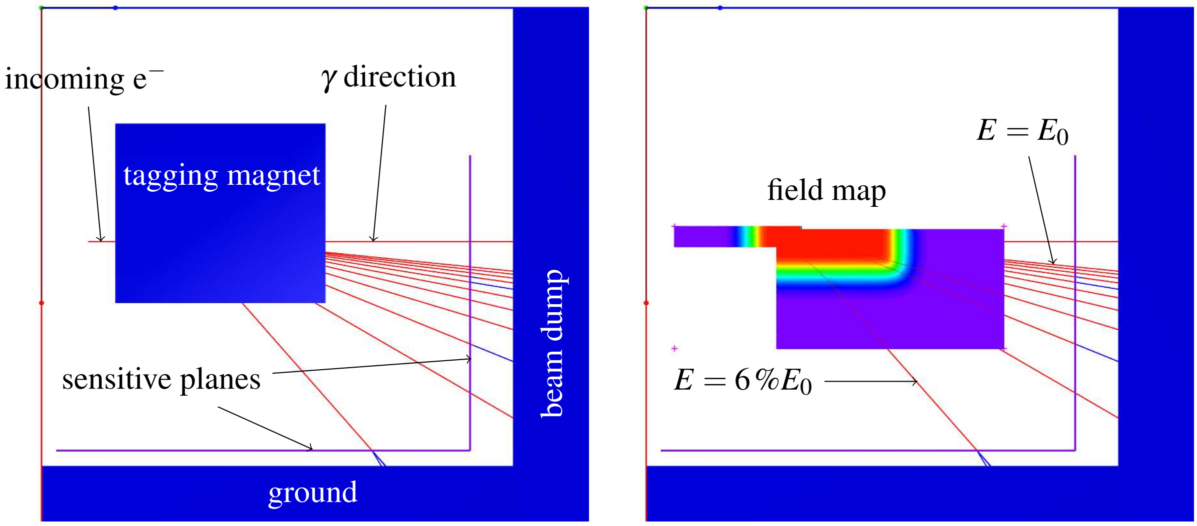

Figure 14. Overview of the setting for the simulation. The bent red tracks represent electrons with energies between $6\,\%E_0$ (200 MeV) and $100\,\%E_0$ (3200 MeV) with steps of $9\,\%E_0$ (300 MeV). The coloured area on the right picture shows the measured magnetic field, red $\simeq 1.6$ T (for $E_0 = 3200$ MeV), purple $\simeq 0$ T.

To simulate an electron moving in z-direction $phi = 0$ and $theta = -1 \times 10^{-13}$ is chosen. With these settings, $dphi$ has the meaning of a horizontal divergence, whereas $dtheta$ has the meaning of a vertical divergence.

4.4 Focal Plane

As explained in Chapter 2.4.2, the tagging magnet focusses electrons of the same energy into a small spot. To calculate the focal point for a single electron energy E, an electron beam of energy E with the properties given in Table 4 (no radiator) is simulated. This test beam consists of n electrons e_i whose angle and parallel offset is distributed according to the beam properties and a single centre electron e_c without beam flaw (see Figure 15). For each electron e_i, the distance $d_i(l_c)$ to the centre electron track $\mathbf{x}_c = \mathbf{x}_{0,c} + l_c \mathbf{p}_c$ is calculated, depending on l_c. The distance is measured perpendicular to $\mathbf{x}_c$, as in Figure 15, but it has to be taken into consideration that the figure only shows the projection of the scenario onto a plane parallel to $\mathbf{x}_c$. In fact, the distance projected onto the $x - z$ plane (the plane of the Bremsstrahlung electrons) is used here instead of the spatial distance. This way, the focussing in y direction is not taken into account.

Now, the *beam width* $w(l_c)$ is defined as

$$w(l_c) = \sqrt{\frac{1}{n}\sum_{i=1}^{n}(d_i(l_c))^2}, \tag{31}$$

the RMS of all distances to the centre track. The focal point $\mathbf{x}_{\text{focal}}$ is then found easily by means of minimizing $w(l_{\text{c}})$ with respect to l_{c},

$$\mathbf{x}_{\text{focal}} = \mathbf{x}_{0,\text{c}} + l_{\text{c,min}}\, \mathbf{p}_{\text{c}}. \tag{32}$$

Using this method, the focal points for energies between $E = 9.4\,\%E_0$ (300 MeV) and $E = 43.8\,\%E_0$ (1400 MeV) with steps of $\Delta E = 1.6\,\%$ (5 MeV) have been calculated. For smaller energies, electrons move into parts of the magnet without measured field values, for higher energies, the electrons already hit the beam dump before being focussed. The simulated focal plane is indicated in Figure 16.

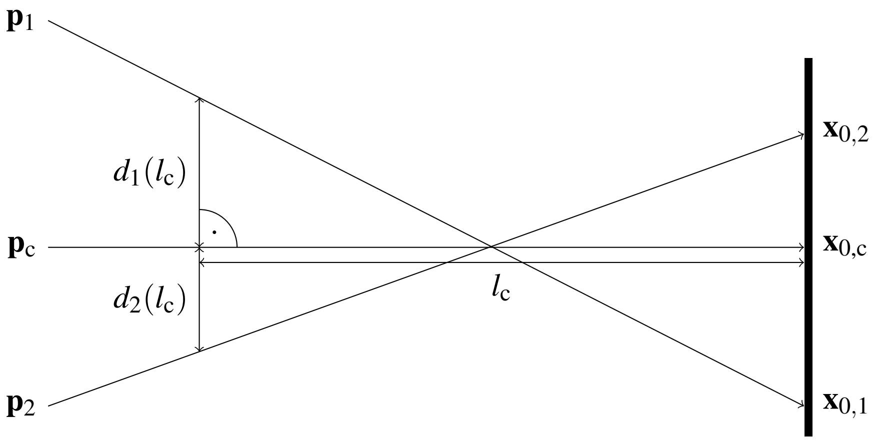

Figure 15. Calculation of the beam width. $\mathbf{p}_{\text{c}}$, $\mathbf{x}_{0,\text{c}}$ and $\mathbf{p}_i$, $\mathbf{x}_{0,i}$ are the momenta and the positions on the sensitive plane of the centre electron and the deflected electrons, respectively. l_{c} is the distance to the sensitive plane, $d_i(l_{\text{c}})$ are the distances perpendicular to the centre track.

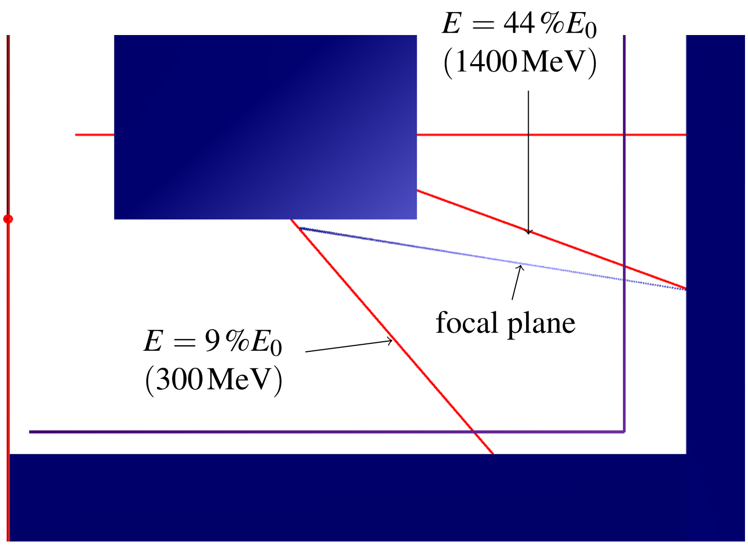

Figure 16. Simulated focal plane. The red tracks indicate electrons. The blue line indicates the position of the focal plane which is calculated using the simulation.

4.5 Calculation of the Detector Geometry

As already mentioned before and shown in Figure 16, only a part of the complete detector can be placed into the focal plane. Therefore, the high energy range of the detector must be placed in a vertical plane. Because the spatial distance between two electrons of energy E and $E + \delta E$ becomes smaller when going to higher electron energies (see Figure 14), the space which is available for the physical scintillation counters also becomes smaller. This makes it difficult to place the scintillator bars in the vertical plane detector where the widths of the bars could become smaller than the diameter of the photomultiplier tubes. The next two subsections cover this in more detail. First, the outline and the alignment of the scintillator bars relative to each other will be discussed, then the composition of the complete detector will be presented.

4.5.1 Alignment of the Scintillator Bars

The width of the scintillator bars defines the energy resolution of the detector. Up to a limit which arises from the beam flaw, a smaller width leads to a better resolution (see also Section 4.6). The easiest way to build the detector would be to use scintillator bars of a fixed width over a certain energy range. Using a simple setup which either uses no overlap of neighbouring scintillator bars or a strict overlap of always exactly two scintillator bars (Figure 17) would lead to a non-constant energy width ΔE for each c-channel, since the spatial distance between two electrons with a constant energy range (the *dispersion*) becomes smaller for higher electron energies. This arrangement leads to two issues: Due to the Bremsstrahlung cross section $d\sigma \sim dE/(E_0 - E)$ (E is the energy of the Bremsstrahlung electron), the electron rate increases when the energy becomes larger. The rate seen by a single scintillator bar increases even more due to the fact that the dispersion becomes smaller at the same time. When using a (small) scintillator width which would work at high energies, the total number of channels would be too large. The second problem of this simple approach is that each c-channel would have a different energy width ΔE, making it more difficult to analyse the data which will be measured later.

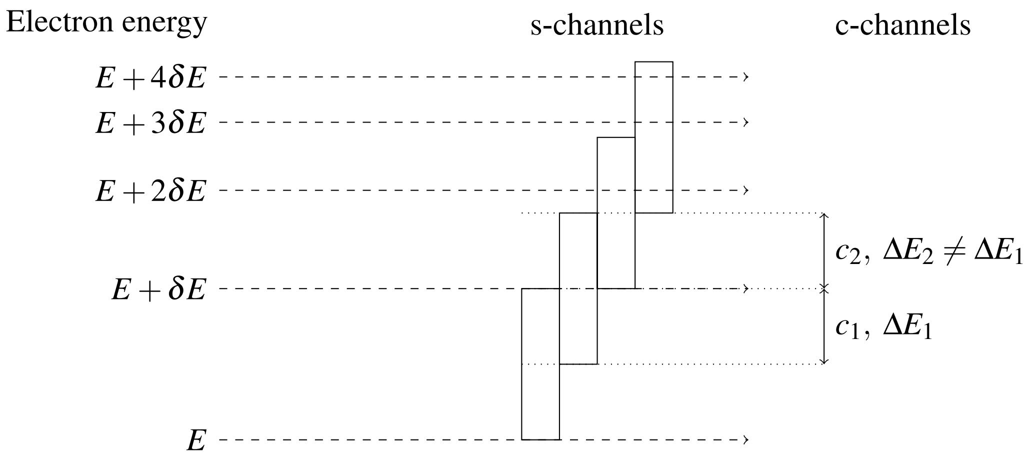

Figure 17. Exemplary electron trajectories for equidistant energies (distance $= \delta E$) and scintillator bars. The c-channels c_i are defined by the overlap of two scintillator bars.

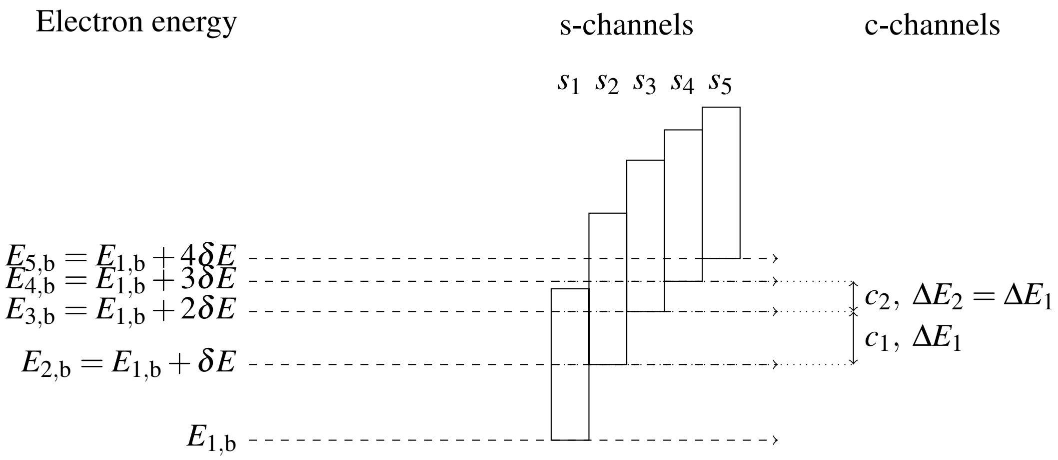

Figure 18. Exemplary electron trajectories for equidistant energies and adjusted positions of the scintillator bars. The corresponding s-channels are called $s_1 - s_5$. The c-channel c_1 is defined by the overlap of the s-channels s_1 and s_2 while there is no overlap with s_3. The energy of c_1 lies between $E_{2,\mathrm{b}}$ and $E_{3,\mathrm{b}}$.

The other extreme and probably the best solution would be to use a different width for each scintillator bar, calculated to exactly match a constant energy width of the c-channels. The problems of this method arise from the manufacturing process. First, each scintillator had to be produced individually with a high precision. Secondly, one needs spare parts of the detector for a fast repair without waiting for the production of new parts. This would imply that at least twice the number of scintillator bars had to be produced since each of them is different.

The solution chosen for the BGO-OD tagging system lies in between. As mentioned above, a design using coincidences of two neighbouring detectors will be used. Starting with the second example, every scintillator bar would have another width if it exactly fits the same energy width for all energies. The trick performed here is to match only the bottom side (to low energies) of each scintillator bar s_i to a fixed energy $E_{i,\mathrm{b}}$ (see Figure 18). The width of the scintillator bar has then to be at least large enough that also electrons with $E = E_{i,\mathrm{b}} + \Delta E$ hit it. The energy of a c-channel is now not only defined by the struck s-channels, but also by the next s-channel which was not struck. If, e.g, an electron hits s_1 and s_2, but not s_3, the energy of this electron lies between $E_{2,\mathrm{b}}$ and $E_{3,\mathrm{b}}$. If also s_3 is hit, the energy lies between $E_{3,\mathrm{b}}$ and $E_{4,\mathrm{b}}$. Using this technique leads to a bit more complicated assignment of the s-channels to the c-channels, but with the benefit of a constant energy width $\Delta E = \delta E$.

So far, one problem remains: When all scintillator bars have the same width, more than two or three scintillator bars will overlap for high energies (see Figure 18). To circumvent this, the width of the scintillator bars is adjusted roughly to match ΔE. Multiple consecutive scintillator bars have the same width, until the overlap becomes too large. Then a new group of scintillator bars with a smaller profile is used. This is accomplished by increasing the width in steps of 1 mm. To make sure that each electron hits at least two s-channels, a minimum spatial overlap of 10 % between three scintillator bars is used.

Using this method, one benefits of the advantages of both ways: On the one hand, multiple scintillators of the same size can be used, simplifying the manufacturing, on the other hand,

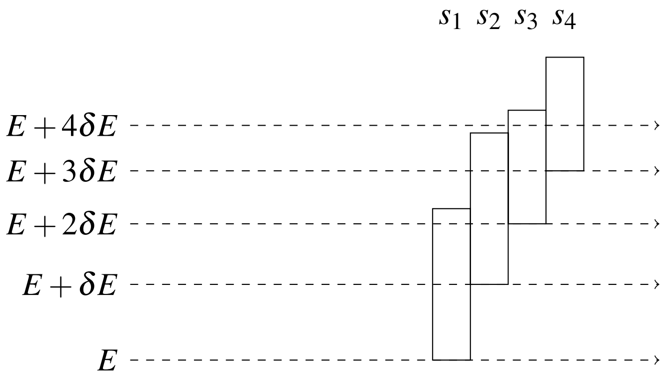

Figure 19. Exemplary electron trajectories for equidistant energies and adjusted positions and widths of the scintillator bars. The corresponding s-channels are called $s_1 - s_4$. s_1 and s_2 have the same width, as well as s_3 and s_4.

a constant energy width can be maintained. For now, the layout of the arrangement of the scintillator bars is depicted in figure 19. One possible problem arises by this layout: Multiple electrons which are close in energy and time may be identified falsely or lost. This will be examined in the next section.

4.5.2 Multiple Hits

The layout using an overlap of three scintillator bars can produce ambiguous patterns of struck s-channels if two (or more) electrons hit the hodoscope. If the temporal distance between two electrons is smaller than the time which the detectors and the electronics can resolve, the electrons cannot be distinguished. This is not a problem as long as these electrons hit distant s-channels, but if two or more electrons hit nearby s-channels, there is a certain probability that these electrons cannot be identified correctly. Only the case of two electrons will be looked at here, because the probability for more than two electrons in near s-channels is sufficiently low as will be shown later. There are several possibilities for such misidentifications which depend on the chosen detector layout: When using a layout with exactly half overlapping scintillator bars, only electrons whose energy corresponds to the same c-channel lead to an error, as only one of them will be detected. If two electrons hit neighbouring c-channels, they can be distinguished correctly. It is different if the scintillator bars are more than half overlapping, since now a single electron can hit either two or three s-channels (see Figure 20 (a)). The same pattern of s-channels can be produced by two coincidental electrons (Figure 20 (b)) which would not be the case without the larger overlap.

Furthermore, the triple overlap leads to patterns of hit s-channels which cannot be associated reliably to the correct c-channels, even when it is evident that more than one electron is detected, see figure 20 (c) and (d). Four s-channels are hit, implying that more than one electron hit the detector. For two electrons, there are two possible origins: one electron in c-channel 4 and one in c-channel 3 or one electron in c-channel 4 and one in c-channel 2. C-channel 4 is correctly identified in both situations. A similar situation occurs when five neighbouring s-channels are hit. With six or more s-channels, the situation is no longer ambiguous, seven or more s-channels are not possible using only two electrons.

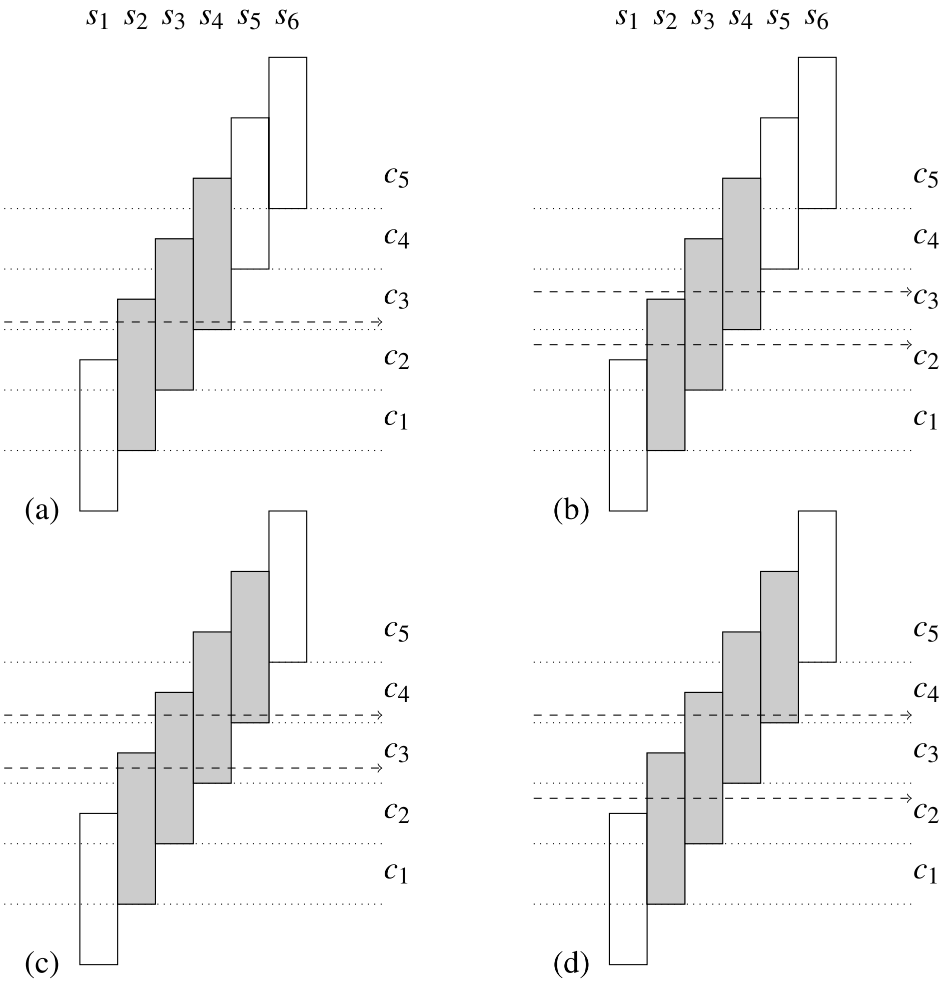

Figure 20. Possibilities for multiple electron events. The scintillator bars are all pictured with the same size to simplify the graphic. The dashed lines represent electron tracks. The c-channels c_1 to c_5 are defined by the dotted lines. Struck scintillator bars are coloured grey. (a) A single electron hits three s-channels. (b) The same pattern as in (a) can be produced by electrons of adjacent c-channels. (c) Two electrons from adjacent c-channels can hit four s-channels. (d) The same pattern can be produced by two electrons which do not come from adjacent c-channels.

To decide which c-channels have to be reconstructed from a certain number of adjacent s-channels, the probabilities are estimated that a certain reconstruction is valid. At the same time, this shows how many electrons are expected to be lost due to false reconstruction. For this estimation, the additional overlap l (in addition to the half overlap) divided by the width d of the scintillator bar is assumed to be the same for all bars: $p = l/d = \text{const}$. The other parameter is the probability t that in addition to the first electron a second electron comes in one specific c-channel, e.g. in the same c-channel as the first electron. The estimation works as follows: The total rate of electrons between $63\,\%E_0$ $(2000\,\mathrm{MeV})$ and $94\,\%E_0$ $(3000\,\mathrm{MeV})$ is assumed to be about $10\,\mathrm{MHz}$ and constant for all energies, neglecting the real shape of the Bremsstrahlung cross section. The temporal resolution of the electronics is estimated by $10\,\mathrm{ns}$, which is rather pessimistic. This leads to a mean of 0.1 electrons per time span of $10\,\mathrm{ns}$, called event throughout this section. Therefore, the probabilities for one and two electrons in one event, given by a Poisson distribution $P(N) = (0.1^N/N!)\exp(-0.1)$, are 0.090 and 0.005, respectively. Assuming an energy width of $\Delta E = 1.6\,\%$ (50 MeV), according to 20 c-channels, t is given by $t = 0.005/(0.090 \cdot 20) \simeq 0.003$. Using these parameters, the probability p_{ni} that a pattern of n neighbouring s-channels originates in a specific combination i of c-channels can be calculated. Instead of showing the complete derivation which is rather long but simple, only the results are shown here. They are summarized in table 5. For each number of neighbouring s-channels which are hit at the same time (within the time resolution), the different possible origins are given. For example, three neighbouring s-channels can be hit by a single electron (Figure 20 (a)), by two electrons of the same c-channel or by two electrons from neighbouring c-channels (Figure 20 (b)). In place of the complete expression for each probability p_{ni}, the ratio of the probabilities for a single pattern of neighbouring s-channels is given. This makes it easy to read off the most probable origin.

Clearly, an event with two or three neighbouring s-channels belongs to a single electron with almost unit probability. If the additional overlap p of the scintillator bars is not larger than approximately 0.6, four and five neighbouring hits correspond to the same combination of c-channels. This information can be used when reconstructing the c-channels of real events, as the energy of the electrons is not known a priori.

One interesting quantity is the probability that an event is indeed reconstructed correctly. As $t \ll 1$, this will be calculated only for the case that two electrons are reconstructed as separated by one intermediate c-channel (for 4 and 5 neighbouring s-channels, see Table 5). The probability P that this reconstruction is in fact correct is:

$$P = \frac{1}{1+p} \tag{33}$$

In the present case, p lies between $p = 0.1$ and $p = 0.3$, meaning $0.77 \lesssim P \lesssim 0.91$. So, in at most 23 % of these two electron events, one electron is not reconstructed correctly. Instead, it is associated to a neighbouring c-channel. Therefore, an additional error of $\Delta E = 1.6\,\%$ (50 MeV) is introduced for this second electron. The electron with the higher energy is always identified correctly, as its energy is defined by the first s-channel which is not hit (see Section 4.5.1). This effect is incorporated in the simulation of the energy resolution, see Section 4.6.

no. of neighbouring s-channels	possible origins[a]	ratio of probabilities	most probable origin[a]
2	1 : 0	$\frac{t}{1-t}(1-p) : 1$	0 ($t \ll 1$)
3	2 : 1 : 0	$\frac{t}{1-t}(1-p^2) : \frac{t}{1-t}(2p-p^2) : p$	0 ($t \ll 1$)
4	3 : 2	$(1-p) : p^2$	3 (for $p \lesssim 0.6$)
5	4 : 3	$(1-p) : 1$	3

[a] 0: single electron; 1: two electrons in the same c-channel; 2: two electrons in adjacent c-channels; 3: two electrons, separated by one intermediate c-channel; 4: two electrons, separated by two intermediate c-channels

Table 5. Probabilities for different multi-hit events.

4.5.3 Complete Detector Layout

The focal plane has enough space to place all scintillator bars in an optimum position, i.e. in the focal points, while maintaining enough space to place the PMTs. More challenging is the *vertical plane detector*. If the scintillator bars were simply placed one above the other, they would physically overlap even without the enlarged width discussed before. For this reason, they have to be staggered in more than one vertical plane. A higher number of planes allows for a higher number of s-channels in the same energy range, because the spatial distance between the single channels decreases, thus leading to a better energy resolution. On the other hand, as the distance in flight direction also increases, multiple scattering in the first struck scintillator bar can change the electrons' directions and increases the possibility that they hit a scintillator bar which does not lie in the original direction.

For the alignment of all scintillator bars in the focal plane, as well as in the vertical plane, a ROOT-program was created which automates this process. First, it places as many scintillator bars as possible into the focal plane. When the distance to the beam dump gets too small, the program starts to build the vertical plane. After placing the first scintillator bar, it is checked if there is enough space to place the second bar directly above it (Figure 21 (a), the dotted bar). If this is does not work, the second scintillator bar is placed in a second vertical plane behind the first one (closer to the beam dump). Now, the same check is done for the third scintillator bar. If there is enough space, it is placed above the first one, otherwise it is placed in a third vertical plane (b). The procedure is repeated until the next scintillator bar fits into the first vertical plane (c). The complete staggering procedure is then iterated until the full energy range is covered. The energy width ΔE and the energy range as well as the minimum distance between the edges of two scintillator bars can be adjusted. The latter has to be chosen appropriately to leave enough space for the placement of the photomultiplier tube. Furthermore, the minimum overlap between three consecutive scintillator bars and the increment in the scintillator width can be set (see Section 4.5.1).

When starting with a energy width of $\Delta E \simeq 0.6\,\%E_0$ $(20\,\mathrm{MeV})$ for low energies, the total number of planes increases up to six (see Figure 22 (a)). This is clearly too high, as a large number of planes complicates the mechanical construction and increases the impact of multiple scattering in the scintillator. To reduce this number, the energy width is enlarged at two points, leading to a jump in the width of the scintillator bars. This way the number of planes can be reduced to three (see Figure 22 (b)). The complete layout is shown in Figure 22 (c). Starting from $\Delta E \simeq 0.6\,\%E_0$ $(20\,\mathrm{MeV},\,\text{for}\,E_0 = 3200\,\mathrm{MeV})$, the energy width is in-

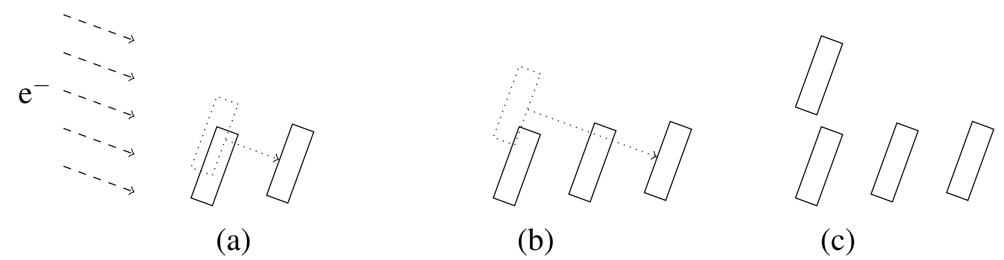

Figure 21. Staggering of the scintillator bars in multiple vertical planes. For a description of the procedure, see the text.

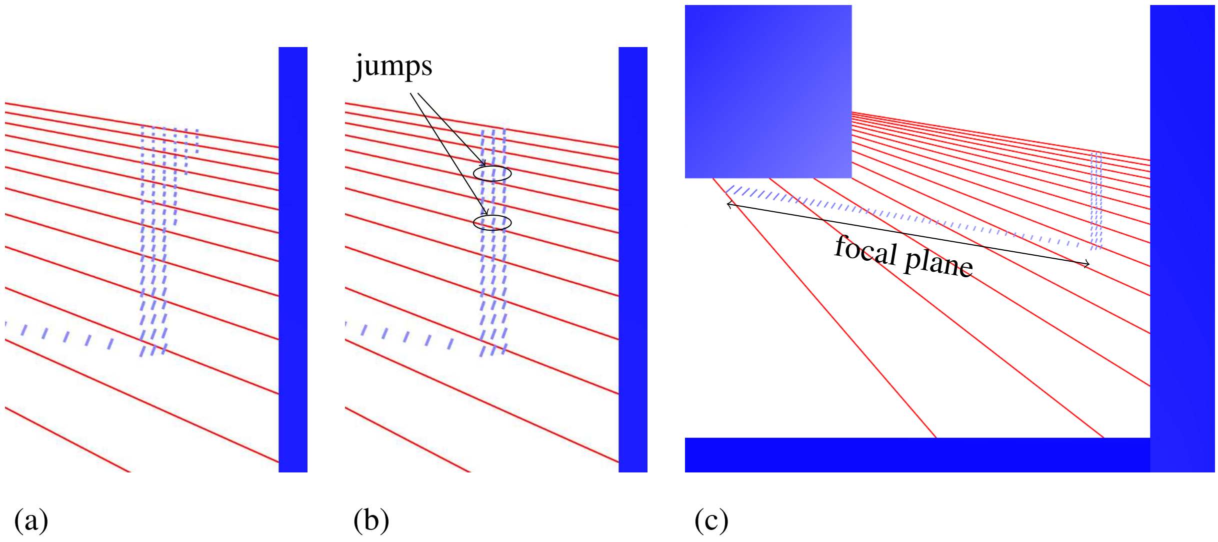

Figure 22. Calculated detector layout with constant (a) and variable (b, c) resolution. The bent red tracks are electrons with energies between $9\,\%E_0$ (300 MeV) and $97\,\%E_0$ (3100 MeV) with steps of $6\,\%E_0$ (200 MeV).

creased at $60.6\,\%E_0$ (1940 MeV) to $\Delta E \simeq 0.9\,\%E_0$ (30 MeV) and at $74.4\,\%E_0$ (2380 MeV) to $\Delta E \simeq 1.6\,\%E_0$ (50 MeV). Figure 23 shows the changeover from $\Delta E \simeq 0.6\,\%E_0$ (20 MeV) to $\Delta E \simeq 0.9\,\%E_0$ (30 MeV).

4.6 Simulation of the Energy Resolution

To investigate the influence of the beam flaw on the energy resolution, the virtual detector is exposed to simulated electrons. For this, sensitive planes with the calculated shapes of the scintillator bars, as shown in the last section, are used for the simulated detector. Now, single electrons with a random energy following the Bremsstrahlung cross section are shot into the tagging system. The information about the struck s-channels and the energy of the incoming electron is stored for 10^6 events. The gathered data set is then used for the next two steps:

Energy Calibration

By analysing the struck s-channels of each event, the corresponding c-channel is reconstructed, using the method described in Section 4.5.2. Since the energy of the incoming electron is known, an energy distribution for each c-channel can be created by doing this for all events. In the ideal case, i.e. when there is no beam flaw, this distribution has a rectangular shape (in fact, it can be slightly curved, since the Bremsstrahlung cross section increases for higher electron energies). The mean energy of each of these distributions is then associated to the corresponding c-channel. This way, the c-channels of the complete (simulated) detector are energy calibrated.

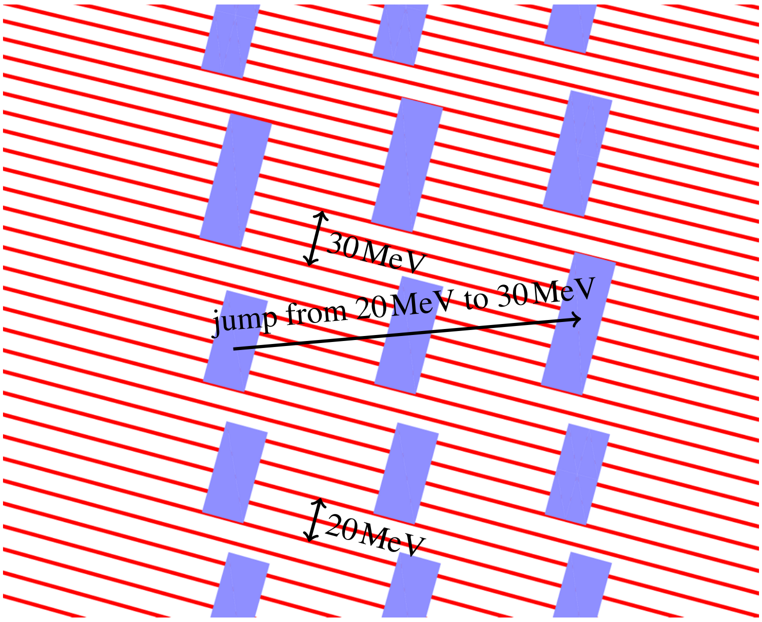

Figure 23. Resolution changeover from $\Delta E \simeq 0.6\,\%E_0$ $(20\,\mathrm{MeV})$ to $\Delta E \simeq 0.9\,\%E_0$ $(30\,\mathrm{MeV})$ in the vertical plane detector. The distance between the electrons is $0.3\,\%E_0$ $(10\,\mathrm{MeV})$.

Resolution Measurement

In the second step, realistic events, which can consist of more than one electron, are simulated. Many electrons can hit the hodoscope in such a short time that they cannot be resolved temporally. In this simulation, they are simply counted as simultaneous. The actual number of electrons per event is given by a Poissonian distribution (see Section 4.5.2). The struck s-channels of the different single electron events are then put together to form a multi electron event. If one s-channel is hit more than once, this piece of information is lost. It just looks like the channel was hit only once. Starting from this pattern of s-channels, the corresponding c-channels are reconstructed. In some cases, this can lead to a misidentification or a loss of an electron (see Section 4.5.2). Again, for each c-channel an energy distribution of the real energies is created. Due to the multi electron events, this distribution will differ from the distribution which was created for the calibration. The energy resolution σ_E is defined as the standard deviation of this new distribution,

$$\sigma_E = \sqrt{\frac{1}{n-1}\sum_{i=1}^{n}(E_i - \bar{E})^2}, \tag{34}$$

where E_i are the real energies corresponding to the specific c-channel, $\bar{E}$ is the mean of all E_i. In case of the ideal rectangular distribution,

$$\sigma_E = \frac{\Delta E}{\sqrt{12}} \tag{35}$$

defines the smallest value which is possible for σ_E. The distributions and the resulting resolutions are simulated without a radiator and with the Cu $200\,\mu\mathrm{m}$ radiator, see Figure 24. In the left pictures, the distribution of the differences between the detected and the real energies is shown for each c-channel. Using the differences instead of the real energies makes the diagram clearer but does not change the standard deviation σ_E, which is shown in the right pictures. The values of $\sigma_E(E_{\mathrm{real}})$ can be interpreted as the resolution the energy E_{real} is measured with. The vertical lines in Figure 24 denote the position the hodoscope goes into the vertical plane. The horizontal lines denote the theoretical minimum resolution $\sigma_E = \Delta E/\sqrt{12}$. This shows the strong influence of the placement out of the focal plane, as the resolution clearly differs from the minimum value starting with the vertical plane. The worst resolution without including the radiator is $\sigma_E = 0.56\,\%E_0$ (18 MeV), using a 200 µm Cu radiator, the resolution becomes $\sigma_E = 0.63\,\%E_0$ (20 MeV). This resolution is obtained for the highest electron energies, where $\Delta E = 1.56\,\%E_0$ (50 MeV). The deviation from the theoretical minimum of $\sigma_{50\,\mathrm{MeV}} = 0.45\,\%E_0$ (14 MeV) thus is $\sigma_{\mathrm{min}} = 0.19\,\%E_0$ (6 MeV). This number constitutes the best resolution which could be achieved with arbitrarily small scintillator bars. The best resolution for both scenarios is $\sigma_E \simeq 0.19\,\%E_0$ (6 MeV) for the lowest electron energies.

In this chapter, the arrangement for all scintillator bars in the focal plane as well as in the vertical plane was computed. Starting from the measured magnetic field map, the electron trajectories were simulated and the focal plane was calculated. Using this information, the scintillator bars could be placed. Finally, the resolution which is expected for this design was calculated. For all simulations, the 3200 MeV field map was used without the scaling for the smaller current in the BGO-OD tagging magnet. Since all steps in this chapter can be repeated fully automated using the created ROOT programs, the calculations for the final design of the tagging system can be redone using the reduced magnetic field. Also the mechanical design, which is made in the next section, can be adapted easily to the final layout without a large effort.

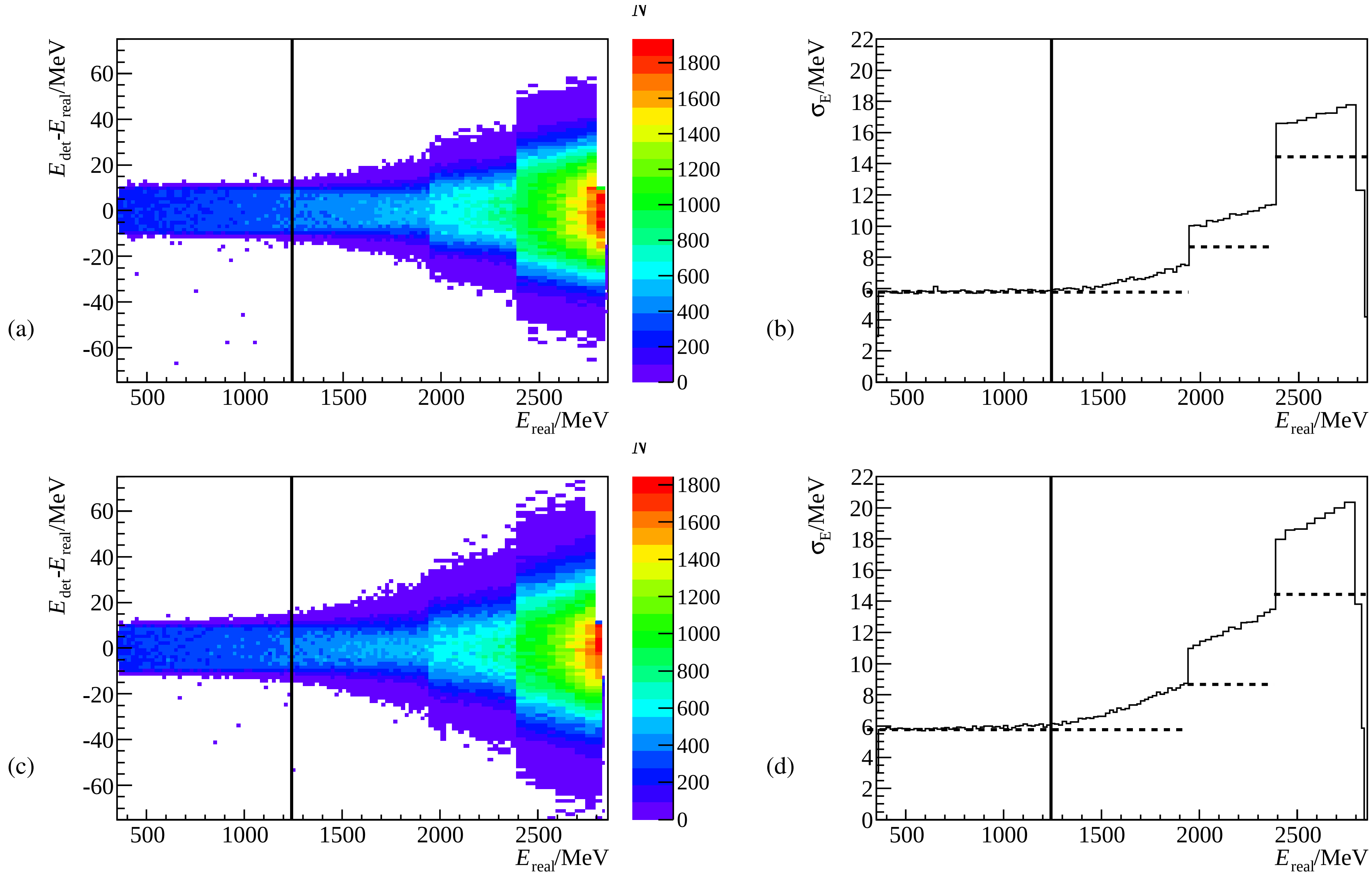

Figure 24. Simulated energy distribution and resolution without radiator (a and b) and with Cu 200 μm radiator (c and d). The vertical lines denote the start of the vertical plane. The horizontal lines denote the theoretical minimum resolution due to the energy width. For details, see the text.

5 Final Design and Prototype Detector

Using the arrangement of the scintillator bars described in the last chapter as a starting point, the design of the mechanical construction for the vertical plane detector is presented in the following sections. Since the design has to be tested, the prototype is created only for nine channels. The energy range of this prototype lies at the second step in the energy width (see Figure 22 (b)). This range is chosen to test the capability of high electron rates and to observe the influence of the step in the energy width. For this part of the tagging system, the Hamamatsu PMTs are chosen, since these have very small dimensions paired with a high rate capability, as described in Section 3.6.

One desirable feature of the tagging system is easy maintenance (see Section 3.4). It should be possible to replace single photomultiplier tubes without dismounting the complete detector and possibly affecting the alignment of the scintillator bars and thereby its energy calibration. This is achieved by putting everything except for the PMTs into one big chassis. In addition, the scintillator bars are mounted in a way which makes it possible to remove small groups of them easily. The complete construction can be roughly split into three different parts: The overall chassis, the PMT assemblies and the slides holding the scintillator bars. To have more space available for each PMT assembly, they are put alternately on the left or the right side of the Bremsstrahlung plane. In the following, the single components will be described. The design is made using Autodesk Inventor 2009[24], all shown pictures are extracted from this software. Technical drawings for all parts can be found in Appendix A.

5.1 PMT Assemblies

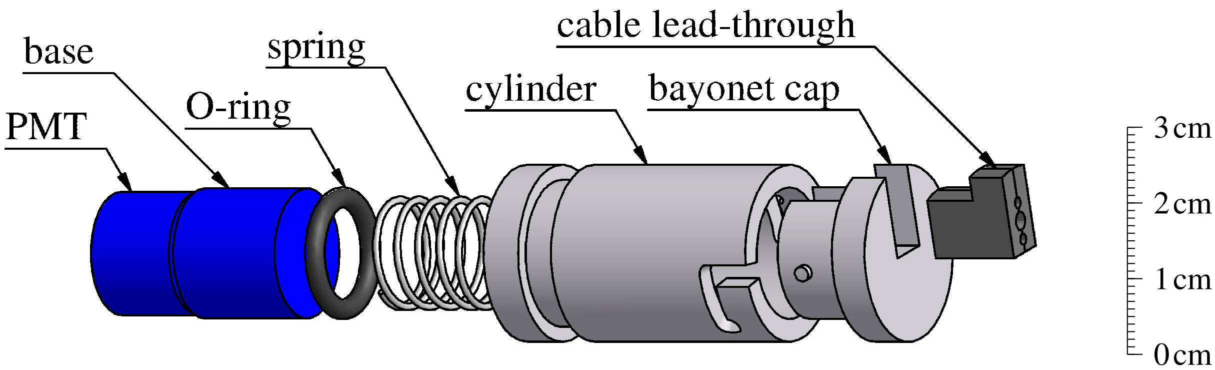

Figure 25. Exploded view of the PMT assembly (to scale).

The PMT assemblies consist of one metal cylinder into which the PMT together with its socket assembly fits exactly and is closed with a bayonet cap (Figure 25). The signal and high voltage cables are guided through a pair of plastic pieces made of black POM[25] which fit into a notch on the bayonet cap. This way the light incidence is minimised and a safe mount for the cables is provided. Between the cap and the socket assembly a metal spring is placed to assure

[24] a 3D mechanical solid modeling design software for creating 3D digital prototypes
[25] POM: Polyoxymethylene

a constant pressure of the phototube onto the scintillator bar. This pressure is needed because the scintillator bars are not glued to the PMTs, instead a piece of transparent silicone is used for the coupling (see Section 5.4). The springs used here apply a force of $F \simeq 15\,\mathrm{N}$, which is more than actually needed. This value was chosen because no other suitable normative springs with the correct dimensions were available. To make sure that no light goes beyond the PMT base, an NBR[26] O-ring with a slightly higher diameter than the inside of the metal cylinder is placed between the spring and the base.

5.2 Slides

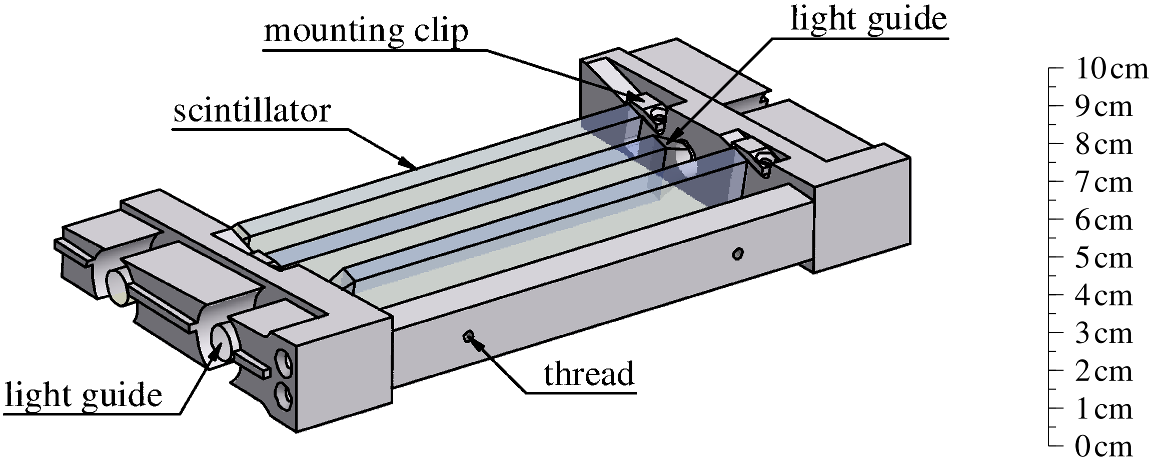

Figure 26. View of the back side of a slide (isometric, scale 1:2).

Three consecutive scintillator bars are each placed onto a single slide (Figure 26) which can be moved individually into the chassis. Thereby, all scintillator bars are accessible easily. If they were mounted directly into the chassis, only the first plane would be accessible directly. That means, to remove a scintillator bar in the middle or back plane, several other scintillator bars would have to be removed individually. The usage of the slides implies that scintillator bars from one slide must not touch scintillator bars from another slide during movement. To accomplish this, the slides must be assembled in a certain angle relative to the chassis (see Figure 27). For each slide, a maximum and minimum angle fulfilling this prerequisite is calculated. As it turns out, one single angle is not enough for all slides, but each time the resolution decreases, i.e. the scintillators strongly increase in size, the angle has to be changed. This way, three different angles are needed for the vertical plane detector. The slides at which the resolution changes are different to the other slides, as they have different angles for the top and the bottom side and thus have the outline of a wedge. Unfortunately, the thicker part of this wedge lies at the back of the detector chassis, implying that it cannot be pulled out without first removing one other slide. This seems to be acceptable because the scintillator bars will be replaced much less often than the PMTs.

[26]NBR: Nitrile butadiene rubber

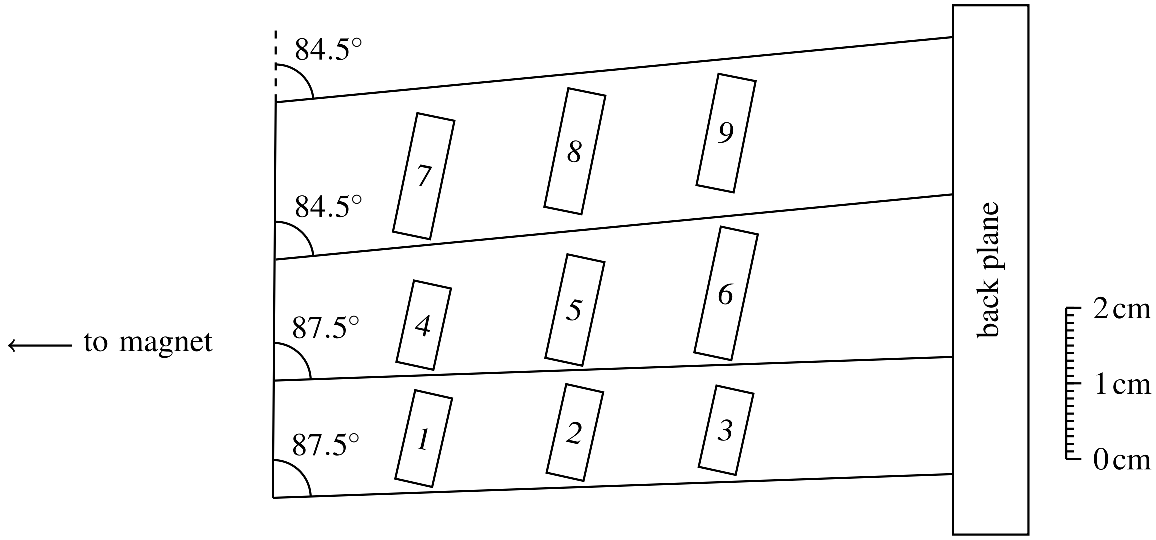

Figure 27. Profile of the slides for the prototype detector (to scale). The numbered rectangles represent the scintillator bars.

The slides are made of three parts (Figure 26). Two opposing parts hold the scintillators. They are screwed to the third part which is located on the back of the system. The back part contains two threads allowing the slide to be fixed in the chassis once it is moved into its final position. The alternating placement of the phototubes is reflected in the design of the slides. On one side, a single mount for a scintillator and two lead-throughs for the light guides are built. The light guides are glued onto the scintillator bars. On the opposing side, there are two mounts and one lead-through. The mount for one scintillator bar consists of one notch in the inner side of the slide and a clip which is mounted on top of the scintillator to fix it. The bottom of the notch has to be manufactured with a high precision, as its position defines the energy of the corresponding c-channel. Using the same precision, the rails on the side of the slide are made. For the prototype, a production tolerance of $\Delta d = 0.1\,\mathrm{mm}$–$0.2\,\mathrm{mm}$ is used. In the energy range of the prototype, the energy width of $\Delta E = 20\,\mathrm{MeV}$ corresponds to width of the scintillator bars of about $d = 5\,\mathrm{mm}$. Therefore, when a slide is removed and mounted again, it can be realigned with an energy tolerance of $\Delta E \cdot \Delta d/d = 0.8\,\mathrm{MeV}$.

As described in Chapter 2.5.2, the magnetic shielding of a phototube should exceed the photocathode by at least the radius of the shielding. This way the shielding does not only cover the PMT but also a part of the light guide which therefore has to be elongated. To keep the light guide still confined in the slide, the side parts have to be made thick enough to provide for sufficient space.

5.3 Chassis

The chassis consists of three 2 cm thick aluminium plates which are held together by screws (Figure 28). The front, top and bottom side are left free and will be covered by a black plastic foil. On the inside, the chassis has grooves which take the slides with the scintillator bars. On the outside, there are slots into which the PMT assemblies fit. These have a depth of 5 mm and their inner diameter is made fit to the PMT assemblies. Directly outside of the chassis, the metal cylinder of the PMT assembly has a smaller outer diameter (see Figure 25). Screwed mounting

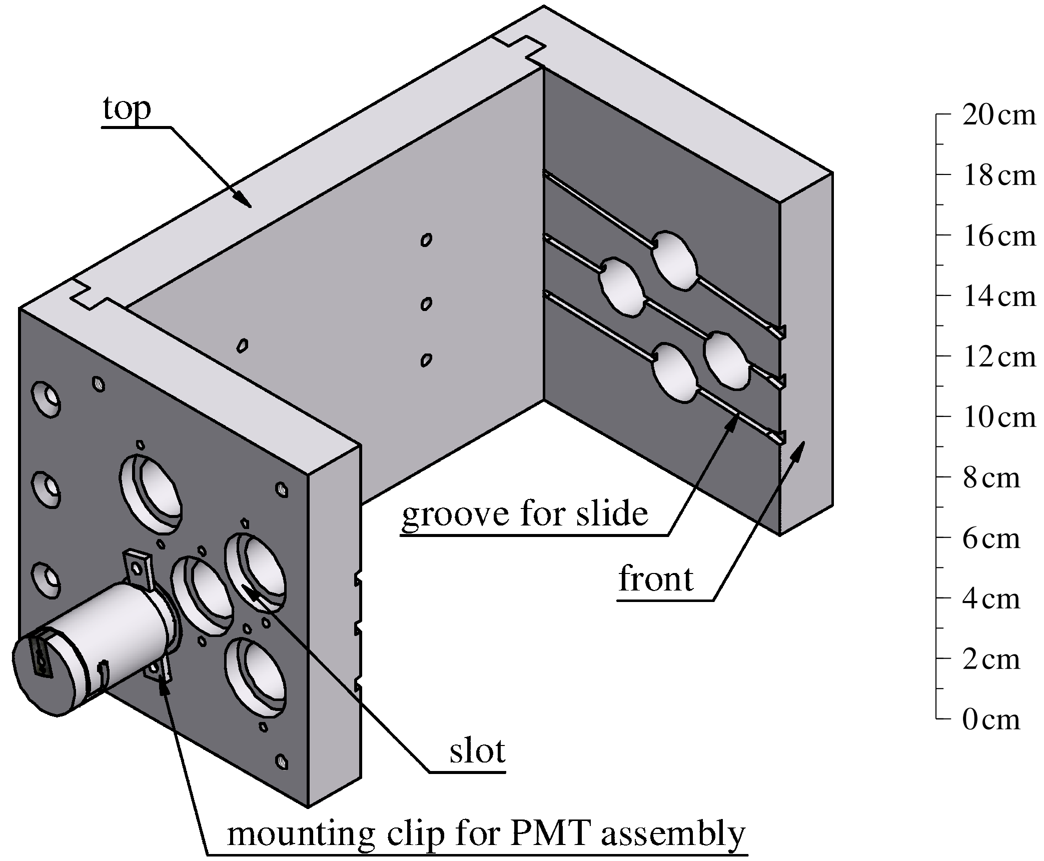

Figure 28. Chassis with one mounted PMT assembly (isometric, scale 1:2.5). The electron beam comes from the front.

clips, which fit into this recess, are used to attach the assembly to the chassis. By mounting the assemblies firmly into the slots, no light comes from the outside into the chassis. The slots have holes with the same diameter as the holes in the PMT assemblies and the slides. Once the slides and the PMT assemblies are mounted, the PMT is shifted through all three consecutive holes until it touches the light guide.

5.4 The Complete Prototype Detector

All parts of the prototype detector were manufactured in the mechanical workshop of the HISKP[27] in Bonn. Since the final scintillator material was not available at the time of production, a spare piece of unknown, and unneeded scintillator material had to be used. To match the cross section of the scintillator bars to the cross section of the PMT, light guides as shown in Figure 29 are used. The assembling procedure consists of different steps, shown in Figure 30 (1)–(7):

(1) The light guides are glued on the scintillator bars.

[27] Helmholtz-Institut für Strahlen- und Kernphysik

(2) The scintillator bars are mounted onto the slides (a and b).

(3) The metal tubes of the PMT assemblies are mounted onto the chassis. The slides are moved into the chassis, considering the right order due the single wedge-shaped slide, and fixed by the screws on the back.

(4) To prevent crosstalk of light between different channels and to improve the light collection in the scintillator, reflective plastic foil is wrapped around each scintillator bar.

(5) The complete device is covered with black plastic foil.

(6) The remaining parts of the PMT assemblies are put into the cylinders and locked by turning the bayonet cap (a). The coupling between the light guide and the PMT is achieved through a "cookie", a roughly 2 mm thick, round piece of transparent silicone (b).

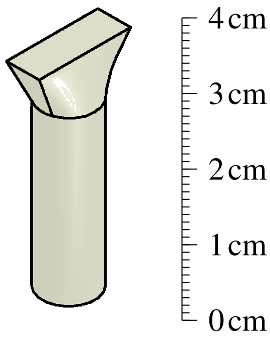

Figure 29. Light guide (isometric, to scale). The size is adapted to the width of the scintillator bar.

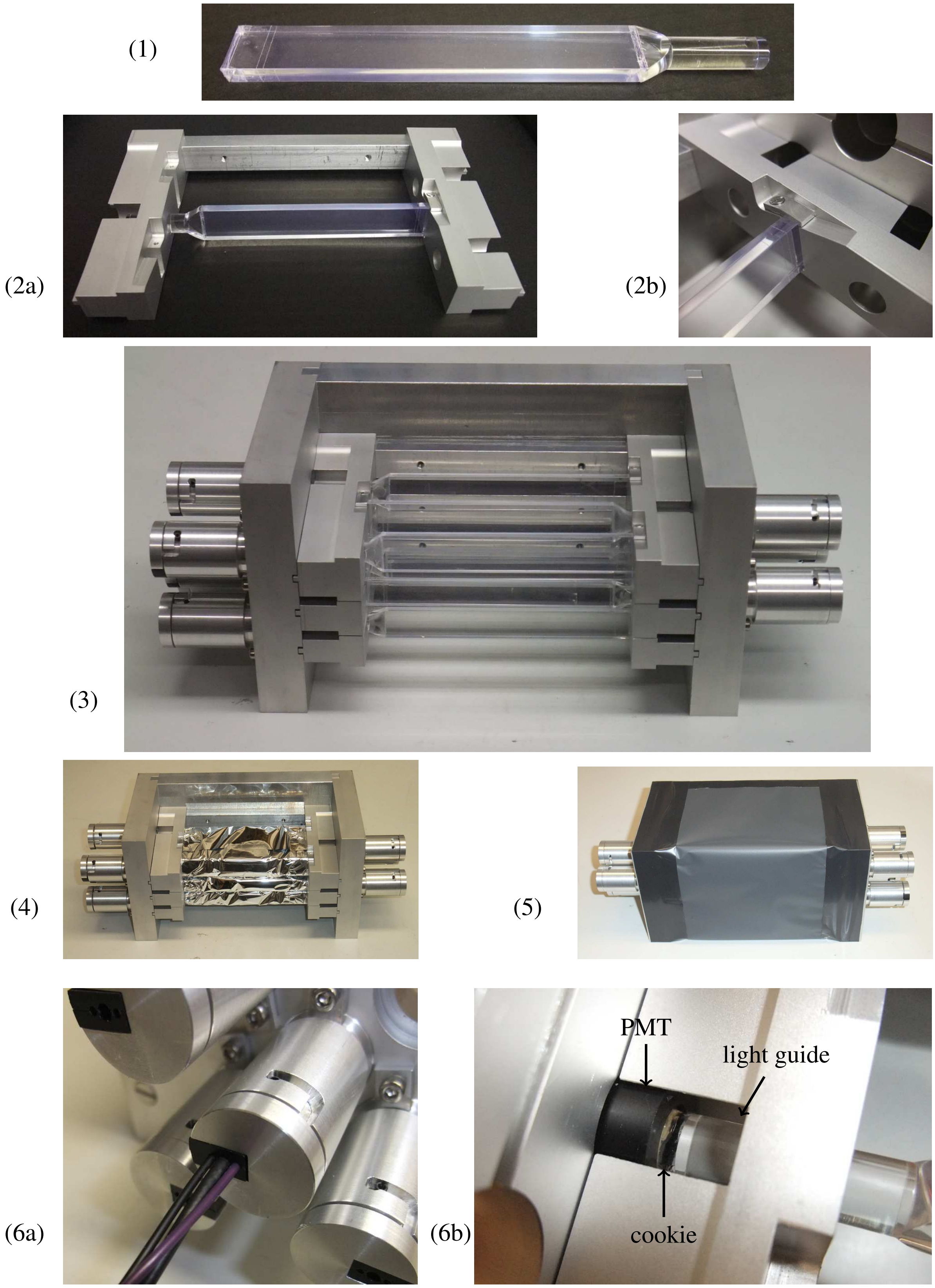

Figure 30. Assembly of the prototype detector. For description, see the text.

6 Experimental Tests

In this chapter, the experimental setup used for the prototype tests and the collected data will be presented. The first test was performed in parallel to the Crystal Barrel (CB) experiment in July 2010, with the detector located behind the CB tagging system. This provided a first check for the prototype and the read out. The second test was dedicated to the prototype and took place in the BGO-OD area, close to the final position of the new tagging system.

Before describing the individual tests in detail, the electronics and the data acquisition common to both tests are introduced.

6.1 Electronics Setup and Data Acquisition

The complete data collection can be split into a hardware and a software part: On the one hand, the electronics which transforms the analogue output of the photomultiplier tubes into digital signals incorporating information about signal height and timing. On the other hand, the data acquisition (DAQ) [Ham10], a software which controls the electronic components, reads out and stores all gathered data.

6.1.1 Components

Figure 31 shows a block diagram of the complete electronics setup. For a better understanding of the complete system, the components are presented individually in this section. The next section explains the assembly of all these components.

Electronic Standards

All electronic components are packed into modules which follow widely used standards in nuclear and high energy physics. These are NIM[28], CAMAC[29] and VMEbus[30]. Common to all of them is that they provide a standardised mechanical and electrical interface. Multiple modules of one type can be put into a crate which also provides the power supply. In contrast to NIM, the CAMAC and VMEbus systems feature a backplane allowing for communication between different modules in one crate, VMEbus offering the higher data transmission rate (up to $320\,\mathrm{MB\,s^{-1}}$ compared to about $8\,\mathrm{MB\,s^{-1}}$ for CAMAC). In addition there are special modules which can connect a CAMAC crate to a VMEbus crate[31], allowing for communication between them.

[28]Nuclear Instrument Module

[29]Computer Automated Measurement And Control

[30]Versa Module Eurocard bus

[31]in the CAMAC Crate: a Joerger Crate Controller Type A-2 Model CCA-2, in the VME crate: a CES CBD8210 Branch Highway [CRE96]

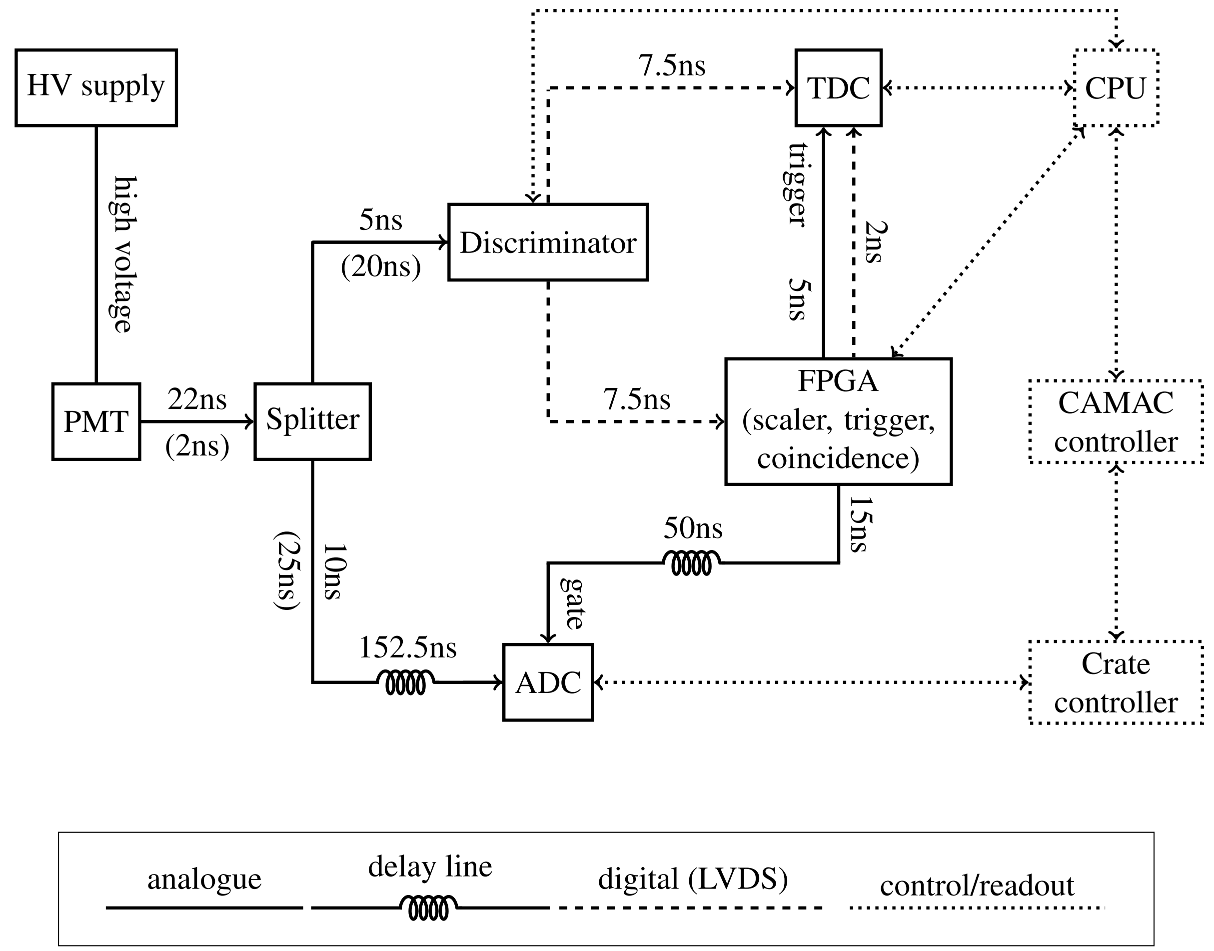

Figure 31. Block diagram of the electronics. The values in brackets are used in the second test.

Trigger Logic

The goal of the measurements with the BGO-OD experiment is the investigation of hadronic states. Compared to the electromagnetic background, the cross section for the production of an interesting hadronic state is very small. To assure that enough of these states are produced, the experiment will be run with very high photon rates of up to 50 MHz, which also implies a total rate of events which is too large to store each event. For this reason it has to be decided which events should be stored and which should be rejected. This is the purpose of the trigger logic. Only when a defined set of conditions is fulfilled, a trigger signal is released, leading to a readout. These conditions are chosen to select hadronic events via their decay signature. One condition will be coincident hits of neighbouring channels[32] in the tagging system. Other conditions can, e.g., be a minimum energy deposit and a defined number of clusters in the BGO ball, or a number of tracks in the forward spectrometer. The coincidence in the tagging system is chosen because only events with a known photon energy can be analysed. If the scattered Bremsstrahlung electron is not detected or the reaction was not caused by a Bremsstrahlung photon at all, this parameter is unknown. Using several trigger conditions, the events to be stored are partly preselected and the resulting readout rate is strongly reduced. After a trigger

[32] in this chapter, s-channels are simply referred to as channels, i.e. the combination of one scintillator bar and one PMT

is released, the trigger logic pauses until the data readout is finished and the electronics is ready again.

For these tests of the tagging system, each single hit in one channel releases a trigger signal. This minimum bias condition, also called *tagger-OR* (a logical or of all tagging channels), is chosen to provide more options for the data analysis as will be shown in Section 7. The trigger logic is implemented on an FPGA board (see below).

Discriminator

The purpose of a *discriminator* is to detect event signals and to distinguish them from electronic noise. In the simplest case, this is achieved by only accepting signals which reach an adjustable threshold. When the discriminator detects such a signal, it generates a logical pulse. Nothing happens, if the signal is below the threshold. To assure that this method works properly, the signal has to be clearly larger than the noise, typically a few mV. Then, the threshold can be set between the noise and the signal level.

When a discriminator detects a suitable signal, a second signal coming shortly after will be ignored. The shortest time without rejecting the second one, is called *dead time*. If the dead time is too short, one long pulse could activate the discriminator multiple times. In case it is too long, the maximum count rate will be significantly reduced.

The discriminator used here features 32 channels, NIM inputs and LVDS[33] outputs. The dead time is 30 ns.

Analogue to Digital Converter

An *Analogue to Digital Converter (ADC)* converts an analogue signal into a digital signal. In this case an LRS 2249A 12 channel ADC with a relative resolution of 0.1 % is used [LeC74]. It integrates the current in an input channel over a fixed time, which is defined by a digital pulse on the *gate* input. Because this is the same as the total charge going into this input channel, this kind of ADC is also referred to as QDC[34]. After each measurement, the ADC outputs a channel number x for each input channel which is related to the charge Q as follows:

$$x = Q \cdot c + x_{\text{pedestal}}, \tag{36}$$

where c is a conversion factor and x_{pedestal} an input channel dependant offset.

Figure 32 shows a simulated[35] ADC spectrum for an ideal detector with two independent channels. Either channel can release a trigger, leading to a measurement of both detector channels. The detector which released the trigger will then induce a charge on the ADC input, while the other detector will induce no charge. Looking at a fixed detector channel, this leads to a narrow *pedestal* peak at $x_{\text{pedestal}} = 100$ and a Landau[36] distributed pulse height spectrum well

[33]Low Voltage Differential Signal
[34]Charge to Digital Converter
[35]simulated by a short ROOT-script
[36]this distribution describes the energy deposit of ionizing particles in thin material, see [Leo94]

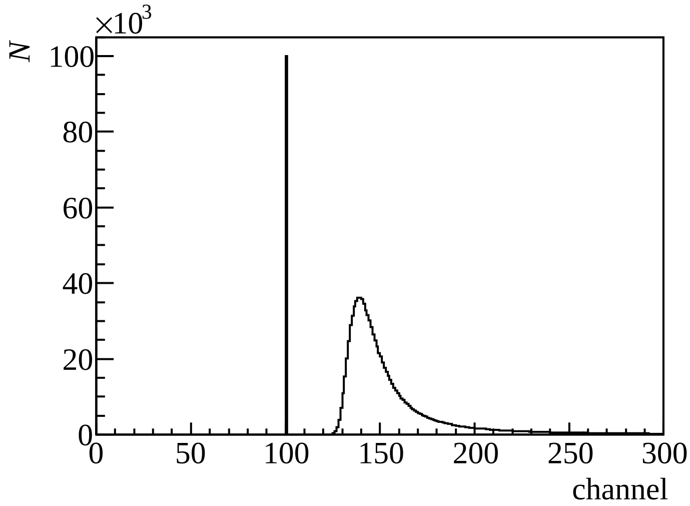

Figure 32. Simulated ADC spectrum of an ideal detector with two independent channels.

separated from this pedestal. In reality, both structures will be broadened due to different effects including a finite charge resolution of the ADC.

Pulse Splitter

Since the analogue output signal of the phototubes will be used as an input for the ADC as well as the discriminator, the signal has to split somehow. This can be achieved by using a passive pulse splitter as shown in Figure 33. One downside of this simple circuit is that it halves the size of the signal. In addition, resistors which have a slightly wrong size can lead to reflections and the outputs can influence each other, as will be shown in Section 6.2.3. The situation can be improved by using an active pulse splitter, which amplifies the signals and prevents cross-talk. This is planned for the final setup of the tagging system [Mes10].

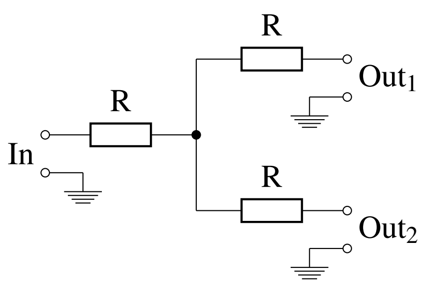

Figure 33. Passive pulse splitter. $R = Z/3$, Z being the cable impedance [Leo94].

Time to Digital Converter

To obtain the timing information of hits in the detector, a multi hit *Time to Digital Converter (TDC)* is used. The employed CAEN V1190A TDC [CAE06] provides for two different operation modes, the *trigger matching mode* and the *continuous storage mode*, the former being the one employed and described here. In this mode, the TDC stores the time of the leading

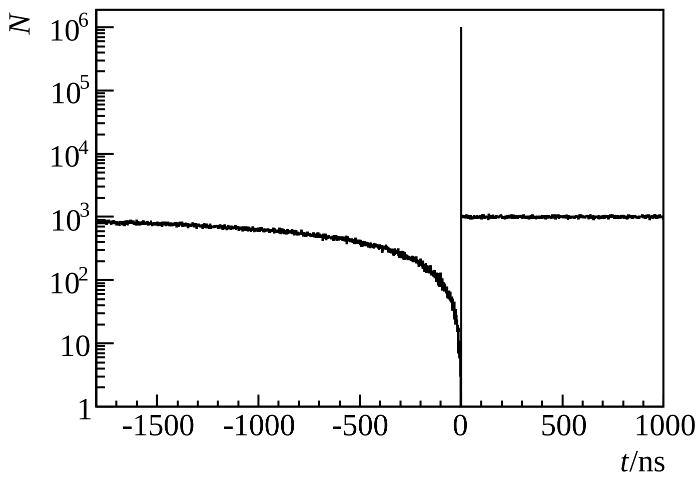

Figure 34. Simulated TDC spectrum of an ideal detector with one channel and a mean rate of 1 MHz. The x-axis shows the time of a hit relative to the trigger time with a bin width of $\Delta t_{\mathrm{bin}} = 1$ ns. The y-axis is logarithmic.

edge[37] of digital signals on the input channels relative to the trigger signal. The trigger signal has a dedicated input port on the TDC. Until a trigger occurs, the TDC continuously measures the times of all[38] input signals. It then continues measuring for a defined time and stores all measured timing information between a fixed time before the trigger and a fixed time after the trigger. In the continuous storage mode, the TDC continuously stores the times of the input signals into an output buffer until it is reset. This can lead to an overflow of the output buffer, when the TDC cannot be read out sufficiently fast.

The CAEN V1190A is based on the CERN/EPC-MIC HPTDC chip [Chr04]. It provides 128 channels and a timing resolution of 100 ns. The range of the time window can be programmed and is set to 1800 ns before and 1000 ns after the trigger. The trigger matching is based on an internal clock of 40 MHz, which means that the measured times can be displaced up to $25\,\mathrm{ns} = 1/40\,\mathrm{MHz}$ relative to the trigger. For this reason, the trigger signal is not only used to trigger the TDC, but is additionally put on one of the input channels. By subtracting the time which is measured in this way from each measured time, one gets all the times relative to the trigger with the highest possible resolution.

Figure 34 shows a simulated[39] TDC spectrum for an ideal detector with a single channel and a mean rate of $n = 1$ MHz. The temporal distance between two hits follows an exponential distribution, imitating the real behaviour of independent electrons entering the detector. $N_{\mathrm{events}} = 10^6$ individual events were simulated and stored in the shown histogram. Clearly, the number of hits for $t = 0 = t_{\mathrm{trigger}}$ is equal to $N_{\mathrm{events}} = 10^6$. This peak can be broadened for a detector with multiple channels and is called *prompt peak*. After the trigger signal arrives, hits continuously occur with the same rate, leading to a mean entry of $N_{\mathrm{events}} \cdot n \cdot \Delta t_{\mathrm{bin}} = 10^3$. The hit distribution prior to the prompt peak is a bit more complicated, but can be derived as follows: At one random point in time t_0 the electronics becomes ready and the trigger is reset. The first

[37] In principle, also the trailing edge or both can be measured.

[38] in contrast to a single hit TDC, which can only do one measurement per channel until it is reset

[39] the TDC is simulated by a short ROOT-script, mimicking the trigger matching mode

hit occurring after this point will then release the trigger. The time distance between this hit at t_{trigger} and t_0 follows again an exponential distribution:

$$P(t_{\text{trigger}} - t_0)\mathrm{d}t = n\mathrm{e}^{-n(t_{\text{trigger}}-t_0)}. \tag{37}$$

The probability for a hit occurring between $t_<$ and $t_< + \mathrm{d}t < t_0$ is

$$P(t_<)\mathrm{d}t = n\mathrm{d}t. \tag{38}$$

To observe a hit with a distance Δt before the prompt peak (on the left side), $t_{\text{trigger}} - t_0$ has to be smaller than Δt. This leads to

$$P(\Delta t)\mathrm{d}t = P(t_{\text{trigger}} - t_0 < \Delta t) \cdot P(t_<)\mathrm{d}t = n \int_0^{\Delta t} \mathrm{d}t' \mathrm{e}^{-nt'} n\mathrm{d}t = n(1 - \mathrm{e}^{-n\Delta t})\mathrm{d}t, \tag{39}$$

perfectly matching the shown spectrum. If two signals follow in a short time, it is more likely that the first one releases the trigger than the second one. This way the count rate for small distances prior to the trigger is suppressed. For large distances, the count rate asymptotically reaches the same rate as after the prompt peak.

Scaler

A *scaler* counts the number of signals between two trigger incidents, even during the time when the remaining electronics is being read out. This way, the scaler "sees" all hits and not only those during a small window around the trigger time like the TDC does. Each detector channel has its own scaler. An additional scaler is connected to a fixed clock of 1 MHz. By dividing the number of entries of one scaler by the number of entries in this 1 MHz scaler, one directly gets the mean rate in MHz since the last trigger. As well as the trigger logic, the scalers are implemented on an FPGA board (see below).

Coincidence Matching

The trigger will only be released when two neighbouring channels were hit. The aim of using adjacent channels is to reduce the background (see Section 3.5). The logic which computes these spatial and temporal coincidences is also implemented on an FPGA board, but still has to be tested (see Section 7.3).

FPGA

Roughly speaking, an *FPGA*[40] is an integrated circuit which consists of many logical gates and different in- and outputs which are by default not connected to each other. The connections between the gates themselves and between the gates and the in- and outputs can be (re)programmed externally, enabling the user to build complex logical circuits without having to construct special hardware and to change the function of this module as one needs.

For this test, one XILINX Spartan-3 XC3S1500 module houses the trigger logic, the coincidence matching and the scalers. It was programmed by D. Hamman [Ham10]. The in- and outputs are implemented on separate *mezzanine* modules, of which up to three can be attached to the FPGA board.

[40] Field Programmable Gate Array

VME computer

Aside from the VMEbus form factor, the VME computer[41] (or VME CPU) is an ordinary computer running a customized GNU/Linux operating system. Amongst others, it possesses two Ethernet ($100\,\mathrm{MB\,s^{-1}}$ and $1\,\mathrm{GB\,s^{-1}}$) controllers, USB ports and a VME interface. It performs different tasks: Most important, it runs the DAQ software, controlling and reading out the TDCs, the ADCs and the scalers (see Section 6.1.3). Furthermore, it reprograms the FPGA and sets the thresholds of the discriminator via its serial interface. Using the *slow control* [Han10], a system which allows for the setting and monitoring of many different parameters related to the complete experiment (e.g. temperatures, voltages), it is possible to set the thresholds remotely without accessing the experimental area directly.

HV supply

The High Voltage (HV) supply used for the photomultiplier tubes is a LeCroy System 1440, which can be loaded with up to 16 modules. The PMTs are connected to a 1443N module, providing 16 outputs of up to $2500\,\mathrm{V}$ negative high voltage. The HV system is connected to the slow control and can be programmed remotely.

6.1.2 Assembly of the Electronics

The block diagram and a photograph of all electronic components which were used for the test of the prototype detector are shown in figures 31 and 35, respectively. Apart from different cable lengths and the mechanical construction, it is the same for the test at the CB experiment and the test at the BGO-OD experiment.

In the beginning (see left part of Figure 31), the signal of the phototubes is split and then used for analogue and digital processing, as described in the next two paragraphs.

Digital Signal Chain

One output of the splitter is carried to the discriminator to generate digital pulses for suitable signal heights. The discriminator itself has two outputs (per channel), one being directly connected to the TDC, the other to the FPGA. The FPGA generates the coincidence signals and the trigger for the TDC as well as the gate signal for the ADC. In addition, the input signal is redirected to the scaler implemented on the same board.

Analogue Signal Chain

The other output of the splitter is carried to the ADC. The signal has to be delayed, since the ADC has to receive the beginning of the gate from the FPGA, before the analogue signal arrives. The delay of $\Delta t \simeq 150\,\mathrm{ns}$ was chosen for practical reasons. The cable for the gate signal was prolonged accordingly to match the right timing. The correct timing was checked using a oscilloscope with a pulsed signal as input as shown in Figure 36. The pulse clearly arrives at

[41] a GE VME 7807RC

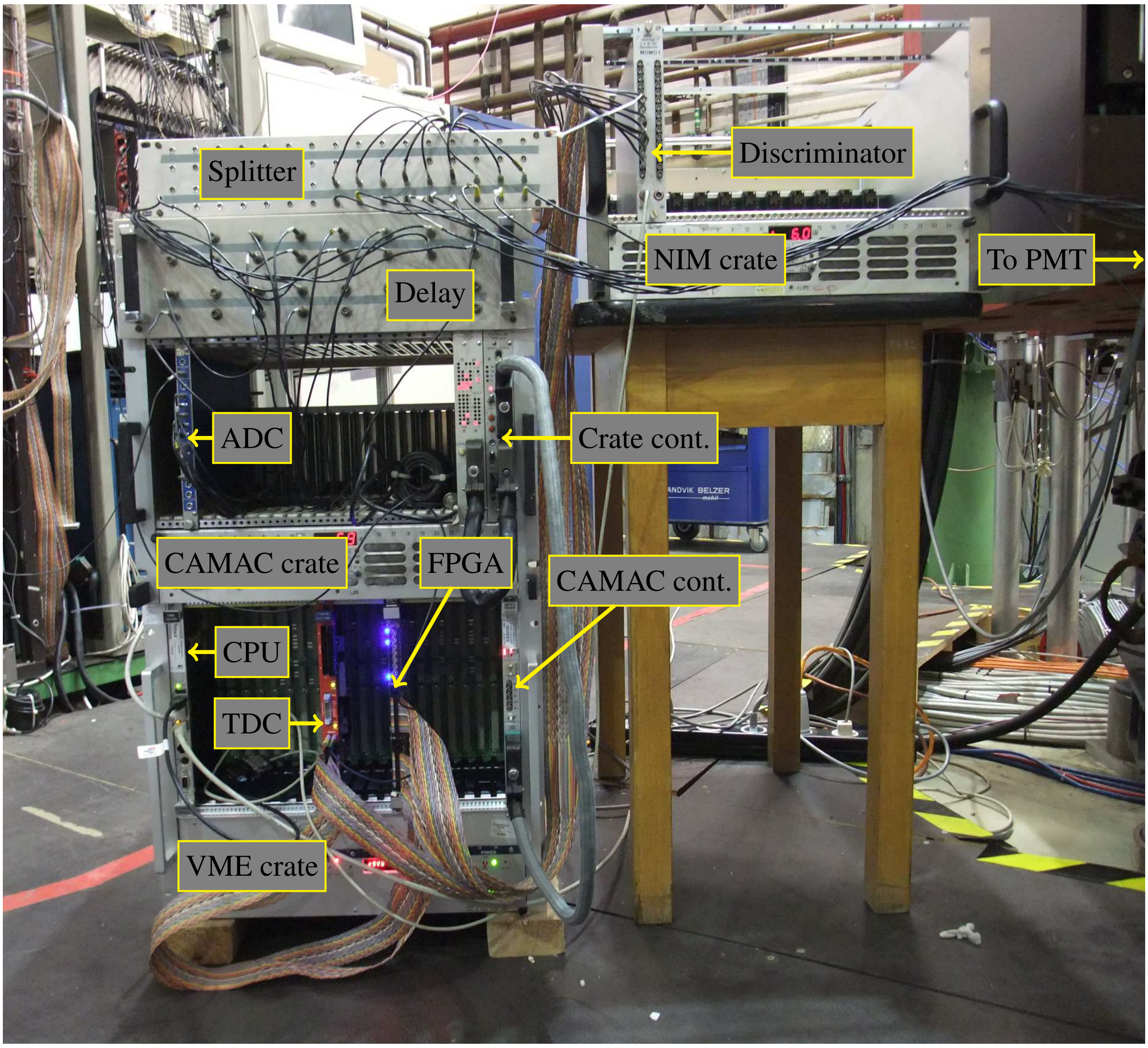

Figure 35. View of the electronics setup used for the first test. The components are the same for both tests.

the ADC (green line) while the gate (blue line) is open. The delays between the input and the ADC/discriminator are reduced by equal amounts with respect to the setup on Figure 31. The gate signal jitters within 10 ns, because it starts and ends exactly at a clock cycle of the FPGA, which runs at 100 MHz.

6.1.3 Readout and Data Acquisition

To start taking experimental data, one remotely connects to the VME computer and starts the *DAQ* (*Data AcQuisition*), which is coded by D. Hamman [Ham10]. This program first initializes the TDC and the ADC and programs the FPGA. Then it starts to record events until a predefined maximum number is reached. One event cycle consists of three phases: 1. Waiting until a trigger occurs. 2. Reading out the electronics (ADC, TDC, scalers). This takes more than 100 µs, so that events occurring within this time are only counted by the scalers. The long

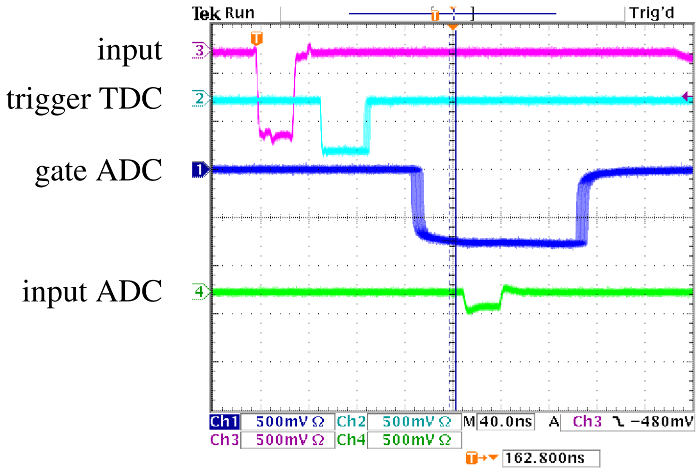

Figure 36. Timing of the different signals. The input signal (red line) activates the trigger signal (cyan line) and the gate signal (blue line). The delayed input (green line) reaches the ADC while the gate is open. The input signal is a square signal generated by a function generator.

time is needed by the ADC and the VME computer to process the input data. 3. Resetting the electronics to the initial state, ready to record the next events.

The readout of the TDC and the scalers can be done directly through the VME backplane while the ADC cannot be read out directly. To accomplish this, the CAMAC crate controller is connected to a VME-CAMAC interface sitting in the VME crate. This way, the VME computer has access to the ADC. The data are finally stored in a ROOT file on a network drive, easily accessible for the analysis.

6.2 Test at the Crystal Barrel Experiment

The first test of the prototype was done in parallel to a regular measurement of the Crystal Barrel experiment in July 2010. Because this beam time was not dedicated to the prototype, it had to be mounted behind the tagging system of CB, to avoid any influence on the ongoing experiment. After describing the experimental setup, first data, measured during this test, will be presented.

6.2.1 Assembly of the Test Stand

With respect to the BGO-OD tagging magnet, the CB tagging magnet is rotated by 90° around the beam axis. Therefore, it is a horizontal bend device. This opens the possibility to construct a frame located independently behind the CB tagging system, which is capable of holding the prototype (see Figure 37). The framework is made of aluminium profiles, partially from RK ROSE+KRIEGER. It can be used to mount the prototype or other detectors at different positions behind the CB tagging system and in this way expose them to different electron rates (for technical drawings, see Appendix A). An additional option is the positioning above or underneath the plane of Bremsstrahlung.

Figure 38 shows an overview of the complete setup. The high voltage and the power supply is taken from the BGO-OD area.

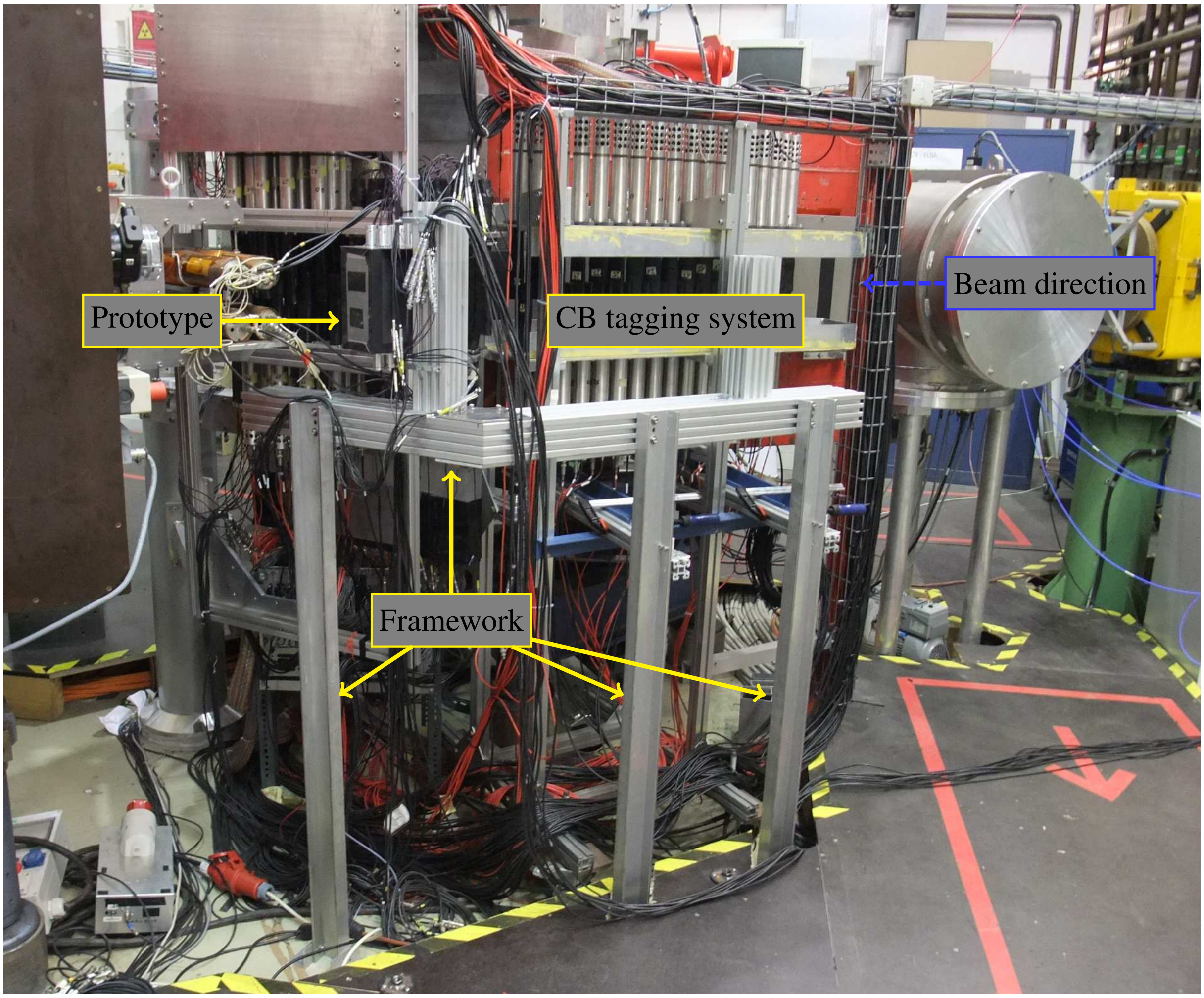

Figure 37. View of the framework in front of the CB tagging system.

6.2.2 Detector Settings

During the test, all photomultiplier tubes were operated at the same nominal voltage of 800 V and the same discriminator threshold value of 30[42]. Using this threshold, the complete signal peak could be observed in the ADC spectra.

The detector was mounted at two different positions, one of them corresponding to the highest possible rate which could be reached within the spatial restrictions. Since these positions were different from the position the prototype detector was designed for, one problem arose: If the detector is mounted in its designed position and its back plane is parallel to the side of the magnet where the primary beam exits, the electrons hit the scintillator bars perpendicular to their surface. When arranged at another position, the detector has to be rotated to accomplish

[42]This number is dimensionless. The corresponding threshold voltage rises linearly with this value

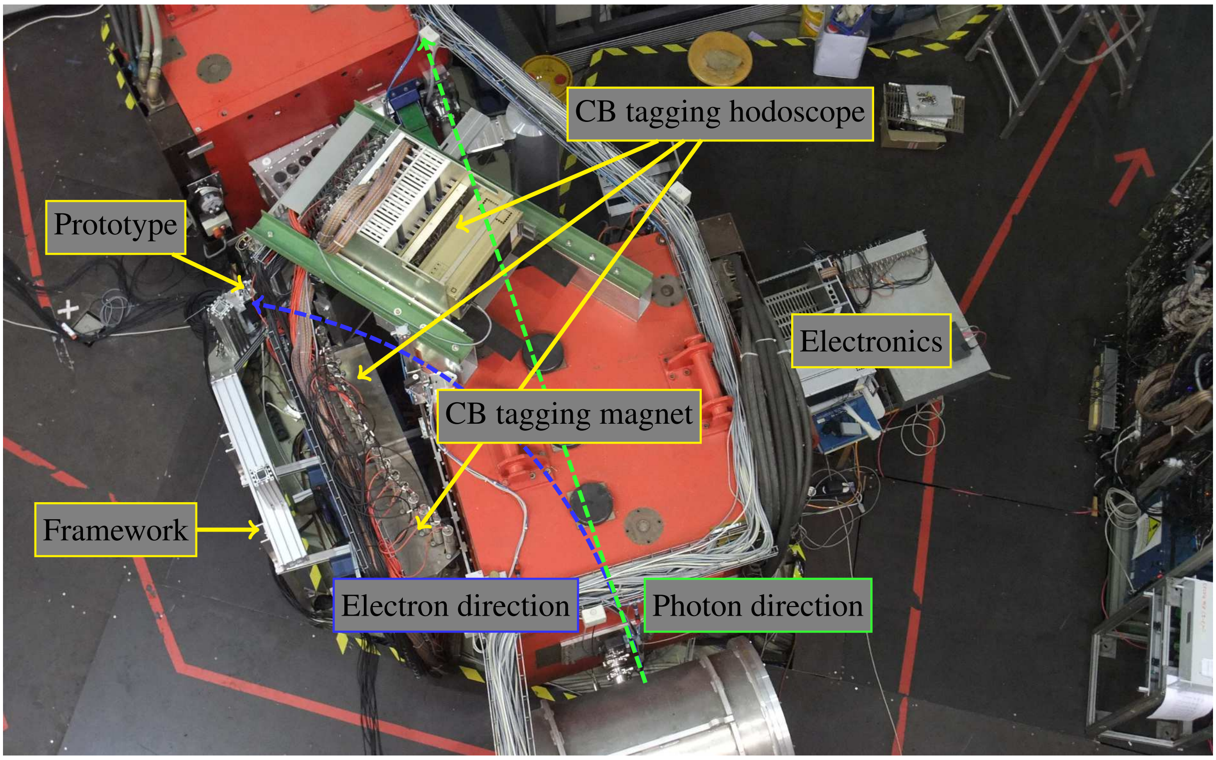

Figure 38. Top view of the CB tagging system. The primary beam gets scattered on the bottom. The produced photons leave the tagging magnet on the top. The scattered electrons are deflected onto the tagging hodoscope. The electronics of the prototype detector (left side) is located to the right of the tagging magnet.

this. Hence the detector was positioned in a way that, by visual judgement, the scintillator bars of the prototype are aligned parallel to the scintillator bars of the CB tagging system. Because this could not be done precisely, two slightly different orientations were used at the position corresponding to high rates. This should assure that at least for one measurement the scintillator bars are aligned almost correctly. Afterwards, the positions were measured relative to the magnet and used for a comparison with simulated data of the expected hit spectrum (see Section 7.4).

6.2.3 First Experimental Data of the Test at the CB Experiment

Figure 39 shows an example of the ADC spectrum of one of the photomultiplier tubes. The broad peak originates from electron hits in the scintillator. The energy distribution in this peaks reflects the varying energy loss described by the Landau distribution. During most events, this particular channel does not detect a signal, because all nine channels can provoke a trigger. This leads to a high pedestal peak, which is clearly separated from the signal peak. Furthermore, some background is visible between the two peaks. In the ideal case, the count rate should be zero in this region. The ADC spectrum will be analysed in more detail in Section 7.1.

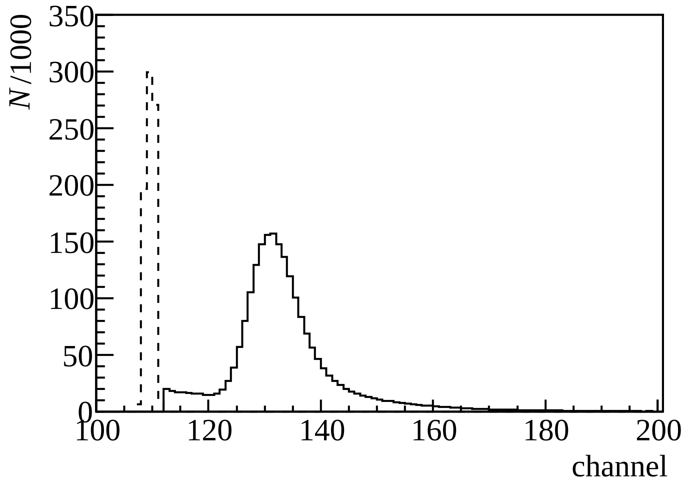

Figure 39. Measured ADC spectrum using channel 5 of the prototype detector during the first test (10^7 events). The dotted line is suppressed by a factor of 10.

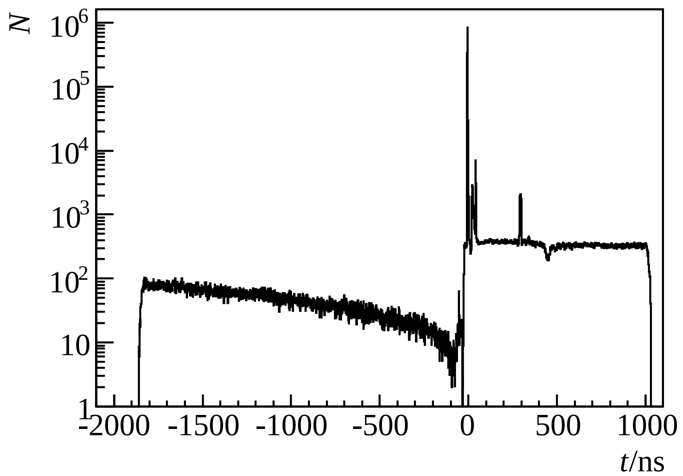

Figure 40. Measured TDC spectrum using channel 5 of the prototype detector during the first test (10^7 events). The y-axis is logarithmic.

Figures 40 and 41 show the TDC spectrum of one channel of the detector. In comparison to the expected form (Figure 34), there appear additional structures. The different features in Figure 41 are explained as follows:

(1) The prompt peak is broadened on the right side (later times), and has a sharp edge to earlier times. This is due to the effect that not only this specific channel can cause a trigger. If one electron hits two overlapping scintillator bars, one of them must be the first one. This one starts the trigger and will always be at the same time in the TDC spectrum (it defines the zero point, except for a constant delay). Due to different cable lengths or a fluctuating transit time in the PMT, the second hit can then be displaced by a small time, leading to a broadening towards later times.

(2) An additional peak appears 30 ns after the prompt peak, which is the dead time of the discriminator. This is caused by the signal of the PMT sometimes showing high spikes

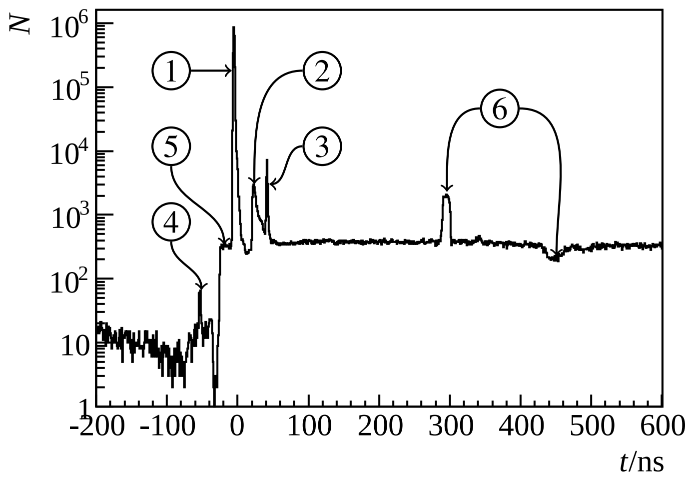

Figure 41. Measured TDC spectrum using channel 5 of the prototype detector during the first test (10^7 events, detail). The y-axis is logarithmic. (1) prompt peak; (2) afterpulses of the PMT; (3) reflections; (4), (5) trigger artefacts; (6) ADC signal. For details, see the text.

after this time. When these are above the threshold, they lead to a second "hit". By adjusting the just roughly set threshold levels, this effect can be avoided.

(3) A second narrow peak appears about 50 ns after the prompt peak. It is caused by a reflection of the signal pulse at the splitter, which could be verified by varying the cable length between PMT and splitter. This reflection sometimes reaches the threshold and causes a false entry in the spectrum. By minimizing the cable length between the PMT and the splitter, the time between the first and the second appearance of the signal can be reduced far below 30 ns, so that the reflection is simply overseen due to the finite double pulse resolution of the discriminator.

(4) This structure arises, when the DAQ opens the trigger just between the real hit and a second hit as in (2) or (3). The second hits defines the zero point and the real hit shows up at smaller times, reflecting the structure of (2) and (3).

(5) The digital output signal of the discriminator has a length of 20 ns. The TDC always sees and records the same edge (leading or trailing) of this signal. If the DAQ resets the trigger during this short time, the FPGA sees an event and immediately causes a trigger, which then can be displaced by up to 20 ns to the real event time. Since the trigger defines the zero point, the real hit time is moved to an earlier time. A hit during this time window of 20 ns cannot release the trigger, which would lead to the exponential structure as explained is Section 6.1.1. As the hit probability during this time is the same as after the trigger, the height of the spectrum up to 20 ns before the prompt peak is the same as after the prompt peak.

(6) This artefact is caused by the ADC. Every time the gate signal reaches the ADC, it emits a small negative (unwanted) pulse on its signal inputs and a higher positive pulse, when the gate signal ends. This pulses travel back through the delay cables and reach the discriminator at some point, increasing or decreasing the signal height which lies on its input. The negative pulse increases the chance that some noise or very weak signal is increased above the threshold, leading to an excess of hits at this time. Vice versa, the positive pulse decreases the height of all signals at this time, leading to a decreased count

rate. The long delay between the prompt peak and this structure can be explained by the way the gate signal travels to the discriminator: The FPGA needs some time to generate the signal, which then goes through a first delay to the ADC. Between the ADC and the splitter there is another long delay, leading to a delay of 240 ns only due to the length of the used cables. Including the delays of the discriminator and the FPGA, a total delay of about 300 ns seems realistic. Nevertheless, this effect has almost no practical consequence, since it is separated by a large time from the prompt peak, which is the only information that will be used in the later experiment. The only effect is the possible increase or decrease of the entry in the corresponding scaler by 1. This is negligible at least for high rates, as the time between two events is larger than 100 µs (see Section 6.1.3), which implies a large number of hits in the scaler. In the later experiment, a different kind of ADC will be used, without the described behaviour.

6.3 Threshold Settings

As shown in Section 6.2.3, the thresholds of the discriminator were set slightly too low. Therefore, even reflections and small pulse fragments were counted as real hits. Since this is as unwanted as throwing away real hits, the adjustment of the thresholds has to be done with care. Clearly, the threshold should lie between the pedestal peak and the signal peak. When these are too close together, it is possible to increase the high voltage of the photomultiplier tubes to within a certain range, which leads to higher signals and to a better separation of the peaks. The reflected signals however are amplified, too.

To get the position the threshold lies in the ADC spectrum, the following method is applied: The ADC always records the energy deposit for all channels, even those where the energy is below the threshold of the discriminator. This is because it suffices that only one channel has a signal above the threshold to start the readout. If a signal is above the threshold, it will not only have an entry in the ADC, but also in the TDC. However, this is only true for those hits arriving at the ADC while the ADC gate is open; hits arriving earlier or later are not counted by the ADC. This time window can be read off in Figure 36. In other words, if there is an entry in the TDC during this time, the entry in the ADC corresponds to a signal above the threshold.

Selecting only those entries in the ADC spectrum with a corresponding entry in the TDC spectrum leads to a distribution as seen in Figure 42. By dividing the number of entries with an entry in the TDC spectrum by the total number of entries for each channel in the ADC, one gets the probability of a signal with a certain energy getting through the discriminator (see Figure 43). Ideally, this *threshold curve* is zero below the set threshold value, and one above. As can be seen, this is not the case here, instead the step is broadened. Reasons for this may be the behaviour of the discriminator itself or an imprecise measurement of the ADC. In the present case, there is a certain chance that very low energetic signals are discriminated, but also that real event signals are not counted. To avoid this, the high voltage of the PMT can be adjusted to increase the gap between pedestal peak and signal peak.

The artefacts seen in Figure 41 are not observed here, because they are correlated to a real signal so that their entry in the ADC lies within the signal peak. Nevertheless, by adjusting the thresholds, some of these artefacts can be avoided (see Section 6.4.3).

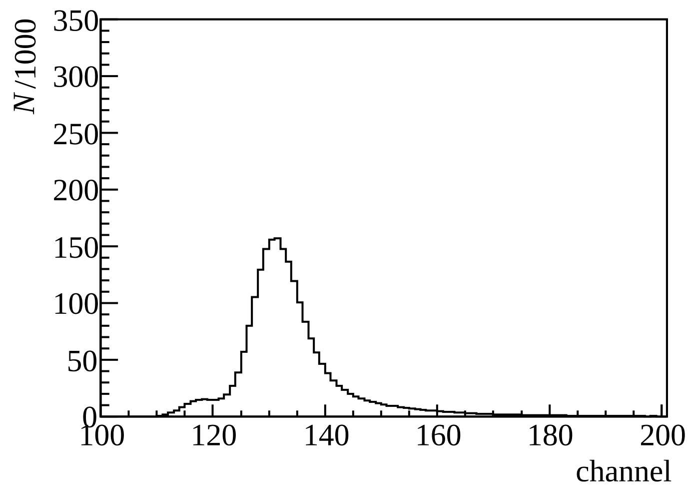

Figure 42. Measured ADC spectrum using channel 5 of the prototype detector, demanding a corresponding entry in the TDC spectrum (10^7 events).

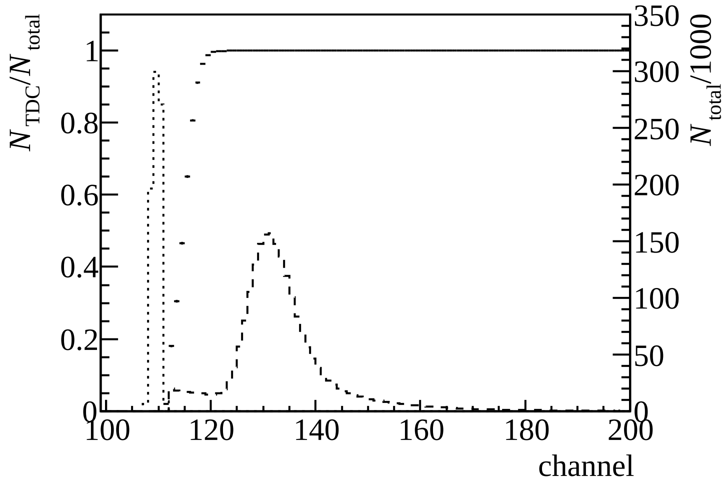

Figure 43. Threshold curve (ratio of the number of hits with entry in the TDC and all hits) for channel 5 of the prototype detector (10^7 events). The dashed/dotted curve is the same as in Figure 39 and belongs to the right axis.

6.4 Test at the BGO-OD Experiment

The second test was performed at the BGO-OD beam line. This test was dedicated to the prototype of the new tagging system, so that effects on other experiments did not have to be considered. This allowed for changing the extracted beam current and for interruptions of the beam to access the detector.

6.4.1 Mechanical Construction and Electronics

The existing holding structure of the old tagging system [Bur96] could be modified easily using aluminium profiles, which allow a placement of the prototype between the old hodoscope and

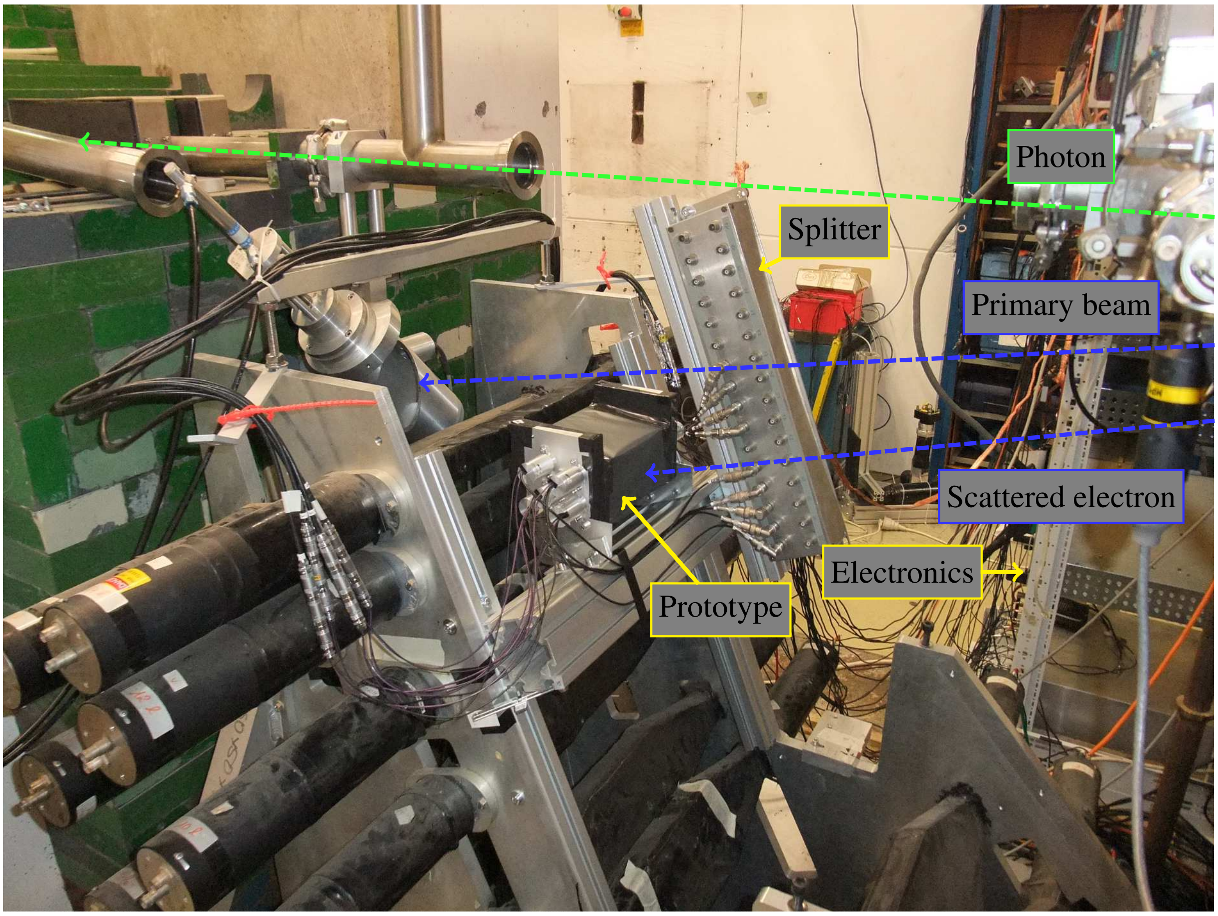

Figure 44. View of the prototype detector mounted in the BGO-OD area.

the tagging magnet (see Figure 44). In contrast to the CB tagging system, the tagging magnet of the BGO-OD experiment is a vertical bend device. The possibility to move the detector easily up and down allows to make measurements at different electron rates.

Figure 45 shows an overview of the complete tagging system as well as the employed electronics. In addition to the modules needed for this test, there are others mounted in the crates which are used for a different experiment. For a detailed description, see Section 6.1.2. To avoid the problems due to reflected pulses as seen in Section 6.4.3, the cable length between the PMTs and the splitter was minimized. In return, longer cables had to be used between splitter and discriminator and ADC, respectively (see also Figure 31, values in brackets). Besides these differences, the electronic setup was the same as in the previous test.

6.4.2 Detector and Beam Settings

The detector was mounted at two different positions along the aluminium profiles, one near its designed position (see Section 4.5.3), the other at the topmost position possible without being hit by the primary electron beam, to reach the maximum possible rate. To identify this position and to avoid hitting the detector frame with the primary beam, the detector was first mounted at a position which lies definitely below that point. Then, a Polaroid film was attached to the back of the prototype, the upper part being exposed to the primary beam. After switching on

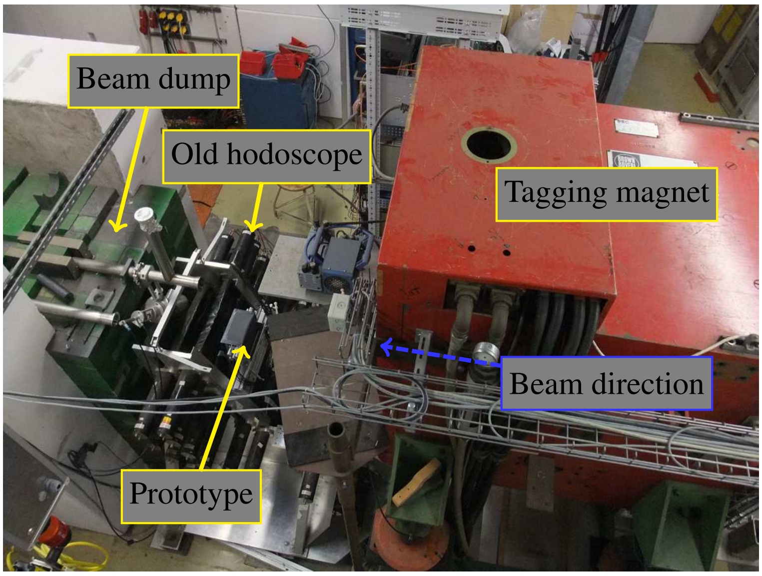

(a)

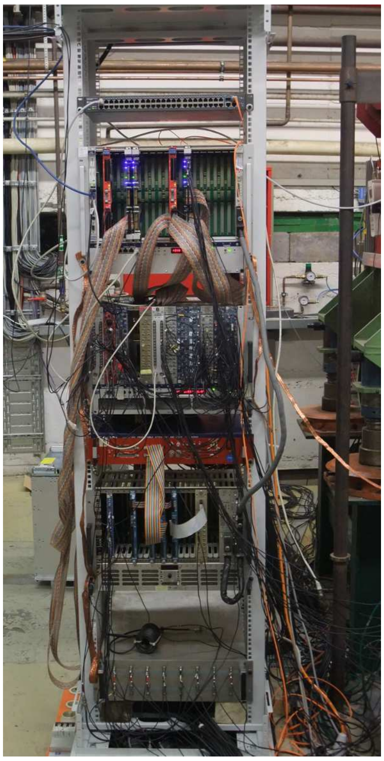

(b)

Figure 45. (a) Overview of the location for the BGO-OD tagging system. The old hodoscope was part of the SAPHIR tagging system. (b) Electronics rack. From top to bottom: VME crate, NIM crate, unused module, CAMAC crate, delay lines.

the electron beam for 1 s–2 s and processing the film, the position of the secondary beam could be clearly identified (see Figure 46). The beam photo also shows electrons which underwent Bremsstrahlung below the secondary beam. The thin line above the spot originates from synchrotron radiation of the electrons which are deflected in the magnetic field.

For this measurement, the thresholds and the high voltage were roughly adjusted using the method shown in Section 6.3. After taking first data, the ADC spectrum for all channels was compared to the same spectrum while requiring a corresponding entry in the TDC. The threshold was then adjusted to fit between the pedestal peak and the signal peak. To make this possible, the high voltage had to be increased for two channels. The resulting values are summarized in Table 6.

For further investigations on the rate stability, an additional test was performed. While the detector was mounted at the topmost position, the rate of electrons leaving the accelerator was varied in a wide range, from below 1 MHz to up to about 15 MHz per channel. This way, measurements for many different rates were acquired without changing the detector position. The results of this test will be discussed in Section 7.2.

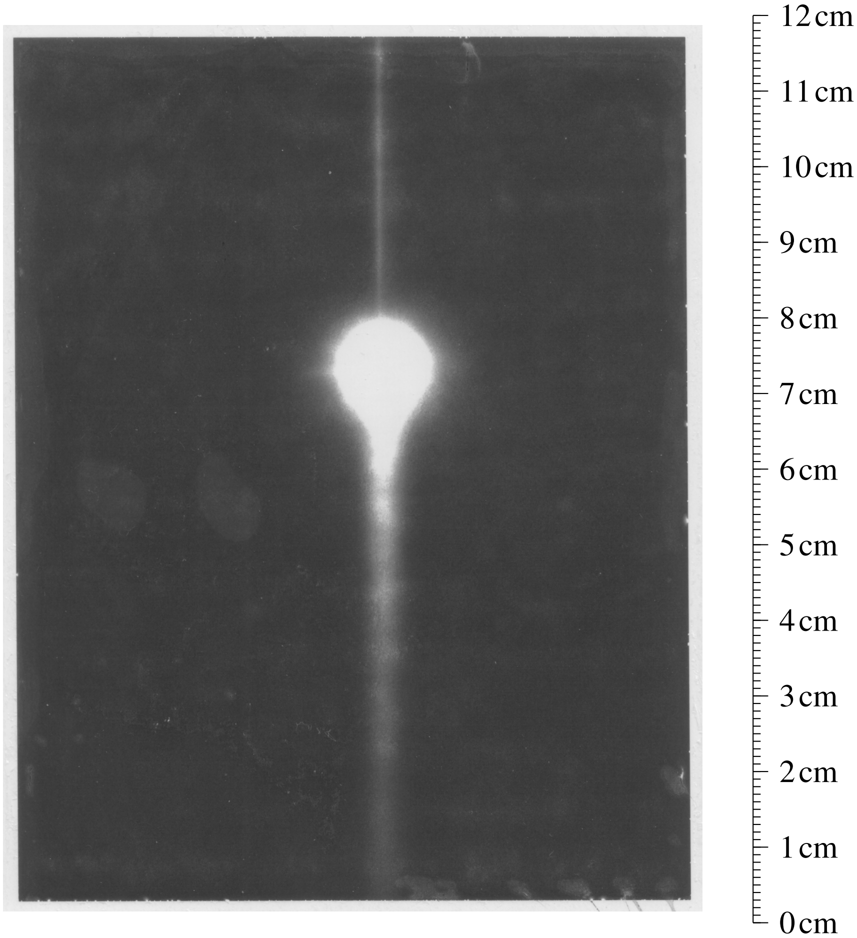

Figure 46. Photograph of the secondary electron beam taken with a Polaroid film (to scale). For details, see the text.

6.4.3 First Experimental Data of the Test at the BGO-OD Experiment

Figure 47 shows an example of the ADC spectrum of one of the channels of the prototype detector. With respect to the previous test (see Figure 39), the pedestal peak is broadened and exhibits a spiky structure. This effect was even more prominent when first tests were made during the build-up of the experiment. The pedestal peak showed more spikes and had a width of more than 20 channels. The situation could be improved by doing the following:

(1) Earthing all electronic components by using a braided copper wire connected to the housings of the crates and the pulse splitter. The splitter box was electrically insulated from the metal construction on which the old hodoscope and the prototype is mounted.

(2) Exchanging the power packs of all crates for different ones.

(3) Connecting the complete electronic setup to another power point, using another phase of the electric power supply.

All these actions resulted in narrowing the pedestal peak. The reason for this is probably an interference-prone electric power supply and high-frequency noise induced by other electronics

PMT	High Voltage/V	Threshold	Electron Rate
1	800	50	lowest
2	800	45	
3	800	50	
4	800	50	
5	800	40	
6	800	45	
7	800	45	
8	850	45	
9	850	40	highest

Table 6. Settings for the test at the BGO-OD site.

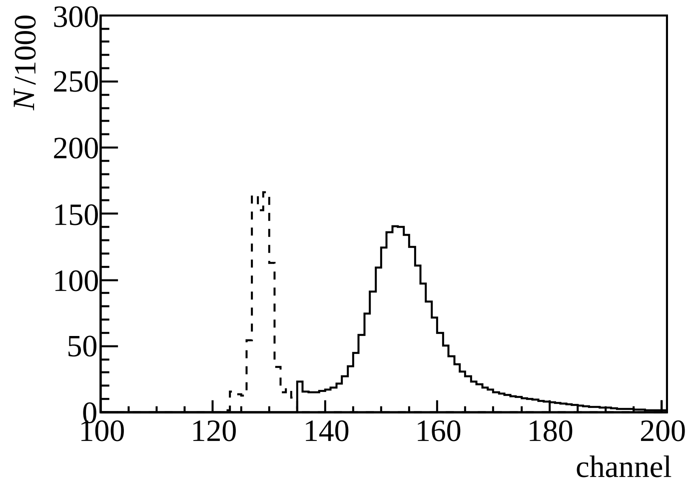

Figure 47. Measured ADC spectrum using channel 5 of the prototype detector during the second test (10^7 events). The dotted line is suppressed by a factor of 10.

sitting nearby. However, the removal of electronic components from the rack which were not used here did not yield a better signal. After the complete test was finished, the entire electrical installation in the BGO-OD area has been renewed. A further test will show if this solves this problem.

Figures 48 and 49 show the TDC spectrum of the same detector channel as in the previous test (Figures 40 and 41). The reflections and the artefact resulting from the thresholds (Figure 41 (2, 3 and 4)) have been removed through the described measures. The first peak in structure (6) is almost vanished, whereas the size of the dip has increased. This supports the justification in Section 6.2.3, as increasing the thresholds decreases the chance, that a pulse accidentally is above the threshold, but increases the chance that a pulse falls below this threshold when lowered by the signal coming from the ADC. The falloff directly behind the prompt peak, which has become visible, results from the finite dead time of the discriminator: Between two hits there is at least a distance of 30 ns.

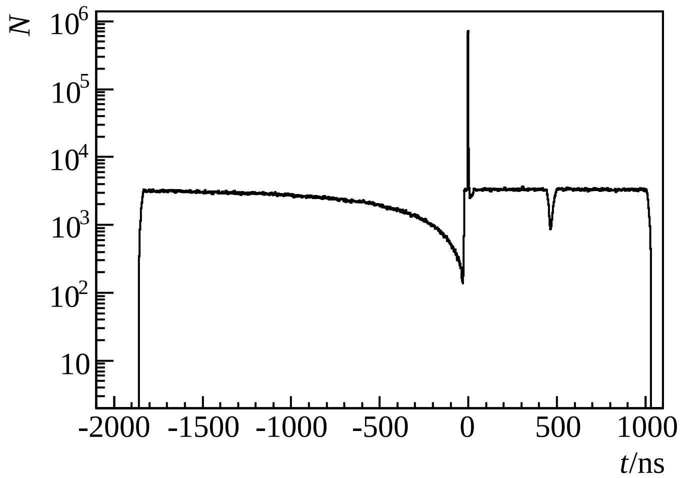

Figure 48. Measured TDC spectrum using channel 5 of the prototype detector during the second test (10^7 events). The y-axis is logarithmic.

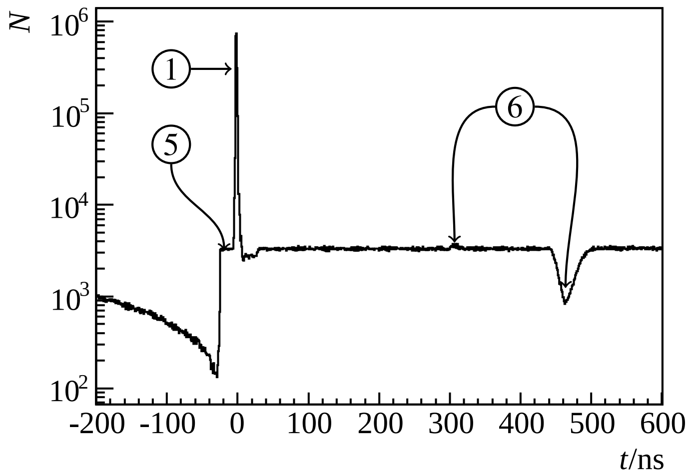

Figure 49. Measured TDC spectrum using channel 5 of the prototype detector during the second test (10^7 events, detail). The y-axis is logarithmic. (1) prompt peak; (5) trigger artefact; (6) ADC signal. For more details, see the text.

7 Data Analysis

In the previous chapter, the experimental setup as well as a first discussion of the raw spectra has been presented. This chapter covers more complex analyses and shows important results about the usability of the prototype detector. Except when otherwise quoted, the data are taken from the dedicated test at the BGO-OD site.

7.1 Detection Efficiency of the Prototype

An important property of a detector is its efficiency. In the context of a tagging system, different efficiency variations should be noted. Here, the *tagging efficiency* is defined as

$$P_\gamma = \frac{N_\gamma}{N_\mathrm{e}}, \tag{40}$$

the ratio of the number of photons impinging on the hadronic target and the number of electrons detected in the tagging system. Ideally, both numbers would be equal to the total number of photons produced in the Bremsstrahlung radiator, $N_\gamma = N_\mathrm{e} = N_{\gamma,\mathrm{total}}$. In reality, they are reduced due to the following reasons:

(1) The photon beam is collimated after leaving the tagging magnet. The amount of photons being removed in the collimator depends on the angular distribution of the Bremsstrahlung process and the dimensions of the collimator, as well as the beam flaw.

(2) The hodoscope only covers a fixed energy range, i.e. electrons outside of this range do not hit the detector in the first place. This is a purely geometrical factor.

(3) The detector itself does not detect necessarily each electron hitting it.

Since the photon rate was not measured, number (1) is not accessible within this experiment. Number (2) can be calculated using the energy range of the detector and the precise Bremsstrahlung cross section. Number (3) is directly accessible within this experimental test. The detector efficiency ε again can be decomposed into two factors: The probability that a temporally isolated electron hitting a scintillator bar leads to a detectable signal from the phototube ($\varepsilon_\mathrm{detect}$) and a factor which arises from the finite dead time of the complete setup including the electronics ($\varepsilon_\mathrm{dead}$):

$$\varepsilon = \varepsilon_\mathrm{detect} \cdot \varepsilon_\mathrm{dead}. \tag{41}$$

The latter will be discussed in Section 7.2, the examination of $\varepsilon_\mathrm{detect}$ follows in this section. Here, $\varepsilon_\mathrm{detect}$ will be simply called ε.

7.1.1 Basic Idea of Efficiency Measurements and its Application to the Prototype

To measure the efficiency of a detector for ionizing radiation, the method depicted in Figure 50 can be used. Electrons leaving some source (e.g. a radioactive source or an electron accelerator)

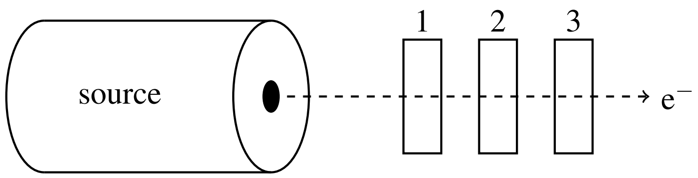

Figure 50. Simple efficiency measurement. Electrons leaving a source penetrate three consecutive detector channels. If a signal is detected in the first and the last channel, there must be a signal in the middle channel, too.

penetrate three consecutive detectors. If one electron has been detected in the first and the last channel, it necessarily also went through the intermediate channel. The efficiency of this intermediate channel is then calculated as

$$\varepsilon_2 = \frac{n_{123}}{n_{13}}, \tag{42}$$

n_{13} and n_{123} being the count rates of coincidences in the particular channels. If the electrons are leaving the source in a straight line as illustrated and background radiation is negligible, also the efficiencies of channel 1 and 3 can be measured in this way. All electrons inducing a signal on a certain channel i, traverse necessarily also the other two channels j and k. The efficiency for channel j is then $\varepsilon_j = n_i/n_{ij}$, ε_k being computed analogously.

However, this method cannot be simply transferred to the prototype detector for several reasons:

(1) The detector was not designed to measure efficiencies, i.e. the arrangement of the scintillator bars differs from the one shown in Figure 50. If the amount of background radiation (see Section 3.5) could be neglected, the efficiency could still be measured for all channels except for the first and the last one. Figure 51 (a) shows a sketch of the detector geometry as well as two exemplary electron trajectories coming from the Bremsstrahlung radiator. It is clear that within the assumption of all electrons coming in this way, the efficiency ε_3 of channel 3 can be obtained. Although it is not sandwiched between two other detectors, all electrons penetrating channel 4 and 2 go through channel 3. Only for channels 1 and 9, no suitable coincidences can be made.

When taking background radiation into account, electrons or other ionizing particles can come basically from any direction. The dotted lines in Figure 51 (b) indicate the regions which are accessible by particles going through channels 7 and 9 or 4 and 2, respectively. Nearly all particles seen by channels 7 and 9 also hit channel 8, making it possible to determine the efficiency ε_8 of this channel. Nevertheless, only a small range which is covered by channels 4 and 2 is covered by channel 3. This implies that only a fraction of all particles seen by channels 4 and 2 can be detected by channel 3. When using the coincident count rates n_{24} and n_{234} to get the efficiency ε_3 of channel 3 as in equation 42, it will be underestimated.

(2) Independently of the geometry, x-ray photons leaving the beam pipe or neutrons coming out of the beam dump can decrease the observed efficiency. The probability for a neutron to interact with the scintillator is so small that it will interact with at most one of the bars. The photons in contrast will be absorbed completely, so that neutrons as well as photons

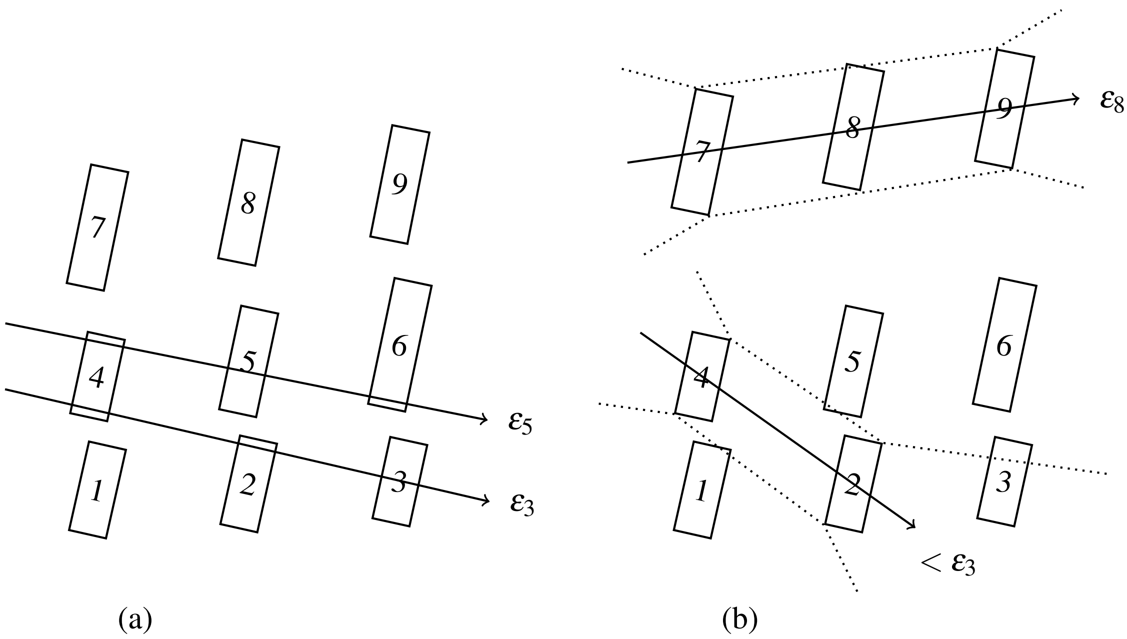

Figure 51. Possible trajectories of electrons in the detector. (a) Side view of the scintillator bars of the prototype detector. The solid lines show trajectories of electrons coming from the radiator. (b) Two sections of the detector. The dotted lines indicate the regions which are accessible for electrons traversing channels 7 and 9 or 2 and 4, respectively.

will only produce a hit in one detector. If two of these particles are detected within a short time in the channels 7 and 9, they will be counted as coincident. In this case it seems that channel 8 missed a particle, reducing the observed efficiency.

(3) It has to be ensured that the discriminator does not miss suitable signals coming from the photomultiplier tubes. This can happen if the thresholds are set above the beginning of the signal peak, thereby removing real electron signals. As will be seen later, this is the case here. Therefore it will be tried in Section 7.1.3 to correct for this.

In the following section, the efficiencies of channels 2 to 8 will be calculated without regarding the mentioned problems. Section 7.1.3 covers the correction of these values for a reduced discriminator "efficiency".

7.1.2 Observed Efficiencies

Before actually calculating the efficiencies, the coincident rates for two and three hits have to be determined. To make sure that every hit of one particle in different channels is counted, hits are considered as coincident, if they are detected within $\Delta t_{\mathrm{coinc}} = 10\,\mathrm{ns}$. This time span should cover all delays of the different channels with respect to each other.

To reduce possible background events, the coincidences are computed as *exclusive*. This means, that a coincidence of two channels implies that no other channel was hit within $\Delta t_{\mathrm{coinc}}$. That way, accidental coincidences are sorted out. For instance, two (background) particles

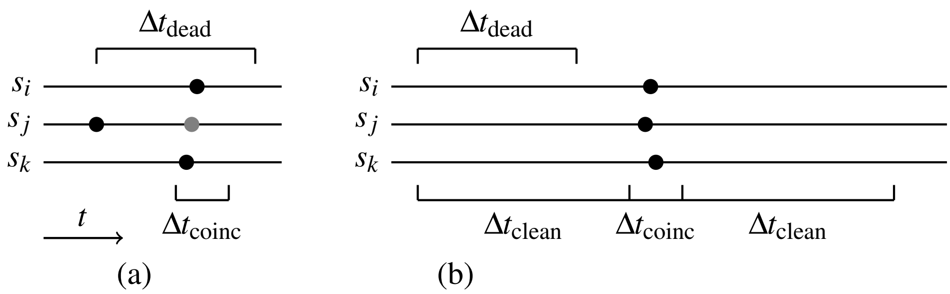

Figure 52. Effect of the dead time on coincidence counting. The dots denote hits in the neighbouring channels $s_{i,j,k}$. The black dots are detected hits. The grey dot is not detected, due to the prior hit on the same channel within the dead time.

hitting channels 4 and 6 without hitting channel 5, also go through other channels with a high probability. With the introduced constraint, such events are filtered out.

Another aspect to be regarded is the dead time of the discriminator $\Delta t_{\text{dead}} = 30\,\text{ns}$. If prior to a coincident hit, one of the detector channels was already struck, it is possible that it is still dead and cannot observe the important electron, see figure 52 (a). This would lead to a reduced count rate of double and triple coincidences, the latter suffering from the higher relative loss. This can be avoided by demanding that during a time $\Delta t_{\text{clean}} = 40\,\text{ns} > \Delta t_{\text{dead}}$ before a coincidence, no channel was busy. To allow for an easier calculation, the same is applied after the coincidence, see Figure 52 (b).

Now the number of coincidences can be extracted from the TDC data by scanning each event and searching for patterns which match the previously mentioned constraints, avoiding errors due to the coincidence time Δt_{coinc} and the dead time Δt_{dead}. The data sample (10^7 events) taken with the lowest rate is used to avoid too high a loss due to dead time effects. Because of the exclusive coincidence counting, equation 42 has to be slightly modified:

$$\varepsilon_2 = \frac{N_{123}}{N_{13} + N_{123}} = \frac{1}{1 + \frac{N_{13}}{N_{123}}}, \tag{43}$$

N_{13} and N_{123} now being the number of exclusive coincidences extracted from the data. The statistical error σ_{ε_2} on ε_2 is calculated assuming Poisson distributed numbers:

$$\sigma_{\varepsilon_2} = \varepsilon_2^2 \sqrt{\frac{N_{13}}{N_{123}^2} + \frac{N_{13}^2}{N_{123}^3}} = \varepsilon_2^2 \sqrt{\frac{N_{13}}{N_{123}^2}\left(1 + \frac{N_{13}}{N_{123}}\right)} \simeq \sqrt{\frac{N_{13}}{N_{123}^2}} \quad \text{if } \varepsilon_2 \simeq 1. \tag{44}$$

Figure 53 shows the number of coincidences for each combination of two channels. As one would expect, the coincidences between neighbouring channels clearly dominate. Coincidences of two hits in the same channel do not appear, since $\Delta t_{\text{coinc}} < \Delta t_{\text{dead}}$. Similarly, Figure 54 shows coincidences of three channels, one of them being fixed to 5. Triple coincidences for the other channels can be found in Appendix B. The coincidences of non neighbouring channels can originate in a detection efficiency for electrons which is smaller than one and background radiation. E.g., neutrons are detected inherently with a small probability $\varepsilon \simeq 10\,\%$ (see Section 3.5), making is possible to penetrate multiple scintillator bars without depositing charge in the middle one.

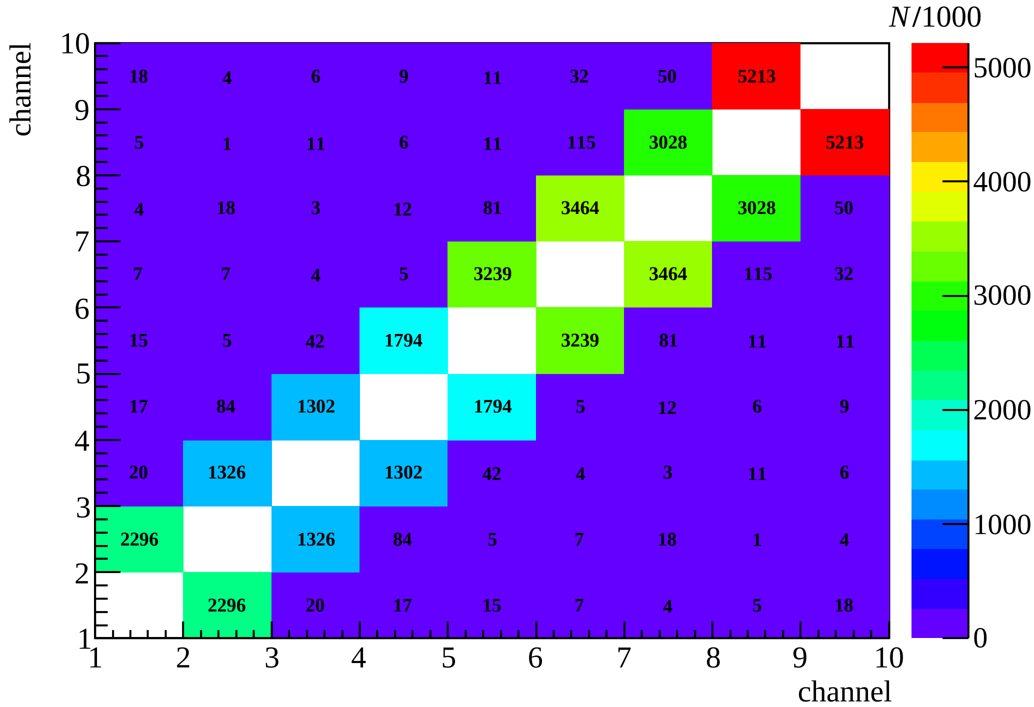

Figure 53. Exclusive coincidences of each combination of two channels. The colour code and the number in each cell show the number of coincidences for the according combination of channels. The numbers in the cells have to be multiplied by 1000.

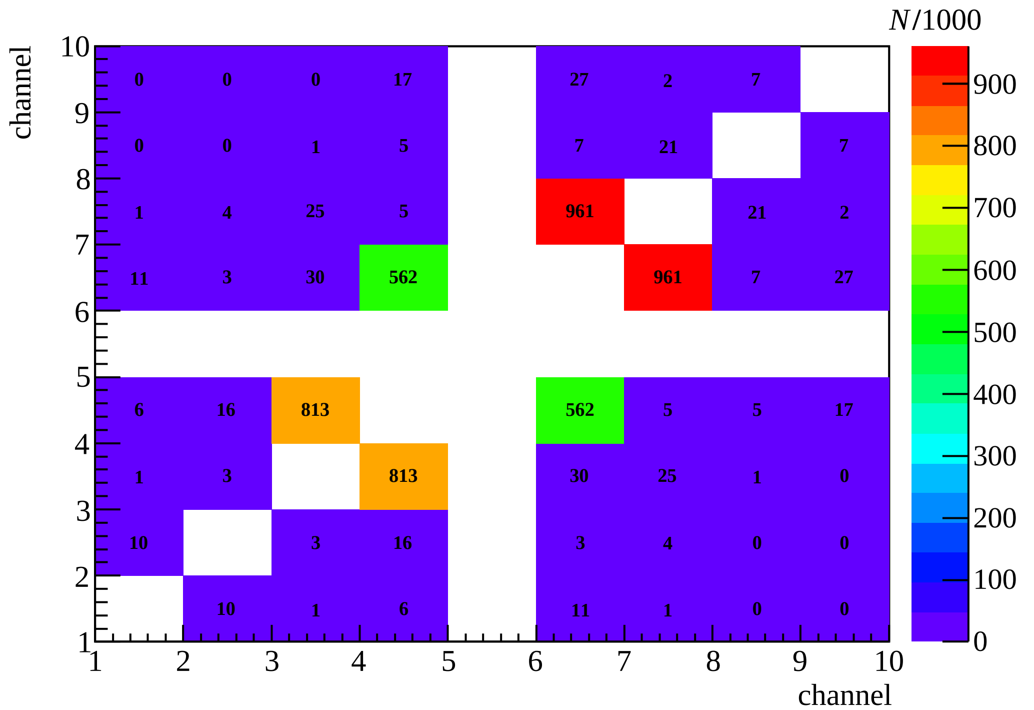

Figure 54. Exclusive coincidences of each combination of two channels and channel 5. The colour code and the number in each cell show the number of coincidences for the according combination of channels. The numbers in the cells have to be multiplied by 1000.

channel	coincident channels	ε	σ_ε
2	1, 3	0.9706	0.0002
3	2, 4	0.9102	0.0003
4	3, 5	0.9507	0.0002
5	4, 6	0.9918	0.0001
6	5, 7	0.9227	0.0003
7	6, 8	0.9280	0.0002
8	7, 9	0.9580	0.0002

Table 7. Efficiencies calculated from the coincidences.

The results from using equations 43 and 44 are summarized in Table 7. The efficiencies for channels 2 and 5 are quite close to one, the others show deviations of 5 % and more. As described in Section 7.1.1, this is at least expected for channels 3, 4, 6 and 7 due to geometrical considerations. The observed values depend on the actual amount of background radiation. This implies at least for channel 8 that either the discriminator throws away many signals or the efficiency is actually comparably low. This will be checked in the next section.

7.1.3 Correction for Discriminator Thresholds

The efficiencies computed in the last section differ, apart from geometrical and background effects, significantly from one, which is not expected for an electron detector. It is highly unlikely that electrons do not lose energy when penetrating a scintillator bar (see Section 2.5.3). However, it is possible that the thresholds of the discriminator are set so high, that signals which belong to a real hit are not being detected. In this section, the attempt is made to estimate the fraction of the event signals which do not go above the threshold, called *discriminator efficiency* $\varepsilon_{\text{disc}}$. To do this, two things are needed: The threshold curves of the discriminator $t(x)$ for each detector channel, computed as in Section 6.3, and the expected energy spectrum $s(x)$ for electron signals in the ADC. $t(x)$ can be interpreted as the probability that a signal corresponding to the signal height x in the ADC is counted by the discriminator. $s(x)$ is the number of entries in ADC channel x which is expected for pulses originating in electrons hitting the corresponding scintillator bar. The real spectrum always includes some noise $n(x)$, which has to be removed before doing further calculations. The total number of electrons can then be calculated as

$$N_{\text{total}} = \sum_{x=x_{\min}}^{x_{\max}} s(x). \tag{45}$$

The total number of particles expected to be registered by the discriminator is

$$N_{\text{disc}} = \sum_{x=x_{\min}}^{x_{\max}} s(x) \cdot t(x). \tag{46}$$

If these quantities are known, the discriminator efficiency is computed as follows:

$$\varepsilon_{\text{disc}} = \frac{N_{\text{disc}}}{N_{\text{total}}}. \tag{47}$$

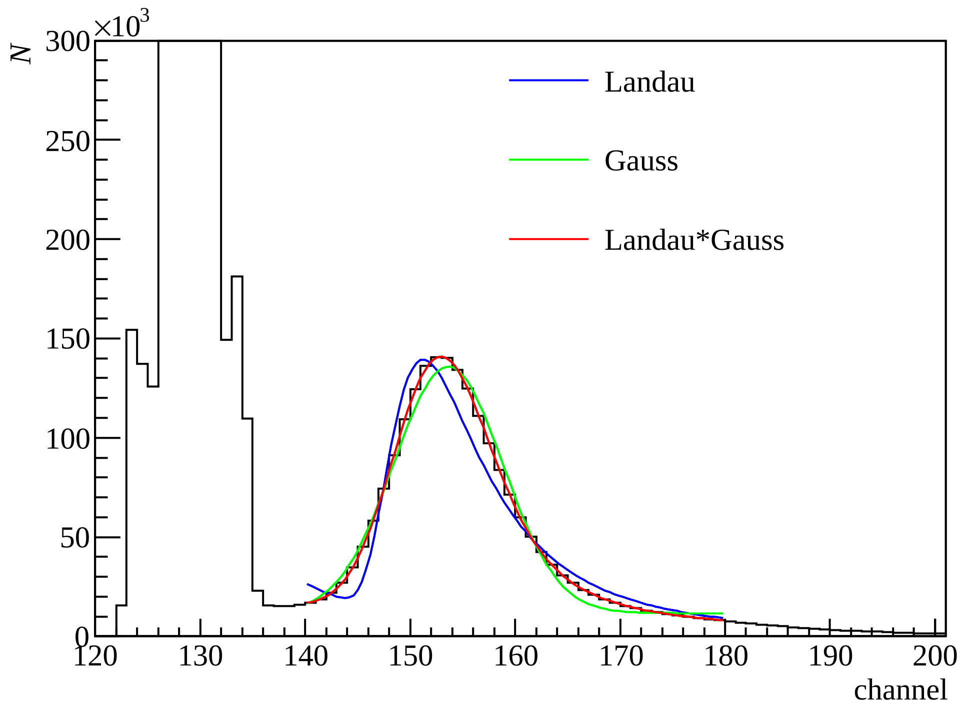

Figure 55. ADC spectrum with fitted functions. Each fit includes an exponential function to describe the background noise. Neither the Landau nor the Gauss function fit the observed spectrum. For the convolution, $\chi^2/NDF \simeq 2$.

The shape of the signal peak in the ADC spectrum is expected to follow a Landau distribution [Kle05]. Therefore, an attempt to fit a Landau function to the ADC spectrum as shown in Figure 55, including an exponential function to match the background, is made. Obviously, this does not work out, which becomes evident when looking at the pedestal peak. This peak corresponds to a single charge $Q = 0$ and is expected to be only at $x(Q = 0) = x_{\text{pedestal}}$, see Equation 36. If the ADC spectrum for $Q = 0$ is broadened, it is obvious that all other charge deposits are broadened, too. This leads to the assumption that the signal $s(x)$ appears to the ADC as the convolution $(s * d)(x)$, where $d(x)$ has the shape of the pedestal peak. Since it is easier to accomplish, the distortion $d(x)$ is approximated as a Gaussian

$$d(x) \sim \mathrm{e}^{-\frac{x^2}{2\sigma}}. \tag{48}$$

Thus, the function to be fitted is

$$f(x) = c_1(s * d)(x) + c_2\mathrm{e}^{-c_3 x} = c_1((s+n) * d)(x), \tag{49}$$

where $n(x)$ is the undistorted background ($c_1(n * d)(x) = c_2 \exp(-c_3 x)$). The convoluted function fits the observed spectrum quite well, with $\chi^2/NDF \simeq 2$ for the shown region. For high x, the spectrum is overestimated due to the Gaussian approximation, as the pedestal peak falls faster to zero than the Gaussian.

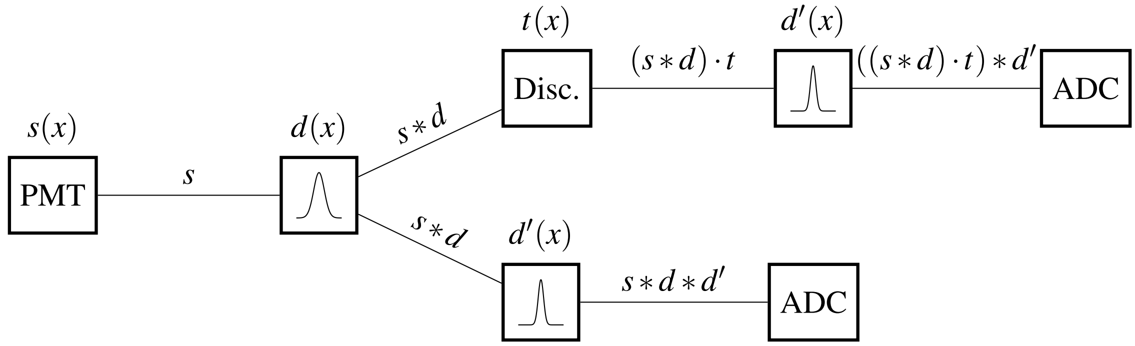

Figure 56. Pulse distortion in the ADC and the discriminator. $s(x) =$ signal generated by the PMT, $d(x) =$ signal distortion common to ADC and discriminator , $d'(x) =$ additional distortion of the ADC, $t(x) =$ threshold curve of the discriminator. The terms on the lines indicate the current signal shape.

Until now it was assumed that both the discriminator and the ADC see the same distortion. The ADC however can introduce another distortion or uncertainty $d'(x)$ due to the charge measurement. The complete signal seen by the ADC is then

$$s_{\mathrm{ADC}}(x) = (s * d * d')(x). \tag{50}$$

This does not change the overall shape of the signal, since the Gaussian distribution is invariant under a convolution. The signal seen by the discriminator is still $s_{\mathrm{disc}}(x) = (s * d)(x)$. When selecting only those hits lying above the discriminator threshold, $t(x)$ has to be applied to $s_{\mathrm{disc}}(x)$. Yet, when looking at this spectrum in the ADC, it is distorted by $d'(x)$:

$$s^{\mathrm{above}}_{\mathrm{ADC}}(x) = (((s * d) \cdot t) * d')(x). \tag{51}$$

The complete path of the signal from the PMT to the ADC is summarized in Figure 56. Now two cases can be considered, depending on the impact of $d'(x)$.

$d'(x)$ negligible ($d'(x) = \delta(x)$)

The complete spectrum $s(x) + n(x)$ is seen in the same way by the ADC and the discriminator. By dividing the spectrum with hits above the threshold by the complete spectrum, one gets the threshold curve $t(x)$:

$$\frac{s^{\mathrm{above}}_{\mathrm{ADC}}(x) + n^{\mathrm{above}}_{\mathrm{ADC}}(x)}{s_{\mathrm{ADC}}(x) + n_{\mathrm{ADC}}(x)} = \frac{(((s+n) * d) \cdot t)(x)}{((s+n) * d)(x)} = t(x). \tag{52}$$

The spectrum originating from real hits $s_{\mathrm{ADC}}(x) = (s * d)(x)$ is found, by fitting $f(x)$ to the complete ADC spectrum. The exponential term is left out to separate the signal $(s * d)(x)$ from the noise $(n * d)(x)$. Replacing $s(x)$ by $(s * d)(x)$ in Equations 45 and 46 to include the distortion gives the discriminator efficiency:

$$\varepsilon_{\mathrm{disc}} = \frac{\sum_{x=x_{\min}}^{x_{\max}} (s * d)(x) \cdot t(x)}{\sum_{x=x_{\min}}^{x_{\max}} (s * d)(x)}. \tag{53}$$

channel	coincident channels	ε	σ_ε	$\varepsilon_{\text{disc}}$	$\sigma_{\varepsilon_{\text{disc}}}$	ε'	$\sigma_{\varepsilon'}$
2	1, 3	0.9706	0.0002	0.9653	0.0001	1.0055	0.0003
3	2, 4	0.9102	0.0003	0.9763	0.0001	0.9323	0.0003
4	3, 5	0.9507	0.0002	0.9942	0.0000	0.9563	0.0003
5	4, 6	0.9918	0.0001	0.9935	0.0000	0.9984	0.0001
6	5, 7	0.9227	0.0003	0.9873	0.0001	0.9346	0.0003
7	6, 8	0.9280	0.0002	0.9931	0.0000	0.9344	0.0002
8	7, 9	0.9580	0.0002	0.9597	0.0001	0.9982	0.0002

Table 8. Discriminator efficiencies, uncorrected and corrected detector efficiencies.

$d'(x)$ not negligible

If however $d'(x)$ significantly distorts the signal seen by the ADC, it not possible to get the real threshold curve $t(x)$:

$$\frac{s_{\text{ADC}}^{\text{above}}(x)+n_{\text{ADC}}^{\text{above}}(x)}{s_{\text{ADC}}(x)+n_{\text{ADC}}(x)} = \frac{((((s+n)*d)\cdot t)*d')(x)}{((s+n)*d*d')(x)} \equiv t'(x) \neq t(x). \tag{54}$$

When using $t'(x)$ instead of $t(x)$ to calculate $\varepsilon_{\text{disc}}$, the value will differ from the real value. The effect can be understood qualitatively: Due to $d'(x)$, the threshold curve will seem broader than it actually is. If the curve is near the event peak, it will cut further into higher energies, while lower energies will only be affected slightly, since these are barely present below the threshold (see also Figure 43). In total, the number of events expected to be seen by the discriminator is reduced, leading to an underestimation of $\varepsilon_{\text{disc}}$.

Correcting the detector efficiency ε

Having calculated $s(x)$ and $t(x)$, Equations 45–47 are now used to determine $\varepsilon_{\text{disc}}$, assuming $d'(x)=\delta(x), t'(x)\simeq t(x)$. The results are summarized in Table 8. ε' is the corrected detector efficiency,

$$\varepsilon' = \frac{\varepsilon}{\varepsilon_{\text{disc}}}. \tag{55}$$

The value greater than one implies an underestimation of the discriminator efficiency $\varepsilon_{\text{disc}}$, as the probability to detect a particle clearly cannot be greater than 100 %. When $\varepsilon_{\text{disc}}$ is measured exactly, the real efficiency $\varepsilon_{\text{detect}}$ is simply given by

$$\varepsilon_{\text{detect}} = \varepsilon'. \tag{56}$$

If $\varepsilon_{\text{disc}}$ is underestimated, the only conclusion which can be made, is

$$\varepsilon \leq \varepsilon_{\text{detect}} \leq \varepsilon'. \tag{57}$$

The maximum observed uncorrected efficiency is $\varepsilon_{\max} = 0.992$, the maximum corrected efficiency is $\varepsilon'_{\max} = 1.005$. These values show that the design of the detector in principle allows for a detection efficiency of

$$0.992 \leq \varepsilon_{\text{detect}} \leq 1.000. \tag{58}$$

Possible reasons for the smaller efficiency of the other channels can be the geometrical arrangement (Section 7.1.1) or flaws in the assembling of the detector like air in the glued joint between the scintillator and the light guide (see Section 2.5.3). To achieve the maximum efficiency for all channels, the production of the light guides and the scintillator bars as well as the assembling has to be done with more care. Especially, air must not enter the glued joint. An additional increase of the efficiency is expected due to the new scintillator material which will be used for the final detector.

7.2 Electron Rate Stability

As mentioned in Chapter 3.3, it is desirable to use the tagging detector at rates as high as possible. Due to the energy distribution of Bremsstrahlung photons $\mathrm{d}N_\gamma \sim \mathrm{d}E_\gamma/E_\gamma$, the rate is not equally distributed over the complete hodoscope, low energy photons being emitted more often than high energy photons. If the tagging system covers photon energies of $10\,\%$–$90\,\%E_0$, about $7\,\%$ of all electrons hit the highest channel (corresponding to the lowest photon energy), assuming an energy width of 50 MeV. In this section, the behaviour of the prototype for high rates will be investigated. The principal reason for a decreased rate stability is the dead time of the involved components as explained in the next section. In the subsequent sections, different methods to investigate the behaviour of the detector at high rates are presented.

7.2.1 The Effect of Dead Times on Observed Rates

It is expected that at some point the rate seen with the prototype will become lower than the actual rate, due to the dead time τ of the used components. One distinguishes two different kinds of dead time: extendible and non-extendible dead time. If the dead time is extendible, a second hit during this period will lead to an extension of the dead time by τ, beginning at the time of the second hit. Photomultiplier tubes exhibit such an extendible dead time. A second hit arriving before the signal has fallen down just adds up to the signal. This way the signal height is increased, but the second hit cannot be separated from the first one. Components with a non-extendible dead time are simply "blind" after one hit occurred. A second hit within the dead time will have no effect. This is the case for the discriminators used here, which have a dead time of $\tau = 30\,\mathrm{ns}$. The effect of the dead time on the observed rates is given in Equations 59 and 60 for the non-extendible and the extendible case, respectively [Mü73].

$$n = \frac{r}{1 - r\tau}, \tag{59}$$

$$n = \frac{r}{\exp(r\tau)}, \tag{60}$$

where n is the observed rate and r is the real rate. If however a combined system is looked at, the situation becomes more complicated. In the present case, an extendible dead time τ_{PMT} (the effect of the PMT) is followed by a non-extendible dead time τ_{disc} (the effect of the discriminator). This leads to the following behaviour [Mü73]:

$$n = \frac{r}{r\left(\tau_{\mathrm{disc}} - \tau_{\mathrm{PMT}}\right) + \exp\left(r\tau_{\mathrm{PMT}}\right)}. \tag{61}$$

Of course, this only holds as long as $\tau_{\mathrm{disc}} > \tau_{\mathrm{PMT}}$. If the first dead time is longer than the second one, the second one has no effect. After determining $n(r)$ in the next sections, the attempt is made to extract the dead time by using Equations 59 to 61.

7.2.2 Measurement Principle

For the following analysis, data were taken at different rates between 0.5 MHz and 12 MHz per channel. The rate observed directly with the prototype detector can be extracted from the scalers (see Section 6.1.1). To obtain the real rate, three different methods are used:

(1) During the experiment, the electron current leaving ELSA and entering the experimental hall was measured with a high frequency resonator [Pus10, Sch09] and monitored by the slow control. As this current is proportional to the rate of electrons hitting the tagging system, it can be used as measure of the rate of Bremsstrahlung electrons. The absolute value of the rate, however, is unknown.

(2) The second possibility is to further investigate the TDC spectrum. Since the distances between two hits follow an exponential distribution, the shape of the distribution of temporal distances can be used to extract the rate. This rate is indeed the real rate, as the only effect of the dead time is the non-existence of small distances. Larger temporal distances are not affected.

(3) One can take advantage of the fact that the different channels of the detector are exposed to different rates. Since low rates are effected less by the dead time than high rates, the rate of the lowest channel in electron energy can be used as an estimate of the real rate, apart from a constant normalisation factor.

In the following sections, these methods will be explained in more detail and the results will be presented.

7.2.3 Electron Beam Structure

When analysing the experimental data with respect to electron rates, one has to take care of the temporal structure of the beam extracted from ELSA. When the stretcher ring is filled, electrons are continuously extracted for about 4 s. After refilling the stretcher ring with electrons from the booster synchrotron for about 1 s[43], the extraction starts again [Hil06]. One extraction period is called *spill*. Figure 57 shows two selected complete spills taken from the whole measurement of about 2 h, where N is the number of hits in the scaler of channel 5. Most spills show a structure like the first complete one shown here. The rate rises very fast and stays almost constant after a small drop. In the end it drops to zero again. Some spills differ from this structure with the rate changing during the complete spill time, e.g. as the second complete spill in Figure 57. During this test, roughly 10 %–20 % of all spills deviated visibly from the ideal shape. These structures imply two things when measuring rates:

(1) The rate must not be computed by simply summing the hit counts for a long time and dividing by this time. This averaging would lead to an underestimation of the rate actually seen by the detector. Therefore, the rate is computed for each spill individually.

[43] Actually, these numbers can vary. The given periods are valid for this test.

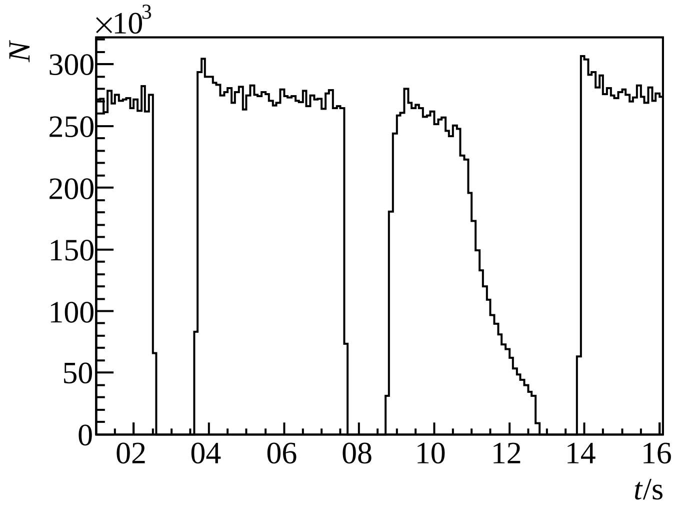

Figure 57. Spill structure of the electron beam. N is the accumulated number of entries in one scaler during $\Delta t_{\text{bin}} = 0.1\,\text{s}$.

(2) The spills themselves show a structure. Only spills with an almost constant rate may be selected. The rising and falling edge should be left out.

Keeping this in mind, suitable spills are defined with the following constraints:

(1) A spill begins when the rate, measured in the scaler, goes above 50 kHz and ends when the rate falls below this value.

(2) Only spills with a length between 3 s and 5 s are used.

(3) The leading edge is cropped by 1.5 s to remove the bump at the beginning of a spill. The trailing edge is cropped by 0.5 s.

(4) The rate averaged over each 0.5 s interval must not deviate by more than 20 % from the mean rate of the spill.

These values were chosen to minimize the error of the rate determination and to maintain a sufficient number of spills. The rate for each channel and spill is then obtained by summing the scaler entries and dividing by the sum of the entries in the 1 MHz scaler, which is the time reference.

7.2.4 Scaler versus Primary Electron Current

The measurement of the electron current which leaves the stretcher ring and enters the BGO-OD experiment is completely independent from the data collection of the tagging prototype. On one hand, this is an advantage, since the measurements cannot influence each other. On the other hand, it is difficult to assign to each rate measurement the correct current measurement. Both values are stored together with a timing information, which can yet be different. The

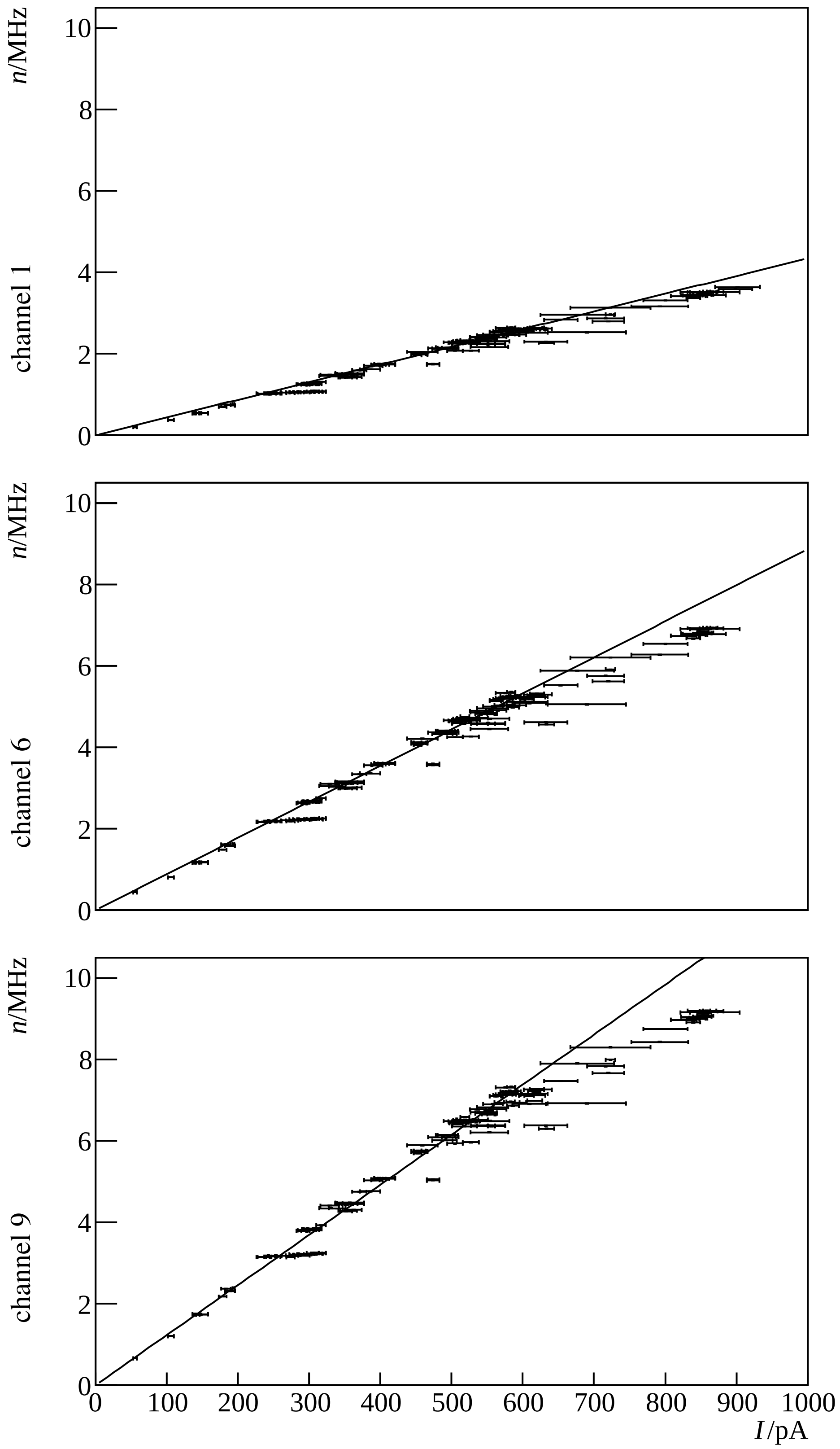

Figure 58. Scaler rate of channels 1, 6 and 9 vs. extracted electron current. The other channels can be found in Appendix C. Shown are the statistical errors; the errors of the scaler rate are too small to be visible in this plot. The line is fitted for I up to 600 pA.

current measurement is stored some seconds after the spill ended, but the displacement is not constant, making the measurement very error-prone. The statistical error of this ambiguous current measurement is estimated by the standard deviation of three consecutive measurements, the middle one most probably belonging to the corresponding spill. The uncertainty is quite large, as can be seen in Figure 58. There, the rate measured with the scaler is plotted against the extracted current. A line is fitted for currents up to 500 mA and shows roughly the range within which the rate increases linearly with the current.

It is conspicuous, that the rate increases linearly with the current up to about 600 pA and then starts rising more slowly, independently of the channel. This is in contrast to the expectation, that this point lies at about the same rate for each channel. This behaviour can be understood at least qualitatively. When a higher current is extracted from ELSA, the beam position may be shifted [Gen99]. If the beam is shifted upwards with increasing current, the distance between the tagging hodoscope and the electron beam becomes larger, implying that the electron energies seen by a fixed detector channel decrease. Because of the Bremsstrahlung cross section $\mathrm{d}\sigma \sim \mathrm{d}E_\gamma/E_\gamma = \mathrm{d}E_\mathrm{e}/(E_0 - E_\mathrm{e})$, this also leads to a decrease of the rate in the detector, explaining the observed discrepancy in Figure 58. The correlation between beam shift and current changes with the exact adjustments of ELSA. As these were changed during the data taking to allow for higher currents, no exact prediction can be made about the electron rate hitting the detector, nor can the maximum possible rate be determined.

7.2.5 Scaler versus TDC

The second method makes use of the exponential distribution of the temporal distances of hits in one detector channel. The shape of this distribution is independent of the dead time τ, since this only cuts out small time spans while leaving the remain unaffected. When calculating distances from the times in the TDC, two things have to be considered:

(1) Only a part of the complete time span measured by the TDC is suitable for this. Immediately before the prompt peak, short distances are suppressed (see section 6.1.1, TDC). At about 300 ns, the spectrum is distorted by the ADC (see Figure 49). Including these parts into the calculation would lead to a false reconstruction of the rate. Because the prompt peak contributes a large amount of the total hits in the spectrum, the used range starts immediately before the prompt peak and ends immediately before the distortion by the ADC.

(2) Not all hits of the selected range t_1–t_2 may be used as starting point for a distance measurement. When starting shortly after t_1 in Figure 59 (a), longer distances to the next hit can be measured as when starting later (b). Starting at a later time, shorter distances (Δt_s) are still measured, whereas longer distances (Δt_l) are not counted, leading to an overall suppression of long distances and an overestimation of the real rate. To avoid this, a maximum distance Δt_max has to be defined. Only distances up to Δt_max may be counted and only if the first hit occurred before $t_2 - \Delta t_\mathrm{max}$ (c). When the first hit arrives after $t_2 - \Delta t_\mathrm{max}$, no distance is measured (d). This way, distances up to Δt_max are counted without distortion.

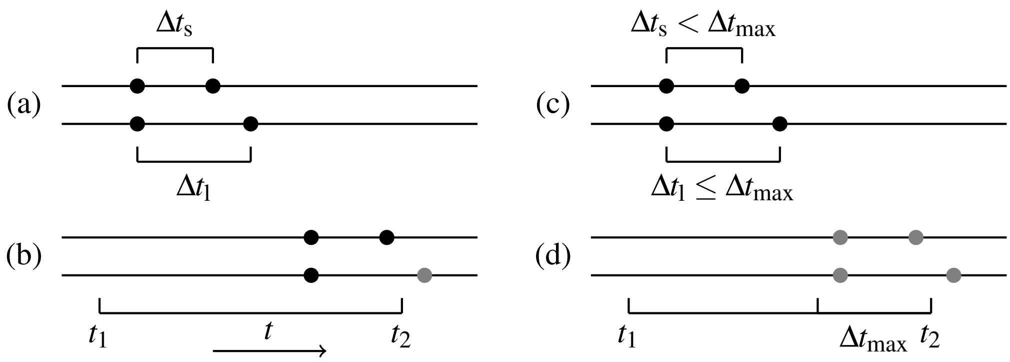

Figure 59. Measurement of temporal distances. The black dots represent entries in the scaler which are used for the calculation of distances, the grey dots are not used. Without additional constraint, short temporal distances are favoured over long distances (a). When introducing a maximum distance, this issue no longer appears (b). For details, see the text.

Since only few distances can be measured for each event, one spill does not provide enough data to calculate the rate reliably. Therefore the data are collected for all spills with a similar rate in the scaler with steps of 0.5 MHz. For each step, the real rate is then computed by fitting an exponential function to the spectrum of distances. Still, the statistical error of the real rate is quite large (Figure 60), making the results barely usable, at least for channels 1–4. The plots for channel 5 and 8 show an expected behaviour, as the scaler rate rises linearly with the real rate up to about 4 MHz and then starts to lose hits. This is also the case for channel 9, but just as for channels 6 and 7, the rate measured with the TDC decreases with respect to the rate from the scaler starting at some point. For channel 9, the TDC starts to lose hits starting at about $r = 10\,\text{MHz}$. This is not a failure of the prototype detector itself, but rather a limitation of the TDC, as will be explained below.

The HPTDC chips [Chr04] on the TDC provide for four groups of eight input channels, making 32 input channels in total. For each group, there is a single buffer collecting the data from all channels of this group. This buffer is read out with a clock rate of 40 MHz, thus limiting the total rate for one group to this value. However, this rate can be achieved only if all hits arrive with the same temporal distance, which is not the case here. If the rate becomes too high for the TDC, hits will be lost first in the last channels of one group, explaining why channels 6, 7 and 9 are affected the most. Channels 1–7 belong to one group and channel 8 and 9 to another (see also Appendix C for the plots for all channels).

To circumvent these limitations, the channels of the detector can be mapped in a non trivial way to the channels of the TDC. The final tagging hodoscope will have about 100 channels. Only a few of them will be exposed to rates critical for the TDC. By grouping one of these together with seven low rate channels, the total rate of one group can be limited. The maximum rate for a single channel is 10 MHz [Chr04], making rates up to 4 MHz possible, even for randomly distributed hits, with a relative loss of less then 10^{-3} [Chr04]. The second issue to consider is the correlation between the channels in one TDC group. If the channels are highly correlated, which is the case for geometrically neighbouring channels, the maximum rate is further decreased, as multiple hits will then occur at the same time. So, no neighbouring detector channels should be put in one group in the TDC. The mapping between TDC channel and detector channel has then to be shifted to the data analysis.

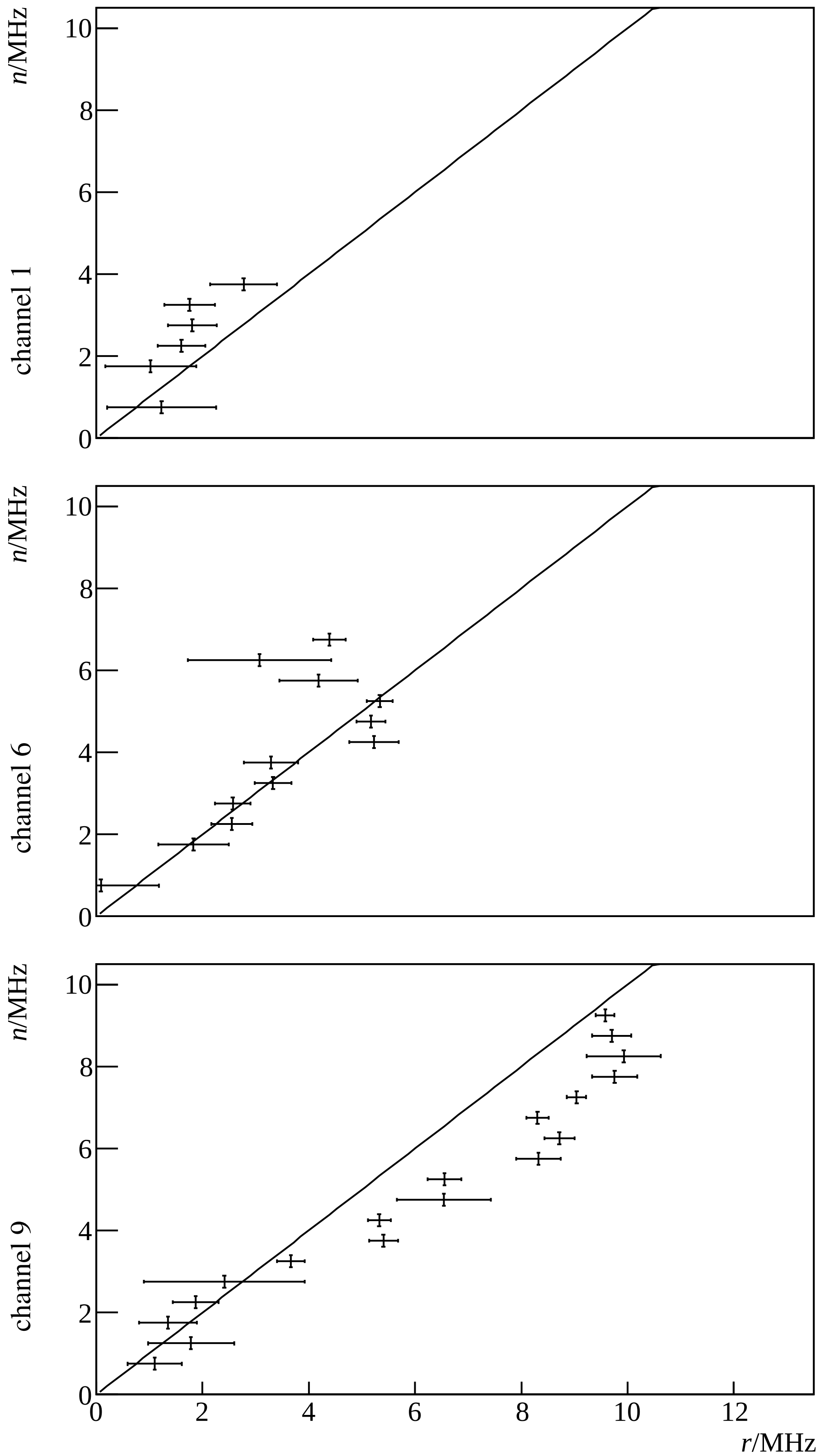

Figure 60. Scaler rate of channels 1, 6 and 9 vs. reconstructed rate from the TDC. The other channels can be found in Appendix C. Shown are the statistical errors. The line is defined by $n = r$.

7.2.6 Scaler versus Scaler

The third method is to approximate the real rate r_i by $c_i n_1$, the rate n_1 of the lowest channel (which is much smaller than the rates of the highest channels) times a normalisation factor c_i. Firstly, this is because of the $\mathrm{d}E_\gamma/E_\gamma$ run of the cross section and secondly, the width of the scintillator bars jumps from 11 mm to 17 mm in the middle of the detector. To assure that the decrease of the rate for one channel can be observed while the rate of the lowest is only slightly affected, only channels 7–9 will be used for this comparison with channel 1, since these are exposed to the highest rate. Figure 61 shows the scaler rate n_9 of channel 9 against the scaler rate n_1 of channel 1. There is no significant loss of rate for up to 4 MHz in channel 9. At the same time, this justifies the approximation, since for $n_9 = 4.0\,\mathrm{MHz}$, $n_1 \simeq r_1 = 1.3\,\mathrm{MHz}$ and no deviation from the linear behaviour has to be expected.

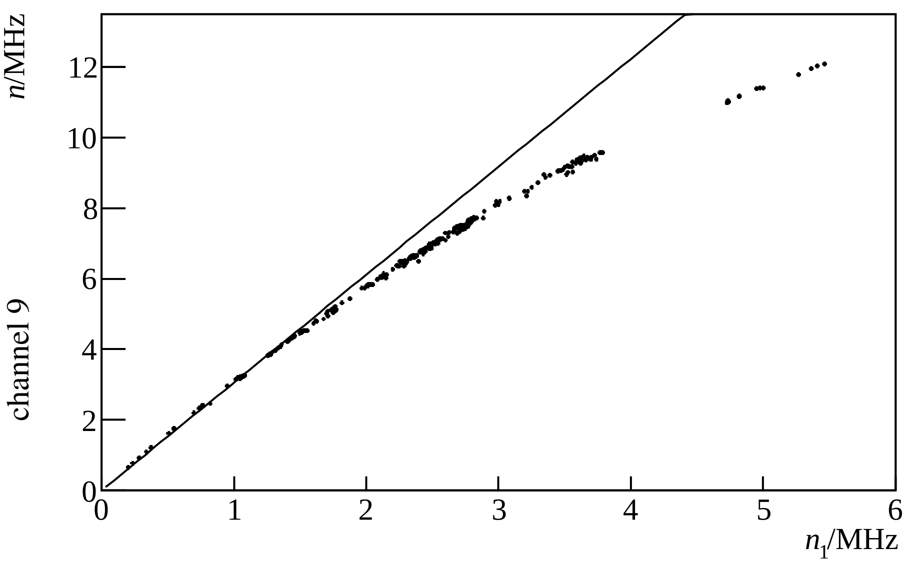

Figure 61. Scaler rate of channel 9 vs. scaler rate of channel 1. The other channels (8 and 9) can be found in Appendix C. The errors of the scaler rate are too small to be visible in this plot. The line is fitted for n up to 4 MHz. No data exist for the gap at $n_1 \simeq 4\,\mathrm{MHz}$.

7.2.7 Dead Times

In addition to the direct comparison of the real and the observed rates, the extraction of the dead time of the scintillator/photomultiplier tube combination is also tried. It is not possible because of the behaviour of the discriminators. When trying to fit Equation 59 or 60 to the observed rates, the resulting dead times lie at about 25 ns. This number is smaller than the dead time of the discriminator of 30 ns and thus cannot be correct. Probably, the discriminator itself induces this incorrect result. One possible origin could be pulses which are still over the threshold when the dead time ends, making the discriminator immediately send the next signal. The timing of this signal is incorrect and thus useless. Nevertheless, the dead time seems to be decreased, because also hits shortly before the end of the dead time are counted. This makes it impossible to extract the dead time of the detector itself without further tests. It is also not possible to use equation

61 to separate the dead time of the discriminator from the dead time of the photomultiplier tube. Without knowing the (effective) dead time of one of the components, the rates would have to be measured up to even higher rates. Only then, the influence of the combined dead time would differ significantly from the single dead times, allowing the calculation of both dead times with a fit of Equation 61 to the observed curve.

To summarize this section, it can be said that a rate of 4 MHz is possible for each channel without a significant loss. Scaling this number to the complete hodoscope leads to more than 50 MHz for the tagging rate. Even higher rates are possible when small losses are accepted. Therefore, the results fully conform to the requirements.

7.3 FPGA Coincidence Matching

Another important object of investigation is the test whether the FPGA recognizes all coincidences between two s-channels (channel corresponding to one PMT) correctly. This is crucial, since this information is part of the trigger condition in the experiment. Therefore, the coincidences are reconstructed from the individual TDC events and compared with the TDC events of the corresponding c-channels (here: channel corresponding to the coincidence of two neighbouring PMTs).

A priori it is not known which hit in one s-channel belongs to which hit in a neighbouring s-channel. Of course, hits belonging to a single electron should arrive within few ns, but the FPGA is not aware of this. So, each combination of two hits from two neighbouring s-channels s_i and s_j is counted as a possible coincidence s_{ij} here (grey lines in Figure 62). Assuming that the hit in s_i is prior to the hits in s_j, it does not suffice to take only the hit in s_j, which follows s_i first. This first could just as well be part of another coincidence s_{jk}, belonging to the neighbouring s-channel s_j and the s-channel s_k next to it (black line). To see if the FPGA generates the according coincidence signals and how long it takes to do so, the time span $\Delta t(c_{ij})$ from the second hit to the next hit in the corresponding c-channel c_{ij} is measured (figure 62 (b)).

The coincidence is implemented on the FPGA simply as the logical AND between two neighbouring s-channels. As the signal which is output by the discriminator has a width of

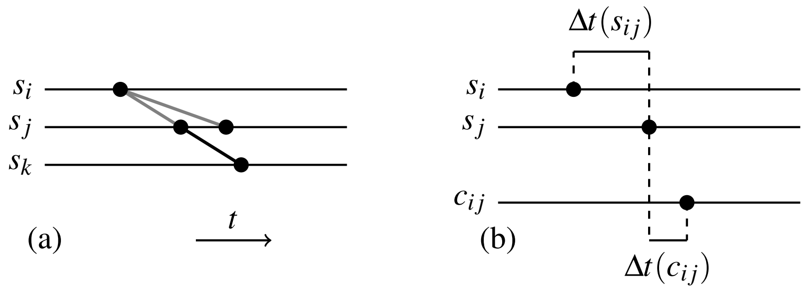

Figure 62. Counting of coincidences (a) and timing (b). The black dots represent hits on an s-channel s_i. (a) The two dots connected by the black line belong to the same electron, the other two dots belong to another electron. For details, see the text. (b) $\Delta t(s_{ij})$ is the time span between two hits on neighbouring s-channels. $\Delta t(c_{ij})$ is the time span from the second hit to the coincidence signal.

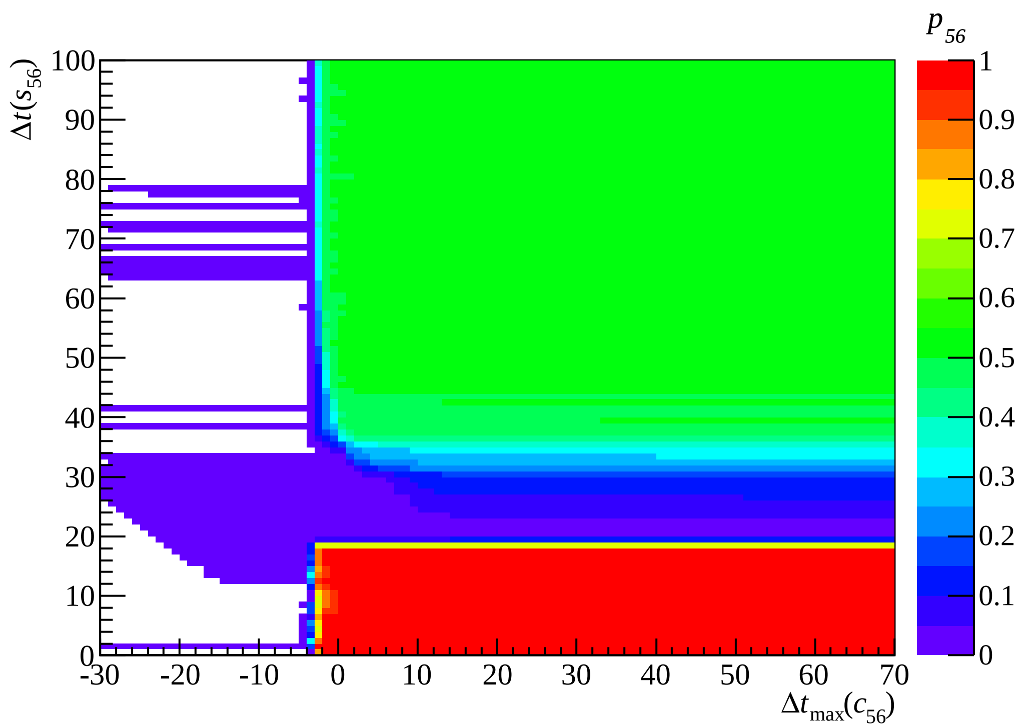

Figure 63. Probability that the FPGA recognizes a coincidence in dependence of the temporal distance (channels 5 and 6, the other channels can be found in appendix D). The red area indicates an accurate detection of coincidences. For the explanation of the different areas, see text.

about 20 ns, all hits with a smaller distance should be recognized as coincidence by the FPGA. Figure 63 shows the probability

$$p_{ij}\left(\Delta t(s_{ij}), \Delta t(c_{ij}) \leq \Delta t_{\max}(c_{ij})\right) \tag{62}$$

that hits separated by $\Delta t(s_{ij})$ (y-axis) are recognised as coincident between -30 ns and $\Delta t_{\max}(c_{ij})$ (x-axis) (see also Figure 62 (b)). For example, $p_{ij}(10\,\text{ns}, 20\,\text{ns}) = 1$, which means that it does not take more than 20 ns for the FPGA to send a coincidence signal for all hits with a distance of 10 ns. The reason why negative values for $\Delta t(c_{ij})$ are possible originates in different pulse recognition in the TDC and the FPGA. In principle, the coincidence signal from the FPGA should be delayed with respect to the single hits. But when the TDC uses the trailing edge of the pulse of the discriminator and the FPGA uses the leading edge, the timing information of the single hits is delayed by the signal length of the discriminator (20 ns). That way, the coincidence signal can be seen prior to the single hits.

The most interesting part of Figure 63 is the red filled area in the lower right. The value for p_{ij} is exactly one for $\Delta t(s_{ij}) \leq 15$ ns and $\Delta t_{\max}(c_{ij}) \geq 3$ ns, implying that all single hits with a distance of at most 15 ns are seen as coincident after at most 3 ns. Also on the other channels, coincidences are found with a probability of 100 %. For distances bigger than 15 ns, the probability decreases, probably due to a non constant signal length of the discriminator. This is also the reason why not all coincidences are seen within a constant time. Since the FPGA and the TDC do not use the same edge of the signal, there can be a jitter between their times due to the signal length.

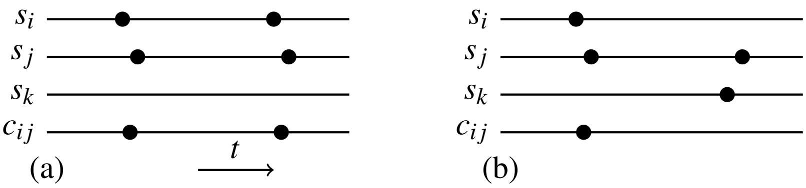

Figure 64. Different types of accidental coincidences. For a description, see the text.

The green area originates from incorrectly reconstructed coincidences. Assuming a real coincidence of channels s_i and s_j, a later hit on s_j will also be regarded as coincident with the hit on s_i. If the later hit originates from an electron out of the Bremsstrahlung target, there are two possibilities:

- s_i was hit a second time, too (Figure 64 (a)). Then there is a hit on c_{ij} at around this time.
- s_i was not hit. Instead the other neighbour s_k of s_j was hit (figure 64 (b)). There is no hit on c_{ij} at this time.

Since the overlap between two scintillator bars is more than 50 %, the probability for at least one of the neighbouring channels being hit, too, is bigger than 50 %. With the same probability, a hit on c_{ij} will be found at the time of the second hit on s_j. The gap between the red and the green area arises due to the dead time of the discriminator. It is washed out, as the distance between two hits of one coincidence is not constant. The purple area belongs to accidental coincidences of electrons or background radiation. The diagonal cut in the lower left can be observed due to timing constraints arising from the dead time and the signal length.

In summary, the generation of the coincidence signal was shown to work reliably. During 10^7 events, the FPGA did not lose a single coincidence event, as long as the time span between the single hits was short enough.

7.4 Comparison of Simulated and Measured Spectra

An interesting test is the comparison between simulated data and really measured data. To make this possible, the position of the detector prototype has been measured relative to the tagging magnet for both experimental tests. This piece of information was then used to generate simulated spectra as in Section 4.6. The general procedure of the comparison will be first explained for the test at the CB site and then extended for the second test.

7.4.1 Test at the CB Site

For the test at the CB site, the measurement of the position and the angle α between detector and magnet was not very precise. That is why the simulation was made for different angles. For one angle close to the measured angle, the agreement between simulation and measured data should be maximal. The simulated position was not changed for this test, since the impact of a small displacement is expected to be very small. The detector was mounted at a position corresponding to low electron energies, so that the rate is approximately constant over the dimension of the prototype. This implies that the spectrum looks the same if the detector is moved some cm.

To minimize the effects of background radiation, the spectrum of single hits is not used, but instead the actual double and triple coincidences are reconstructed as in Section 4.5.2. A quantitative measure for the agreement between simulation and experiment is then computed as follows:

(1) The mean rate for all channels is normalized to 1, for the real spectrum as well as for the simulated one (see Figure 65 (a), (b), (d)).

(2) The rate for each channel of the real spectrum is divided by the corresponding rate of the simulated spectrum (see Figure 65 (c), (e)).

(3) The standard deviation σ of all eight ratios describes the quality of simulated spectrum.

Ideally, the normalized simulated spectrum is equal to the normalized measured spectrum. Just in this case

$$\frac{N_{i,\,\mathrm{real}}}{N_{i,\,\mathrm{sim}}} = 1 \quad \forall i, \tag{63}$$

$$\Rightarrow \sigma = 0. \tag{64}$$

Each deviation of the simulated spectrum leads to $\sigma > 0$. This quantity is then calculated for α between $15.0°$ and $25.0°$ with steps of $0.1°$ and 40000 events for each step. Figure 66 shows the σ dependence of α for the range where σ is reasonably small. The smallest value for σ is encountered at an angle of $\alpha = 21.5°$:

$$\sigma_{\mathrm{min}} = \sigma(21.5°) = 0.046. \tag{65}$$

The Figures 65 (b) and (c) shows the simulated spectrum as well as the ratio for this particular angle.

7.4.2 Test at the BGO-OD Site

This time, the prototype was mounted very close to the primary electron beam leaving the tagging magnet. This implies a big change of the rate when moving the detector up or down. Hence, this time, the spectrum is simulated for different angles α and for different vertical displacements Δx of the prototype relative to the measured position. Due to this second dimension and the limited amount of time, the granularity as well as the number of simulated events had to be decreased for this task. α is varied between $-4.0°$ and $7.0°$ with steps of $0.5°$, Δx between $-7.0\,\mathrm{cm}$ and $7.0\,\mathrm{cm}$ with steps of $0.5\,\mathrm{cm}$. 4000 events are simulated per point. The resulting values for σ are shown in Figure 67. Because of the low statistics, no single minimum can be seen here. However, it seems probable that $\Delta x \simeq 0$ and $\alpha \simeq 2.0°$, which is realistic as the position could be measured with a higher accuracy than the incline.

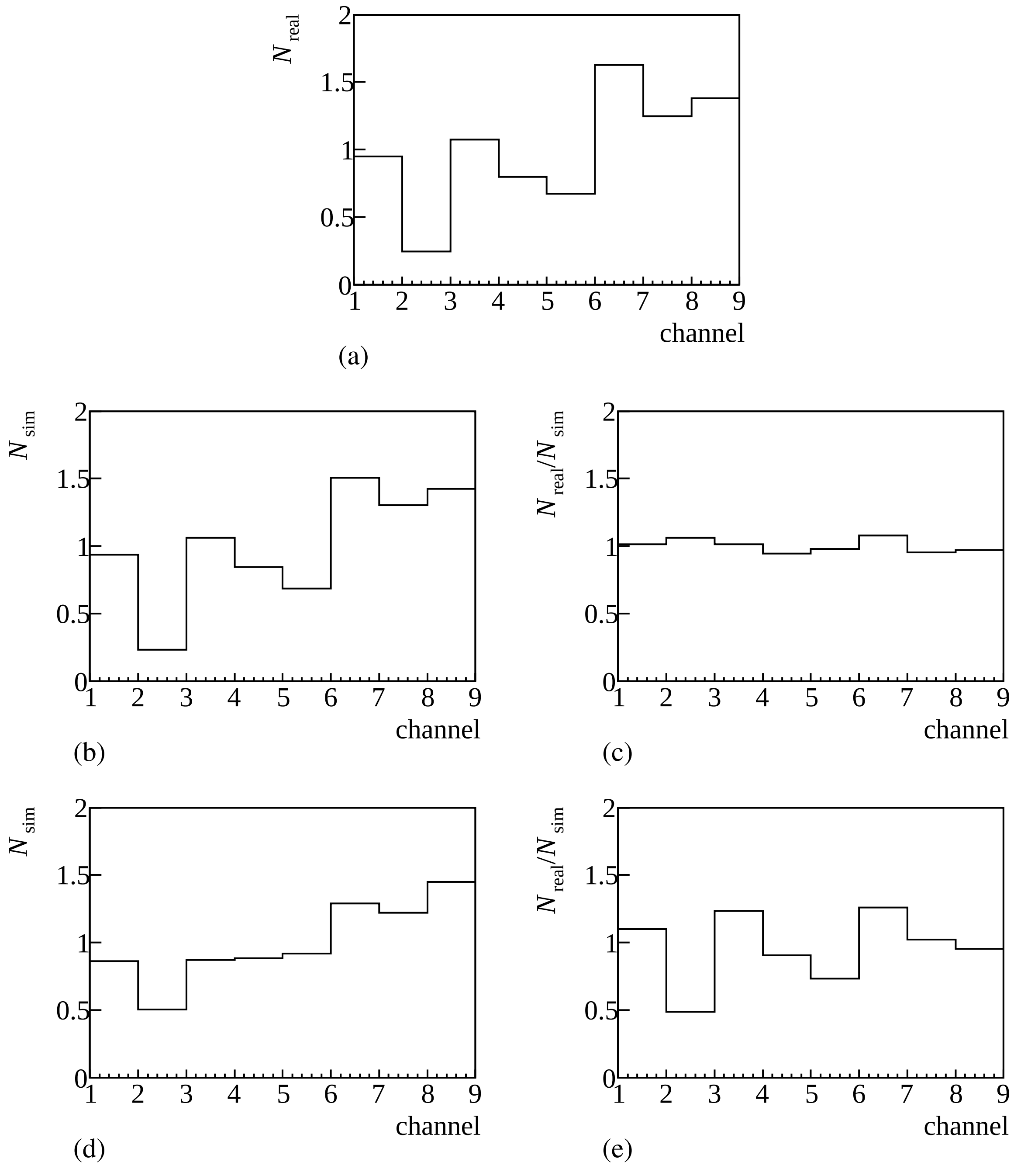

Figure 65. Measured spectrum (a). Simulated spectrum for 21.5° (b) and 24.0° (d). Ratio of real and measured spectrum for 21.5° (c) and 24.0° (e).

7.4.3 The Usefulness of this Comparison

The first test shows that there is a single position where the agreement between simulation and measurement is best. This point could not be found for the second test, which is probably due to the low statistics of the simulated data. When increasing the number of simulated events, the area of possible positions should be reduced.

This procedure can be used to measure the position of the detector with respect to the electron beam. With this piece of information, the detector can then be aligned precisely. After doing this, a complete energy calibration of the detector should be performed to ensure that the simulation reflects the actual reality. This can not be checked by only minimizing the disagreement of between the simulated and the measured data.

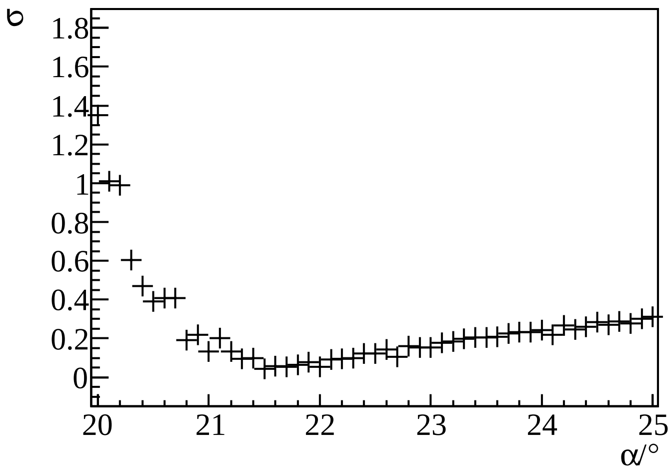

Figure 66. Deviation of the simulated data from the measured data (CB). σ measures the size of the deviation for different orientations of the simulated detector. For details, see the text.

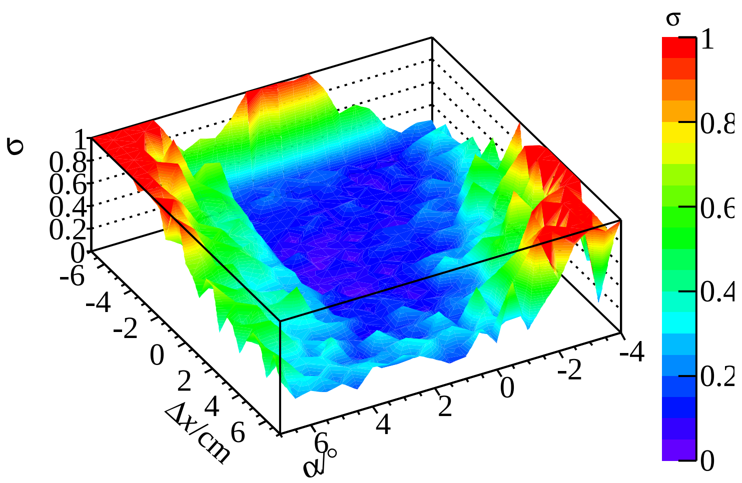

Figure 67. Deviation of the simulated data from the measured data (BGO-OD). σ measures the size of the deviation for different orientations of the simulated detector. For details, see the text.

8 Conclusion and Outlook

In the previous chapters, a complete design for a part of the vertical plane hodoscope has been described, starting from scratch by defining the requirements of the new tagging system right up to the in-beam test of a nine channel prototype detector. The results are now summarised briefly by chapter and compared to the requirements of Chapter 3. Finally, an outlook will be given on what is still to do to construct the complete tagging system.

Chapter 4: Detector Design

To define the best positions for the single scintillation counters, a simulation was set up which is able to compute the focal plane. A further program has been created to calculate the best arrangement of the scintillator bars in the focal plane as well as in the vertical plane, which is needed due to spatial limitations. After setting the magnetic field, the desired energy widths, the size of the photomultiplier tubes and some other tuning parameters, the complete layout can be generated without further input. This way, a design using three vertical planes with an energy width ΔE between $0.6\,\%E_0$ $(20\,\mathrm{MeV}$ for $E_0 = 3200\,\mathrm{MeV})$ for the high energetic photons and $1.5\,\%E_0$ $(50\,\mathrm{MeV})$ for the low energetic photons was generated.

Furthermore, a modified simulation setup was used to estimate the resolution of the hodoscope. In the focal plane, no influence of the beam flaw can be observed. Starting with the vertical plane, the resolution becomes worse than the theoretical minimum of $\sigma_E = \Delta E/\sqrt{12}$. The worst simulation without including the radiator is $\sigma_E \simeq 0.56\,\%E_0$ $(18\,\mathrm{MeV})$, using a $200\,\mu\mathrm{m}$ Cu radiator, the resolution becomes $\sigma_E \simeq 0.63\,\%E_0$ $(20\,\mathrm{MeV})$. The best resolution for both scenarios is $\sigma_E \simeq 0.19\,\%E_0$ $(6\,\mathrm{MeV})$.

Chapter 5: Final Design and Prototype Detector

After the desired positions of the scintillator bars have been calculated, the mechanical construction for a prototype detector using nine Hamamatsu R7400U PMTs was designed and built. The design is extendible for the complete segment of hodoscope which uses this PMT. A focus was laid on easy maintenance of the hodoscope, in terms of the replacement of single PMTs and scintillator bars. The experimental tests showed that it is in fact possible to replace single PMTs within several minutes. The replacement of the scintillator bars is possible without affecting the energy calibration of the complete setup.

Chapter 6: Experimental Tests

A first test at the Crystal Barrel experiment was performed to ensure the correct functioning of the test setup including the electronics. The second, dedicated test at the BGO-OD experiment was then used to collect various data. During the second test, the position of the prototype was changed as well as the electron current extracted from ELSA.

Chapter 7: Data Analysis

The data from the experimental tests could be used to examine several important properties of the tagging hodoscope:

(1) By including effects which arise due to the discriminator, it was shown that a detecting efficiency between $\varepsilon = 99.2\,\%$ and $\varepsilon = 100.0\,\%$ can be achieved. This coincides with the expectation of Section 2.5.3.

(2) An analysis of the electron rates in single scintillator bars showed that rates of up $n = 4\,\mathrm{MHz}$ are possible for a single channel without significant losses. Assuming a coverage of 10 %–90 % of E_0, this implies a total rate of more than $n_{\mathrm{total}} = 50\,\mathrm{MHz}$ for the complete hodoscope, entirely fulfilling the requirements.

(3) The later experiment will use the coincidence of two s-channels as the trigger condition of the tagging system. Therefore, the FPGA which generates the coincidence signal for the trigger was tested. Each single coincidence was recognised during the experimental test.

(4) To check the correct work of the simulation program, simulated c-channel spectra were compared to the measured spectra. The Crystal Barrel test showed that the simulation can be used to align the detector precisely, at least for the high photon energy range. The comparison for the BGO-OD experiments has to be repeated with better statistics to confirm this.

8.1 Outlook

Further tests can be made using the already existing prototype:

(1) An energy calibration would show if the simulation predicts the electron trajectories correctly. During this calibration, E_0 is varied in a large range and the current in the tagging magnet is swept to redirect the primary beam without radiator directly into the hodoscope. During this test, the beam intensity is strongly decreased (see also [FP09a]).

(2) The influence of an additional shielding against the magnetic field of the tagging magnet can be investigated. The design of the prototype provides enough room to wrap two layers of Mumetal foil around the PMTs.

(3) The precise timing of the prototype was not tested. This depends on the scintillator material but for the prototype, only old scintillator material could be used. By further testing with the new scintillator (see Section 3.6), the timing resolution of the final detector can be investigated.

To finish the complete tagging system, some building blocks are still missing:

(1) The mechanical layout for the lower part of the vertical plane and for the focal plane has to be designed. Probably, the existing design can be adapted to the larger photomultiplier tubes to be used for the lower part of the vertical plane. Instead of fixing the black foil with adhesive tape, a frame construction should be used which is screwed onto the detector. As in the focal plane the spatial distance between the channels is bigger, the construction of this part of the hodoscope should be more simple than the other parts.

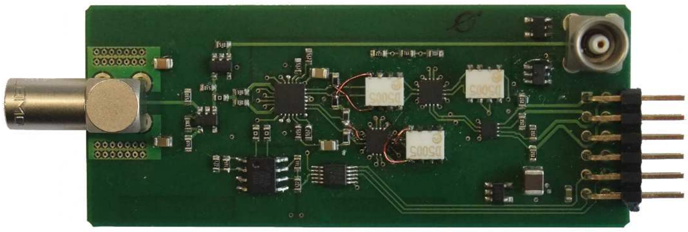

Figure 68. FrED board prototype. The PMT signal enters on the left connector. An amplified analogue signal as well as the digital signal is output on the right.

(2) Only a basic functional check was made for the PMTs which will be used for the lower part of the vertical plane as well as for the focal plane. Before building the remaining parts of the detector, their behaviour at high rates and their efficiency should be investigated.

(3) The electronics which was used for the experimental test is not final. Rather, a new electronic design is under way in [Mes10]. At the moment, there are tests of the FrED[44] board which amplifies and discriminates the analogue signal (see Figure 68). The future plan is to amplify and split actively the analogue output of the PMT with the AFA[45] board as close as possible to the hodoscope. The active splitting prevents crosstalk between the two outputs. Multiple channels are collected on the B-FrED board. This board will take care of the discrimination and the connection to the slow control. Using the new electronics, further tests can be made, providing information about the precise timing of the signals.

(4) To increase the resolution for low photon energies, one could possibly use an additional detector using scintillating fibres with a small diameter of a few mm. Such a device is employed in the tagging system of the Crystal Barrel experiment [FP09a]. However, the minimum resolution depends on the shape of the electron beam, see Section 4.6. For the 200 µm Cu radiator the worst resolution is $\sigma_E = 20\,\mathrm{MeV}$ for $E_0 = 3200\,\mathrm{MeV}$. The minimum resolution given by the width of the scintillator bars is just $\sigma_{\mathrm{min}} = 14\,\mathrm{MeV}$. Thus, less than $\sigma = 6\,\mathrm{MeV}$, corresponding to an energy width $\Delta E = 17\,\mathrm{MeV}$, cannot be achieved.

8.2 Conclusion

A very promising design for the tagging hodoscope has been developed and tested during this thesis, incorporating the demands of Chapter 3. All tests and analyses which were performed conform to the expectations. By translating the mechanical design to the complete detector, a tagging system is obtained which fulfils the experimental needs completely and which, in addition, is easy to maintain.

[44] Front End Discriminator
[45] Analog Fanout and Amplifier

References

[AAA+03] AGOSTINELLI, S. ET AL. GEANT4–a simulation toolkit. *Nuclear Instruments and Methods in Physics Research Section A: Accelerators, Spectrometers, Detectors and Associated Equipment*, 506(3):250–303, 2003.

[BAA+97] BOCQUET, J. P. ET AL. GRAAL: a polarized γ-ray beam at ESRF. *Nuclear Physics A*, 622(1–2):c124–c129, 1997.

[Bal10] BALLING, A. *In preparation*. Ph.D. thesis, Universität Bonn, 2010.

[BCD+90] BABUSCI, D. ET AL. Polarized gamma-ray beams by inverse compton scattering. *Progress in Particle and Nuclear Physics*, 24:119–139, 1990.

[Bel10] BELLA, A. *In preparation*. Diploma thesis, Universität Bonn, 2010.

[BLP71] BERESTETSKIĬ, V. ET AL. *Relativistic Quantum Theory*. Pergamon Press, Oxford, 1971.

[BR97] BRUN, R. AND RADEMAKERS, F. ROOT – An object oriented data analysis framework. *Nuclear Instruments and Methods in Physics Research Section A: Accelerators, Spectrometers, Detectors and Associated Equipment*, 389(1–2):81–86, 1997.

[Bru10] BRUDVIK, J. The Near-Threshold Pion Photoproduction Program at MAX-lab. In *Svenskt Kärnfysikermöte XXIX*. Örebro, Sweden, 2010.

[Bur96] BURGWINKEL, R. *Aufbau und Test und Eichung des hochauflösenden Tagging-Systems TOPAS II am Bonner SAPHIR-Detektor*. Ph.D. thesis, Universität Bonn, 1996.

[CAE06] CAEN S.p.A. *User's Manual: Mod. V1190-VX1190 A/B, 128/64 Ch Multihit TDC*, 7th edition, 2006.

[CER93] CERN, Geneva. *GEANT–Detector description and simulation tool*, 1993. CERN Program Library Long Write-up W5013.

[che10] Chemical Search Engine, Nov. 2010.
URL `http://www.chemindustry.com/apps/chemicals`

[Chr04] CHRISTIANSEN, J. *High Performance Time to Digital Converter*. CERN/EP - MIC, 9 2004. Version 2.2 for HPTDC 1.3.

[CMA+09] CREDE, V. ET AL. Photoproduction of η and η' mesons off protons. *Phys. Rev. C*, 80(5):055202, Nov 2009.

[CRE96] CREATIVE ELECTRONIC SYSTEMS S.A. *CBD 8210 CAMAC Branch Driver User's Manual*, 2nd edition, 1996.

[DBB+00] D'ANGELO, A. ET AL. Generation of Compton backscattering γ-ray beams. *Nuclear Instruments and Methods in Physics Research Section A: Accelerators, Spectrometers, Detectors and Associated Equipment*, 455(1):1–6, 2000.

[EBB+09] ELSNER, D. ET AL. Linearly polarised photon beams at ELSA and measurement of the beam asymmetry in π^0 photoproduction off the proton. *The European Physical Journal A - Hadrons and Nuclei*, 39:373–381, 2009.

[Els07] ELSNER, D. *Untersuchung kleiner Partialwellenbeiträge in der Nähe dominierender Resonanzzustände des Protons mit linear polarisierten Photonen*. Ph.D. thesis, Universität Bonn, 2007.

[els10a] Electron Strechter Accelerator (ELSA), Nov. 2010. URL `http://www-elsa.physik.uni-bonn.de/Beschleuniger/bilder/elsaplan_en.pdf`

[Els10b] ELSNER, D. Private communication, 2010.

[ET 09] ET Enterprises Ltd. *9111B series data sheet*, 2009.

[Ewa10] EWALD, R. *Untersuchung der $\Sigma^+K_s^0$ Photoproduktion am Proton mit dem CBELSA/TAPS-Experiment*. Ph.D. thesis, Universität Bonn, 2010.

[FP09a] FORNET-PONSE, K. *Die Photonenmarkierungsanlage für das Crystal-Barrel/TAPS-Experiment an ELSA*. Ph.D. thesis, Universität Bonn, Bonn, 2009.

[FP09b] FORNET-PONSE, K. Private communication, 2009.

[Fro10] FROMMBERGER, F. Private communication, 2010.

[Gen99] GENTNER, M. *Präparation von Teilchenstrahlen für Experimente der Hadronenphysik: langsame Extraktion an ELFE@DESY und ELSA, sowie Strahlkühlung an HERA*. Ph.D. thesis, Universität Bonn, 1999.

[Gre00] GREEN, D. *The Physics of Particle Detectors*. Cambridge University Press, New York, 2000.

[HAB+03] HŘIVNÁČOVÁ, I. ET AL. The Virtual Monte Carlo. In *Computing in High Energy and Nuclear Physics*. La Jolla, California, 2003.

[Ham04] Hamamatsu Photonics K.K. *R7400U series*, 2004.

[Ham07] Hamamatsu Photonics K.K. *Photomultiplier Tubes – Basics and Application*, 3rd edition, 2007.

[Ham10] HAMMAN, D. *In preparation*. Ph.D. thesis, Universität Bonn, 2010.

[Han10] HANNAPEL, J. Private communication, 2010.

[Hil06] HILLERT, W. The Bonn Electron Stretcher Accelerator ELSA: Past and future. *The European Physical Journal A - Hadrons and Nuclei*, 28:139–148, 2006.

[Jac06] JACKSON, J. D. *Klassische Elektrodynamik*. Walter de Gruyter, Berlin, 4th edition, 2006.

[Kam10] KAMMER, S. *Strahlpolarimetrie am CBELSA/TAPS Experiment*. Ph.D. thesis, Universität Bonn, 2010.

[Kle05] KLEINKNECHT, K. *Detektoren für Teilchenstrahlung*. B. G. Teubner, Wiesbaden, 4th edition, 2005.

[KM59] KOCH, H. AND MOTZ, J. Bremsstrahlung Cross-Section Formulas and Related Data. *Reviews of Modern Physics*, 31(4):920–955, 1959.

[LD91] LYNCH, G. R. AND DAHL, O. I. Approximations to multiple Coulomb scattering. *Nuclear Instruments and Methods in Physics Research Section B: Beam Interactions with Materials and Atoms*, 58(1):6–10, 1991.

[Leb02] LEBERIG, M. D. *Das COMPASS-Triggersystem zur Messung des Gluonbeitrags ΔG zum Protonspin*. Ph.D. thesis, Universität Mainz, 2002.

[LeC74] LeCROY research systems corporation. *CAMAC Model 2249A Technical Data*, 1974.

[Leo94] LEO, W. R. *Techniques for Nuclear and Particle Physics Experiments*. Springer-Verlag, Heidelberg, 1994.

[lep10] LEPS Beamline, Sept. 2010.
URL `http://www.rcnp.osaka-u.ac.jp/Divisions/np1-b/lepsbl.html`

[Mes10] MESSI, F. *In preparation*. Ph.D. thesis, Universität Bonn, 2010.

[MKA+08] MCGEORGE, J. ET AL. Upgrade of the Glasgow photon tagging spectrometer for Mainz MAMI-C. *The European Physical Journal A - Hadrons and Nuclei*, 37:129–137, 2008.

[Mü73] MÜLLER, J. W. Dead-time problems. *Nuclear Instruments & Methods*, 112(1–2):47–57, 1973.

[O'R10] O'RIELLY, V. The Near Threshold Pion Production Program at MAX-lab. In *American Physical Society Division of Nuclear Physics Spring Meeting*. Washington DC, USA, 2010.

[Pus10] PUSCH, T. *In preparation*. Ph.D. thesis, Universität Bonn, 2010.

[SAA10] SCHMIDT, C. ET AL. The explora analysis software, in preparation. CB-Note, 2010.

[Sai05] Saint-Gobain Ceramics & Plastics, Inc. *BC-400,BC-404,BC-408,BC-412,BC-416 Premium Plastic Scintillators*, 2005.

[SBB+94] SCHWILLE, W. ET AL. Design and construction of the SAPHIR detector. *Nuclear Instruments and Methods in Physics Research Section A: Accelerators, Spectrometers, Detectors and Associated Equipment*, 344(3):470–486, 1994.

[Sch09] SCHEDLER, M. *Optimierung von Hochfrequenz-Intensitätsmonitoren am Elektronenbeschleuniger ELSA*. Bachelor thesis, Universität Bonn, 2009.

[Sie76] SIEBKE, W. *Die Homöotypie bei den Hepatahydratsulfaten: Mössbauereffektuntersuchungen an den Mischkristallsystemen: (Fe, Me) $SO_4 7H_2O$, Me=Mg, Ni, Zn, Co*. Ph.D. thesis, Universität Erlangen-Nürnberg, Erlangen, 1976.

[Tim69] TIMM, U. Coherent Bremsstrahlung of Electrons in Crystals. *Fortschritte der Physik*, 17(12):765–808, 969.

[Wal10] WALTHER, D. CAD drawings, 2010.

9 Danksagung

An dieser Stelle möchte ich mich bei all denen bedanken, die mich bei der Anfertigung dieser Diplomarbeit unterstützt haben.

Für die Vergabe des interessanten und herausfordernden Themas sowie die Unterstützung während der Arbeit bedanke ich mich bei Herrn Prof. Dr. Schmieden. Besonderer Dank gebührt Herrn Dr. Elsner für seine Betreuung während des letzten Jahres sowie für seine gewissenhafte Korrektur der Diplomarbeit. Danken möchte ich Dieter Walther für seine Hilfe bei der Erstellung der technischen Zeichnungen sowie der feinmechanischen Werkstatt des HISKP für die Realisierung der mechanischen Bauteile. Außerdem möchte ich mich bei Dr. Russell Johnstone, Dr. Claire Chapin, meinen Eltern und meiner Freundin Gesine für das Korrekturlesen bedanken. Zu guter Letzt bedanke ich mich bei der ganzen Arbeitsgruppe für das gute Arbeitsklima sowie für die hilfreichen Diskussionen.

Appendix

A Technical Drawings

Prototype Detector

Technical drawings of all parts of prototype detector. Left and right are as seen when looking from the front while the detector is mounted at the BGO-OD experiment. All distances are quoted in mm. See Section 5 for a description.

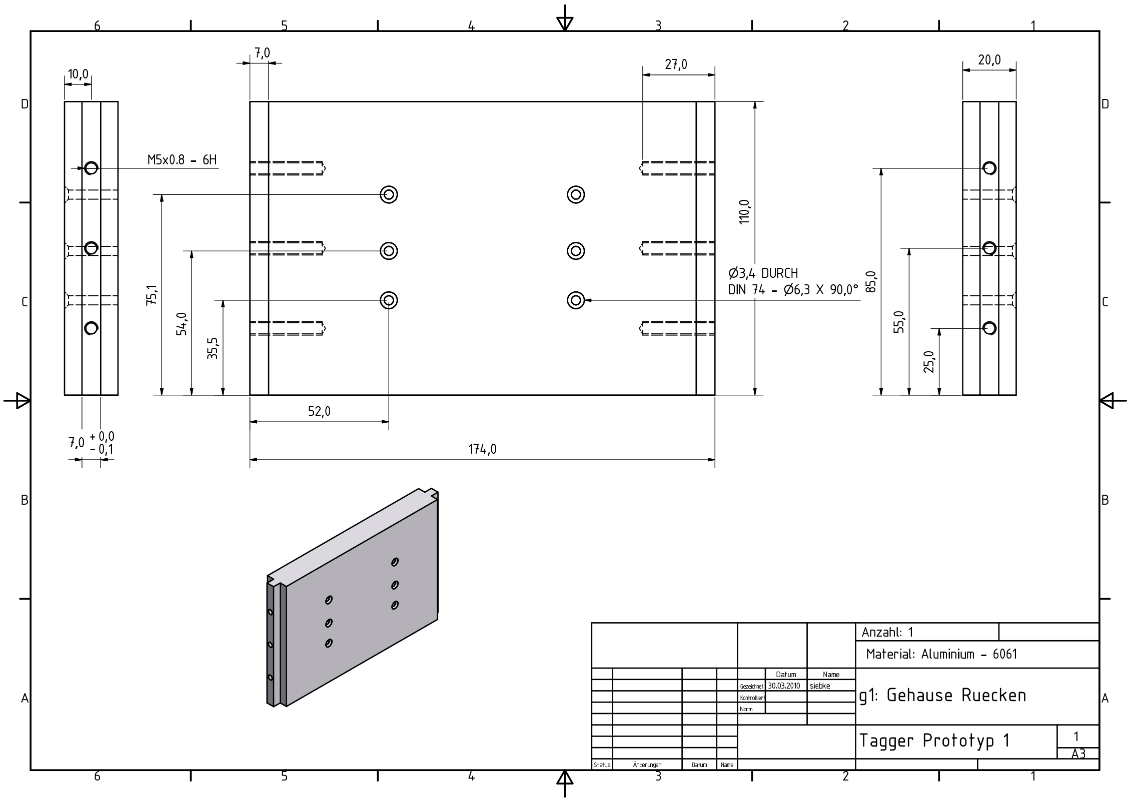

Figure 69. Back plane of the chassis.

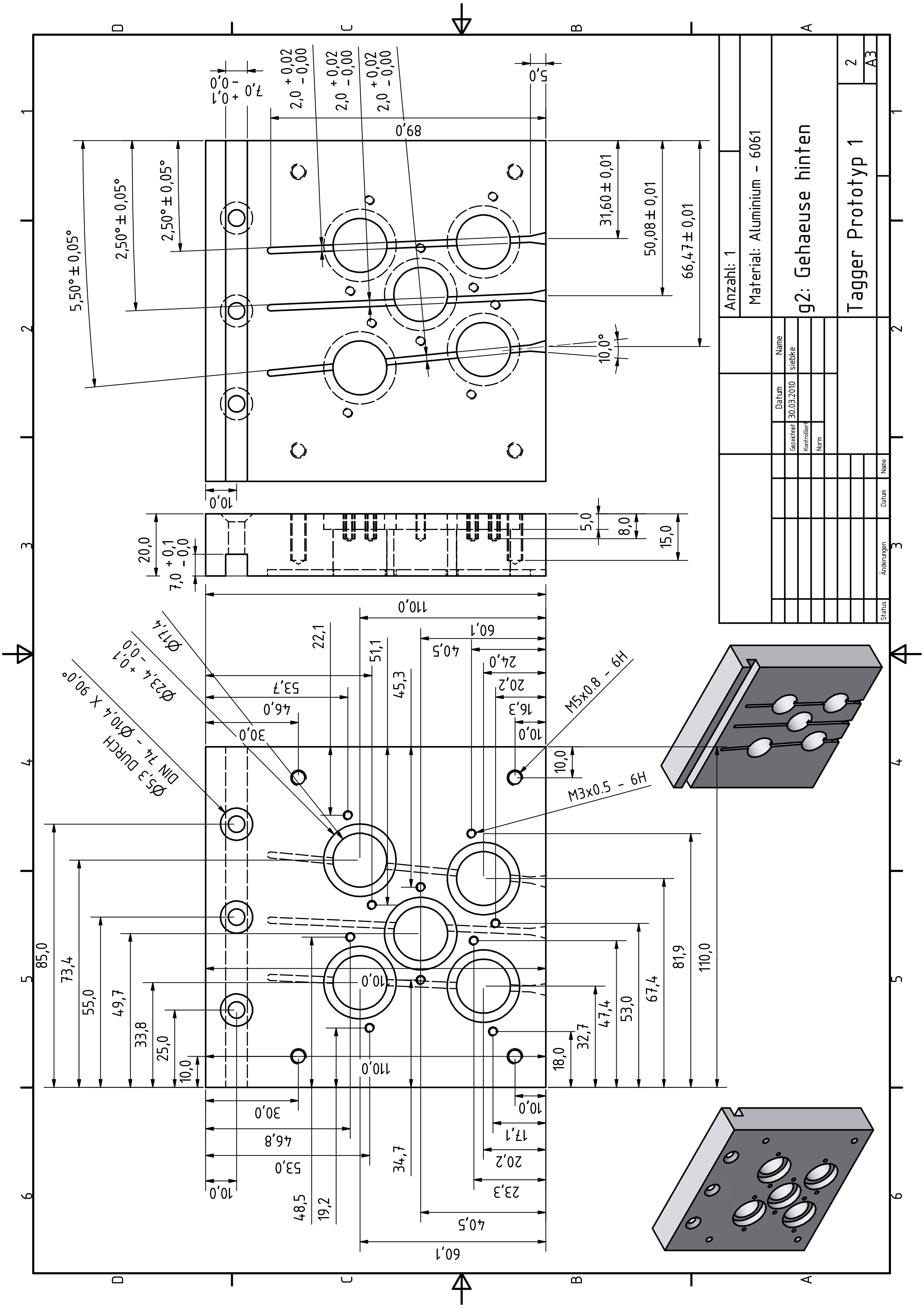

Figure 70. Left side plane of the chassis.

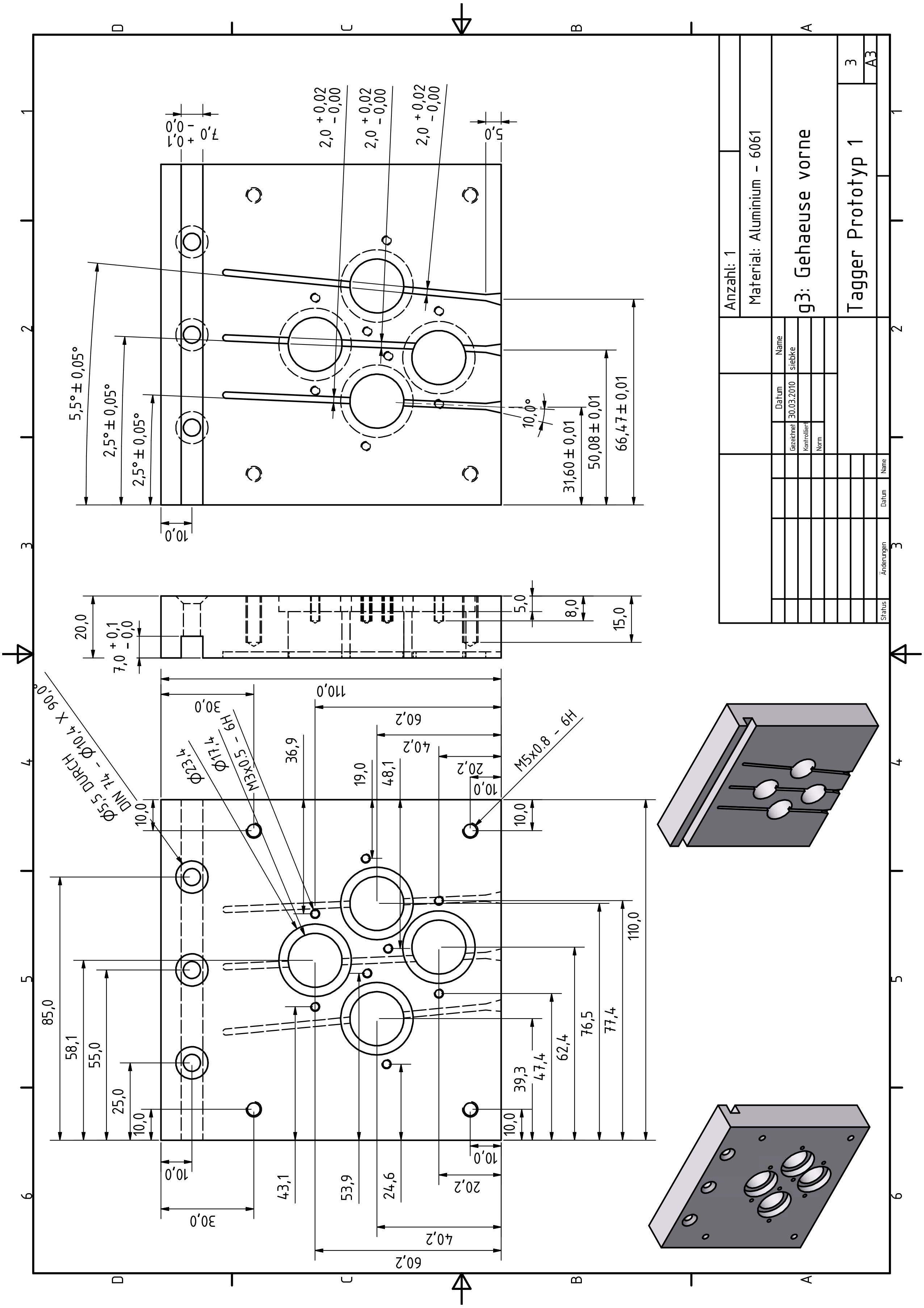

Figure 71. Right side plane of the chassis.

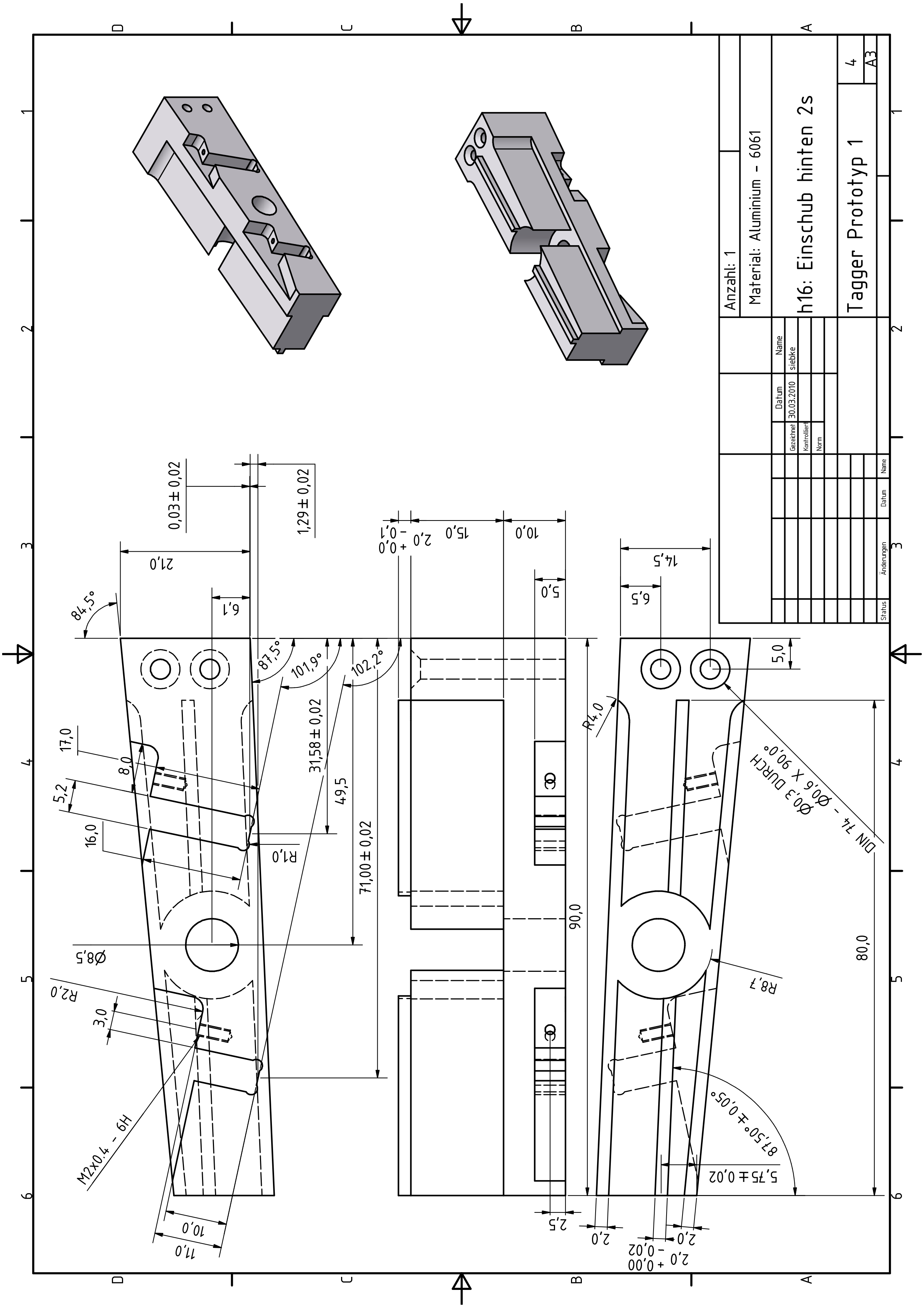

Figure 72. Left side of the middle slide.

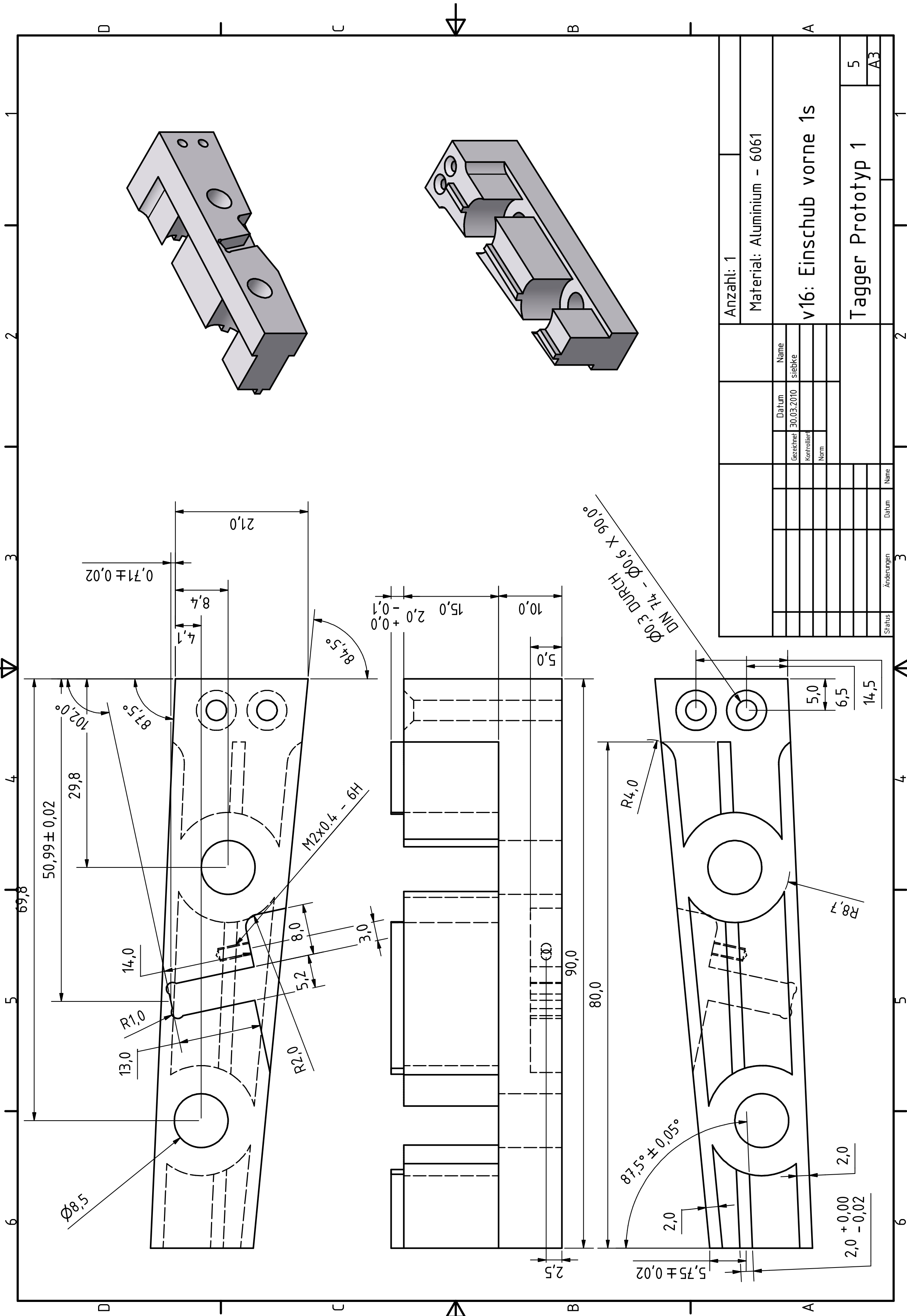

Figure 73. Right side of the middle slide.

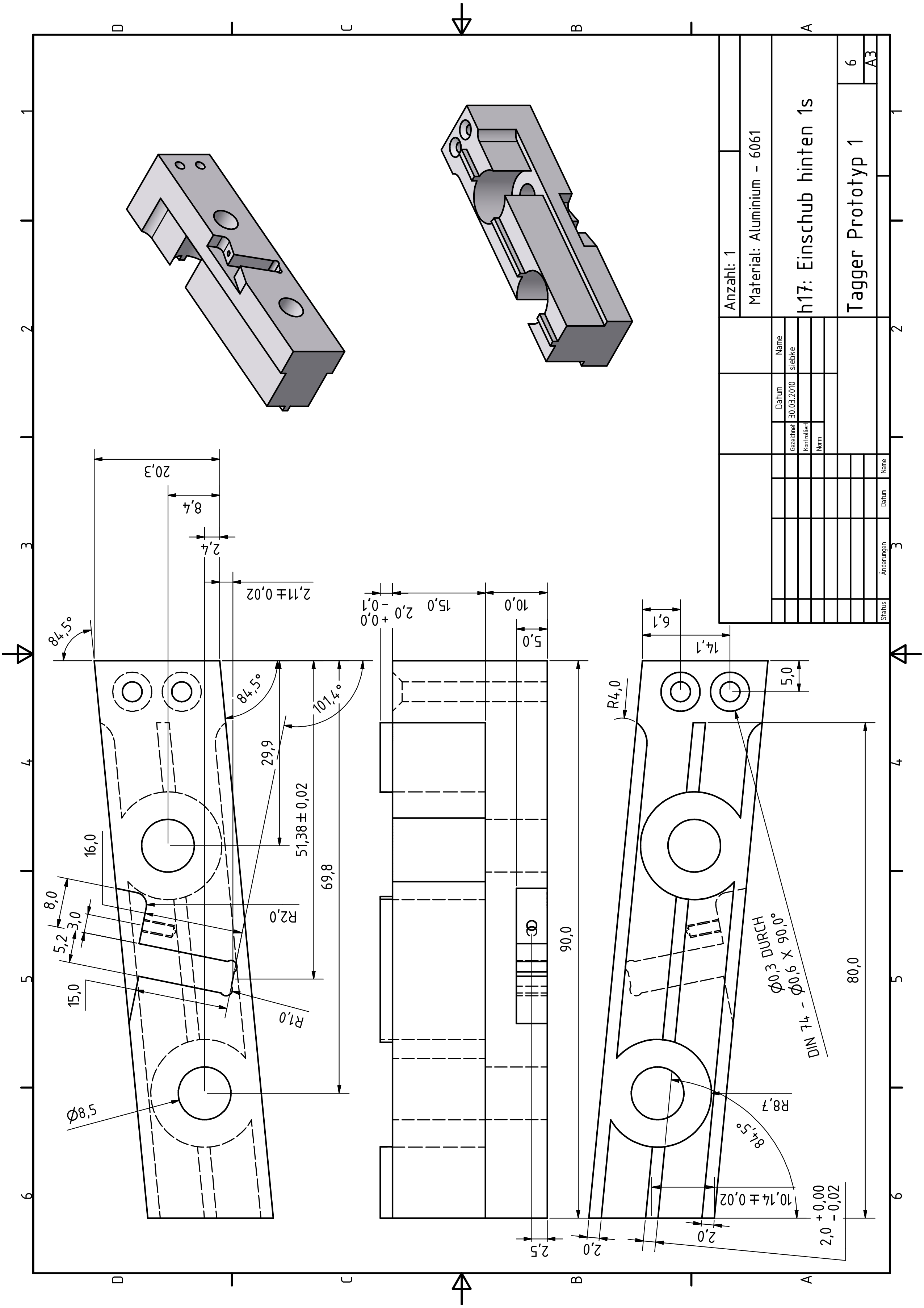

Figure 74. Left side of the top slide.

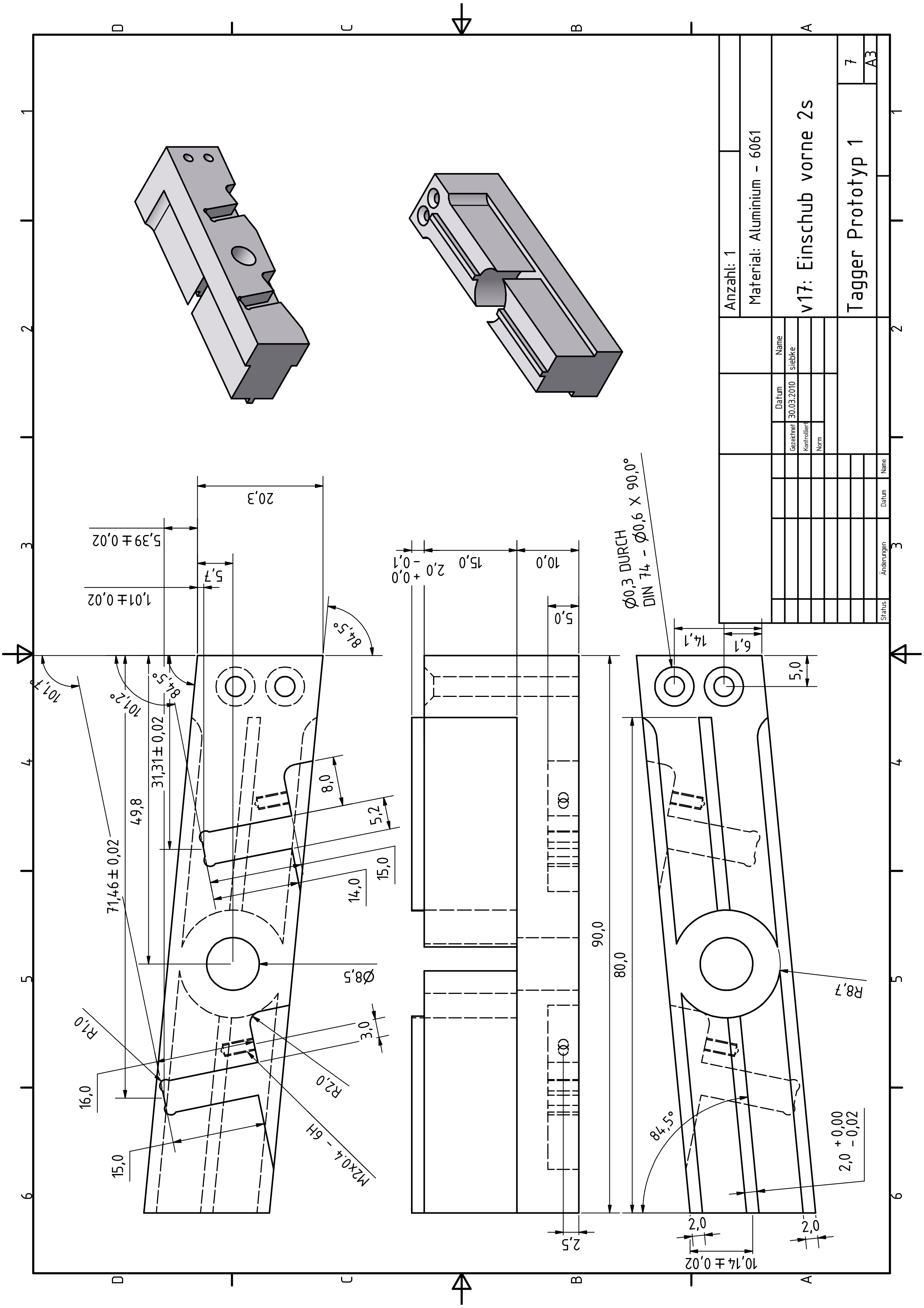

Figure 75. Right side of the top slide.

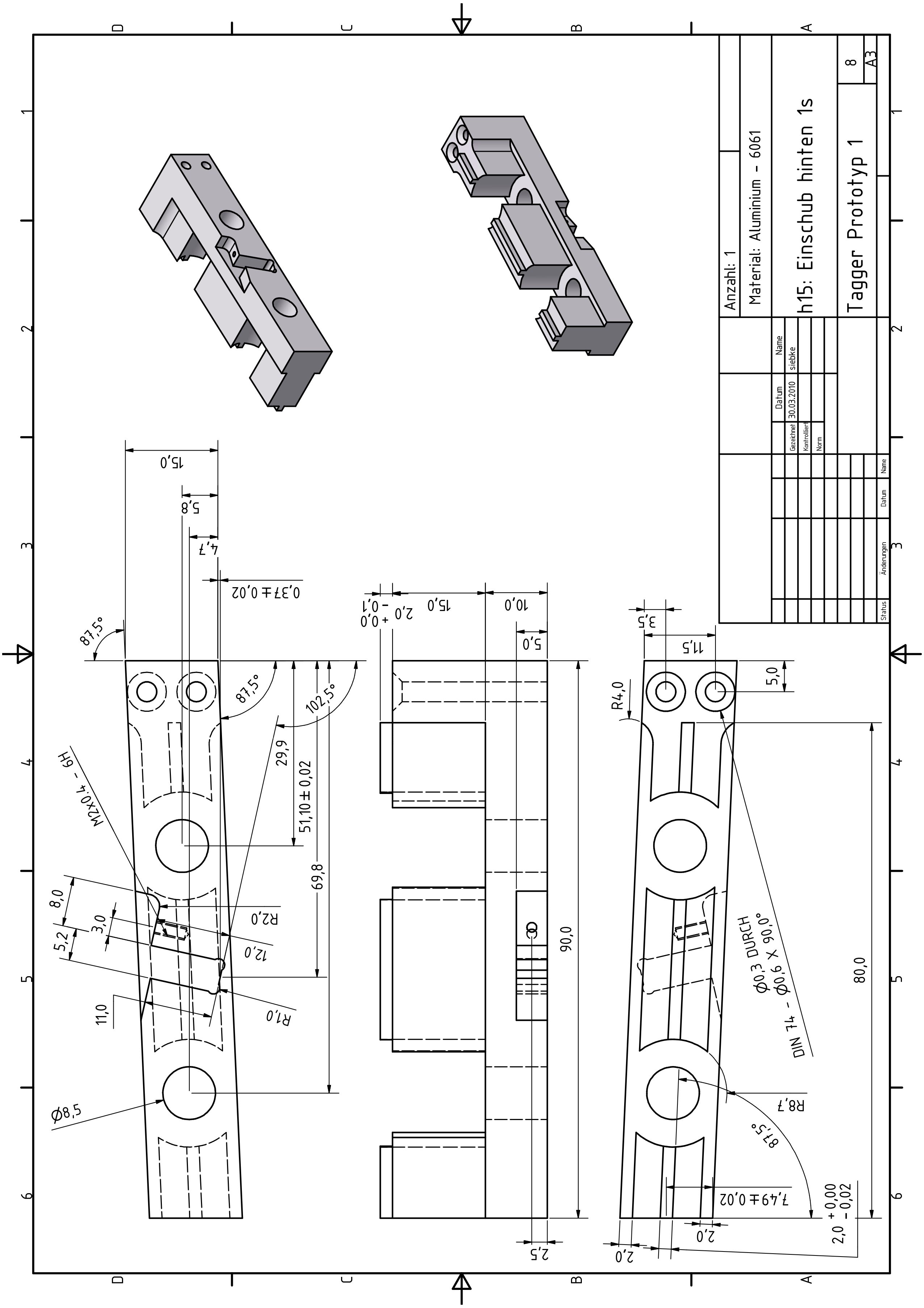

Figure 76. Left side of the bottom slide.

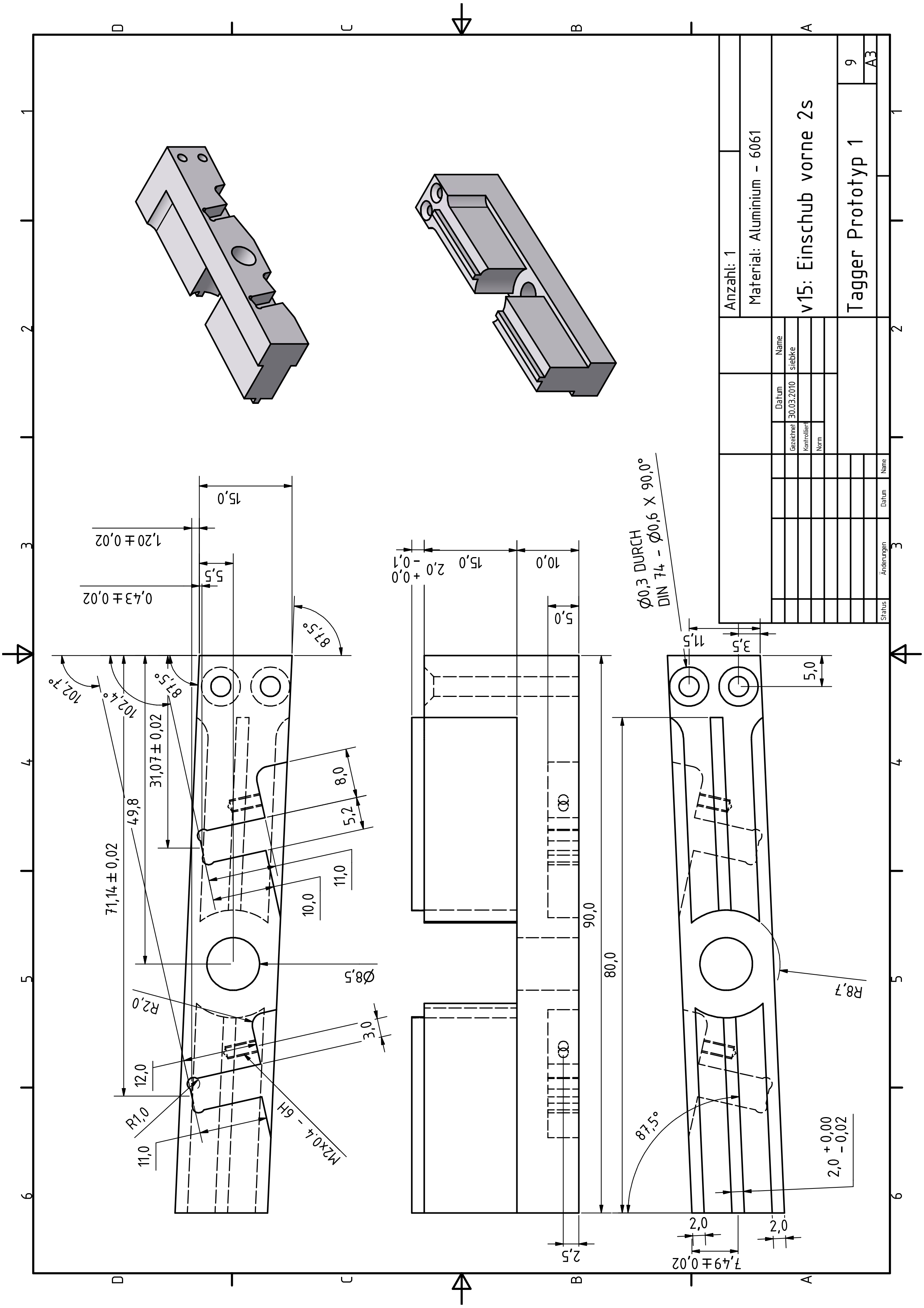

Figure 77. Right side of the bottom slide.

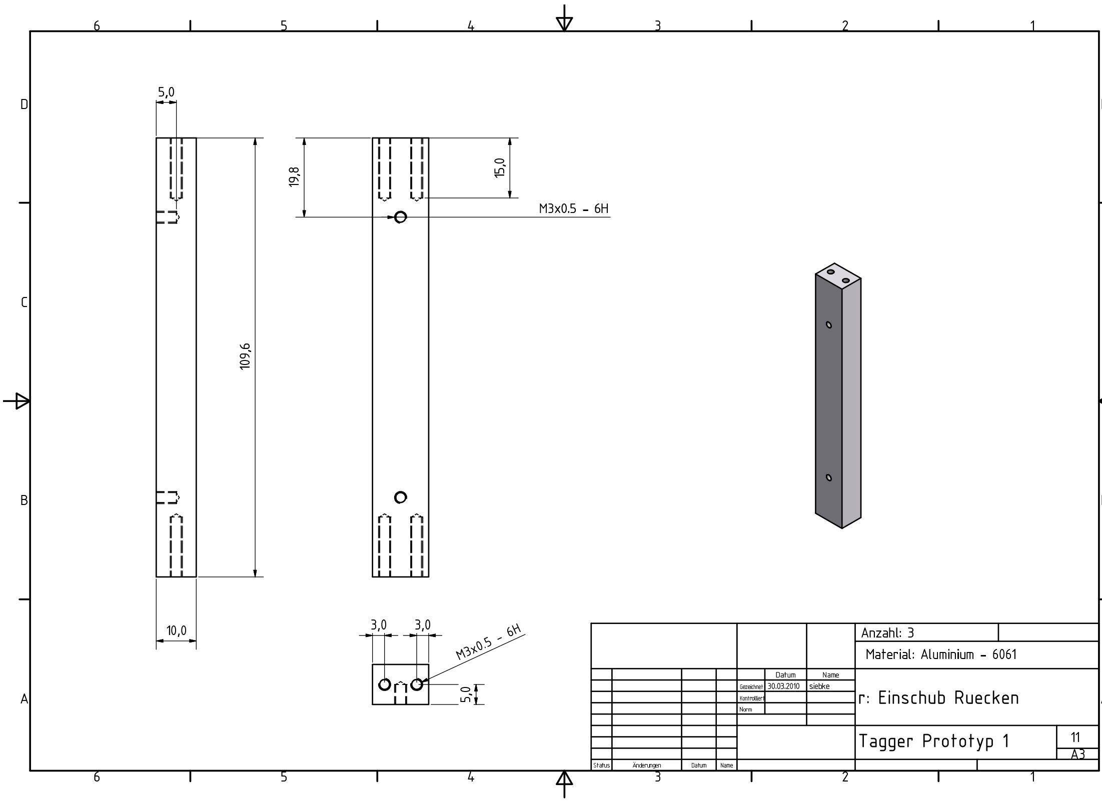

Figure 78. Back side of the slides.

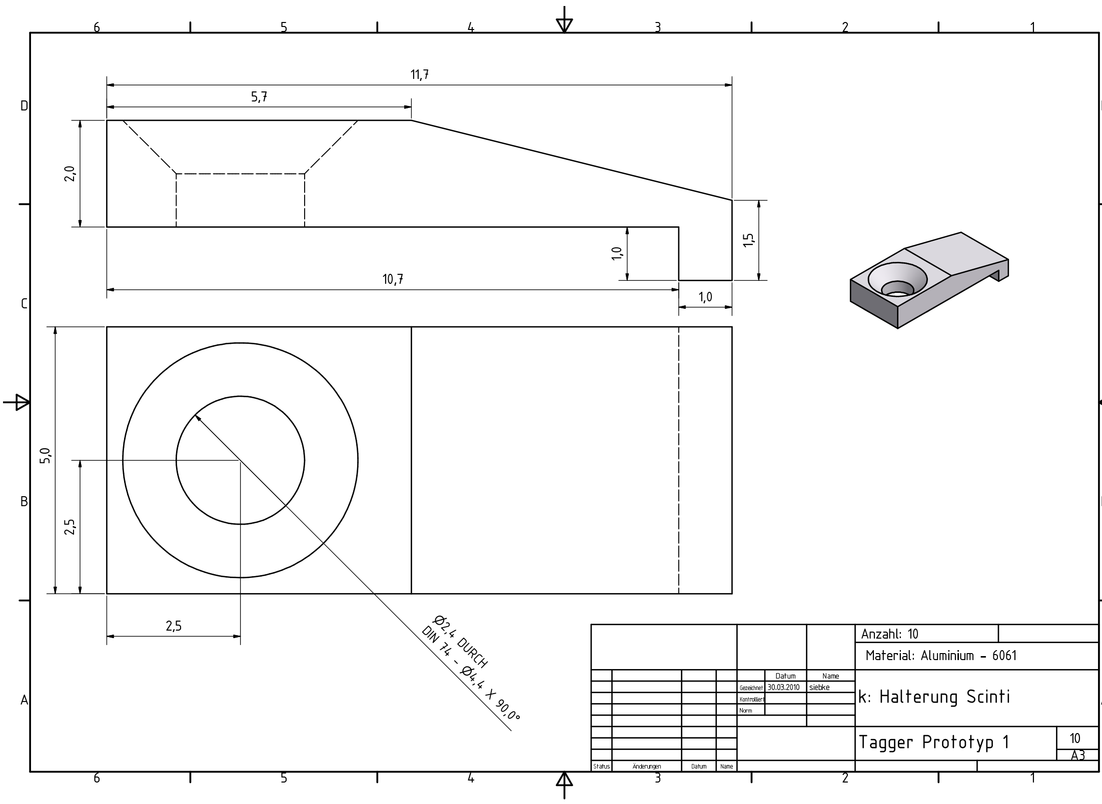

Figure 79. Clip used to fix the scintillator bars.

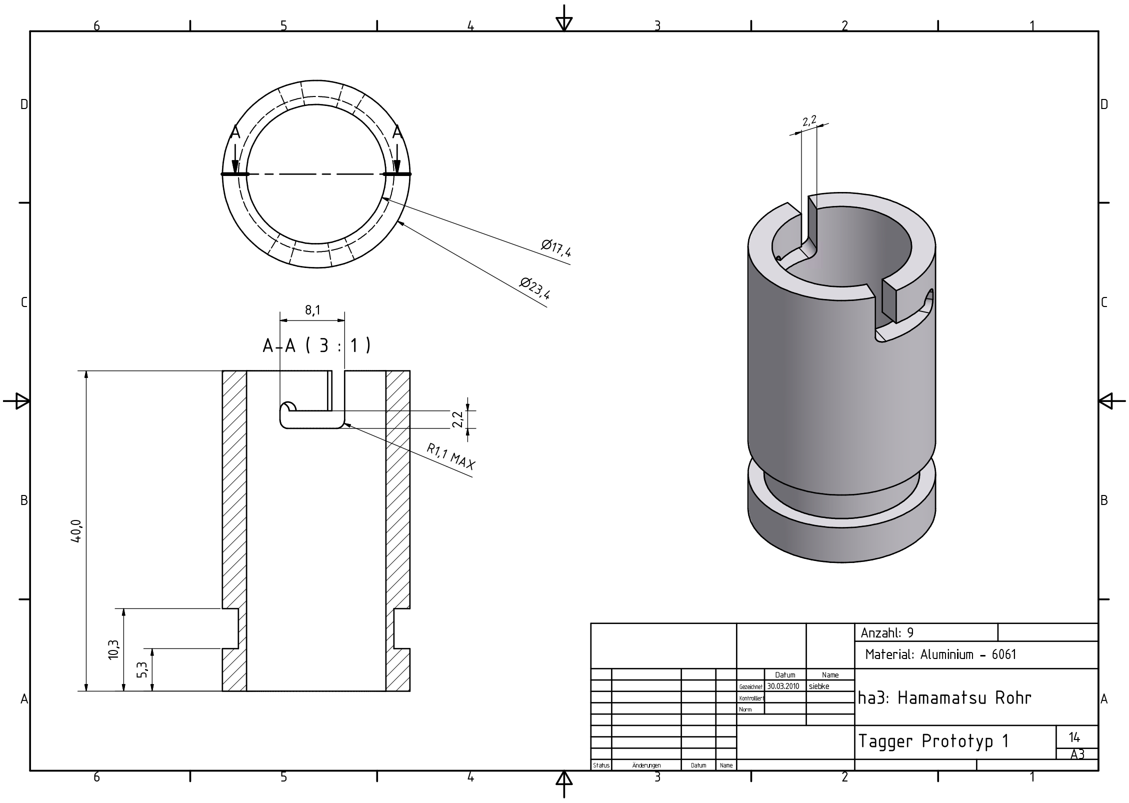

Figure 80. Cylinder of the PMT assembly.

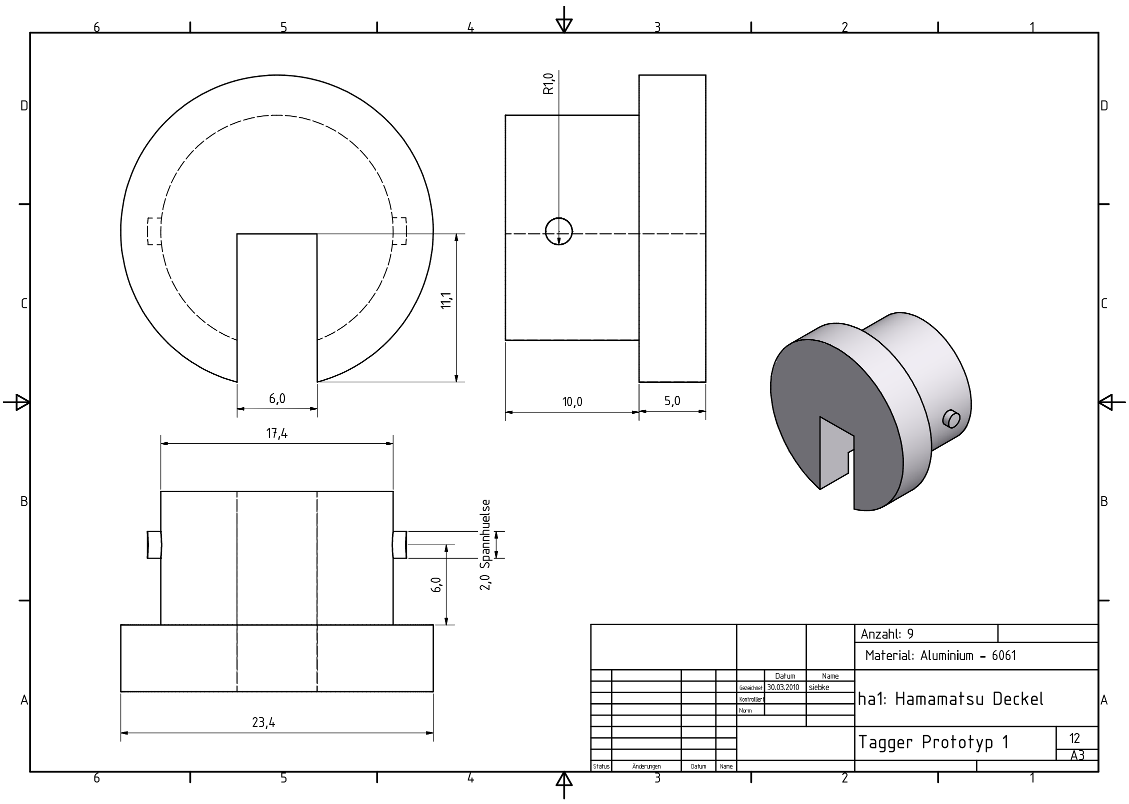

Figure 81. Cap of the PMT assembly.

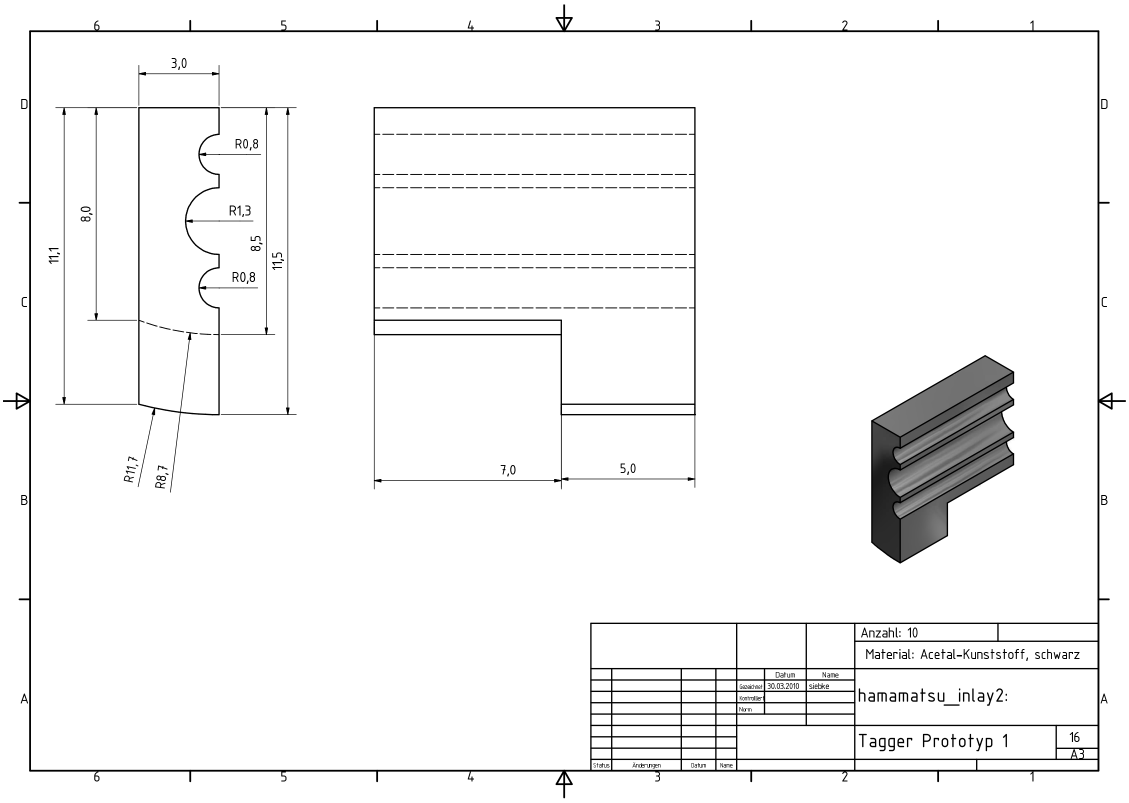

Figure 82. Part 1 of the cable lead through.

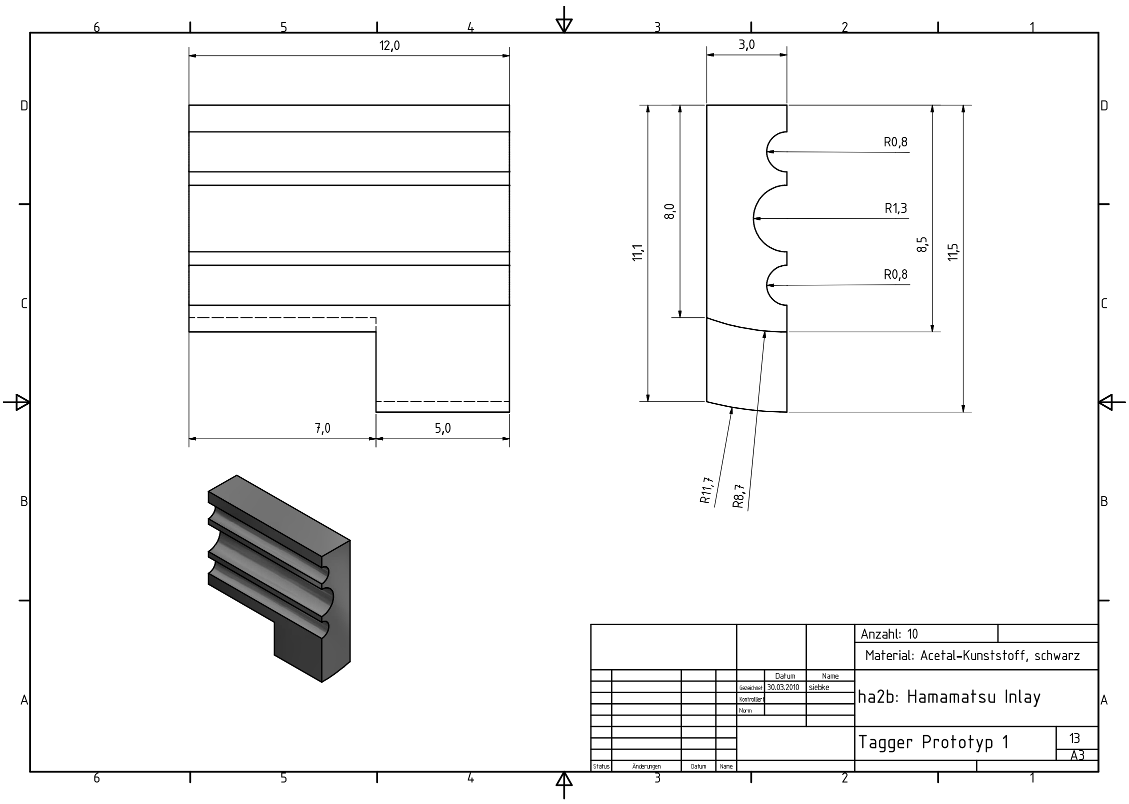

Figure 83. Part 2 of the cable lead through.

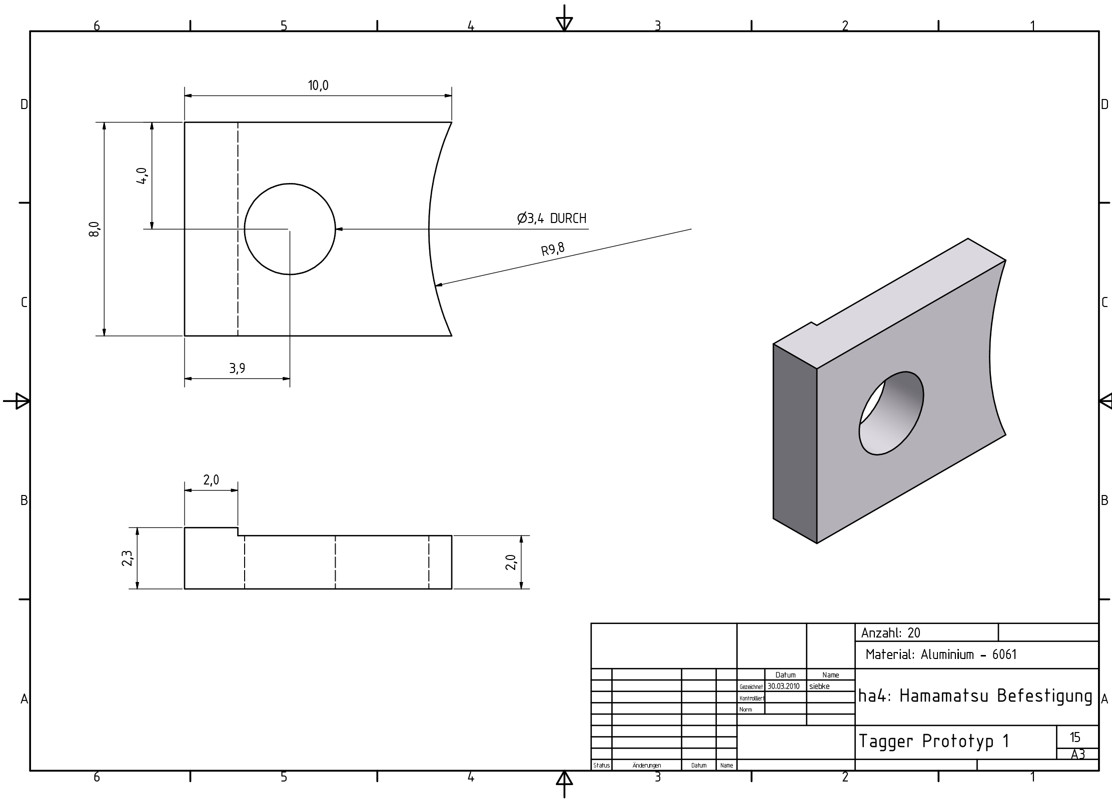

Figure 84. Clip used to fix the PMT assembly on the chassis.

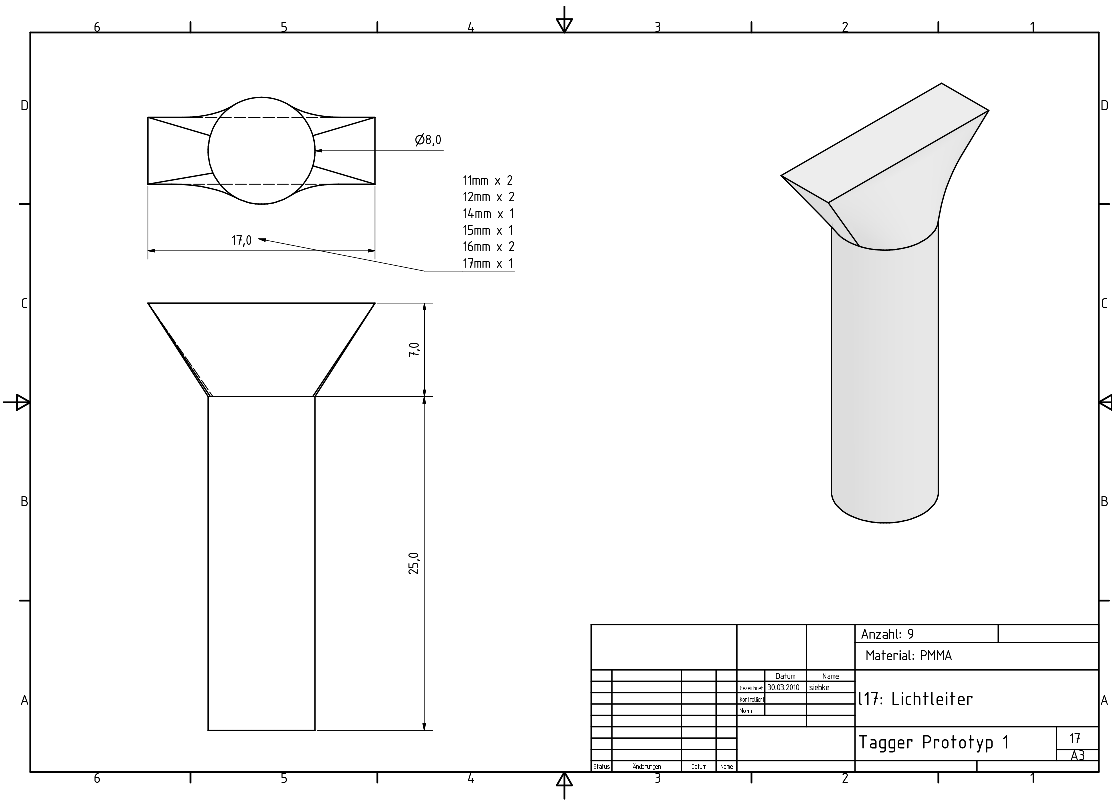

Figure 85. Light guide.

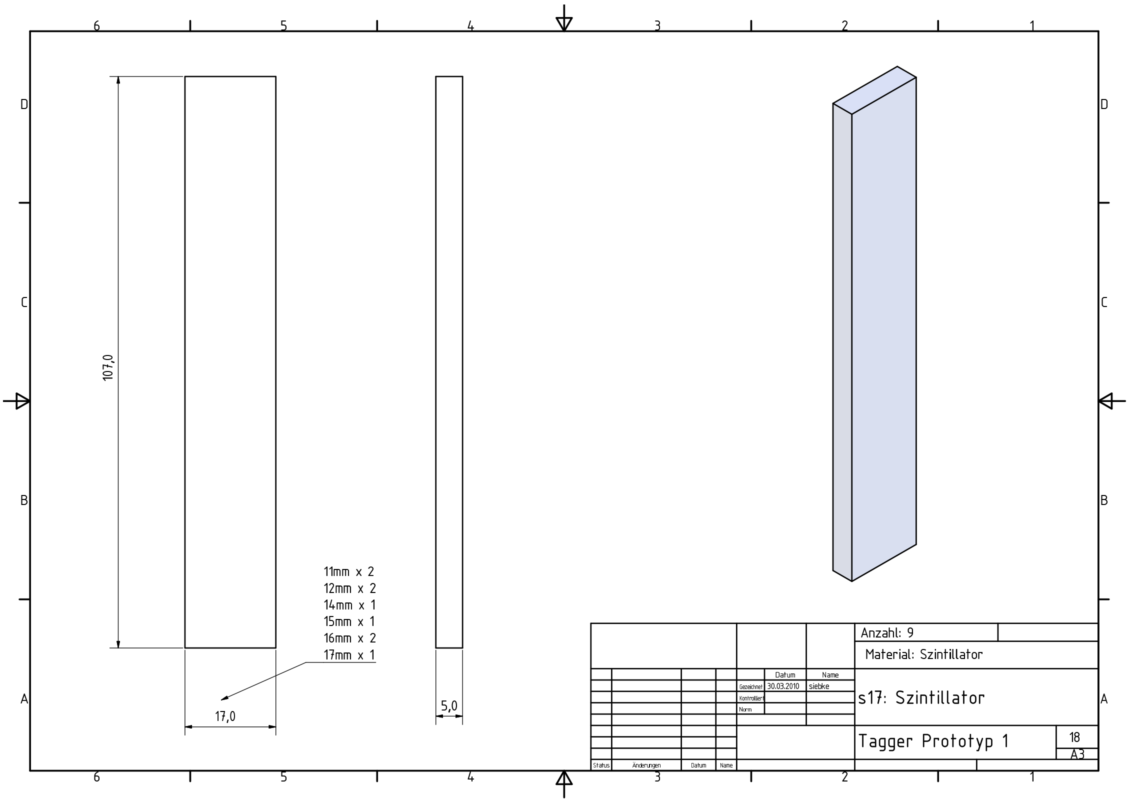

Figure 86. Scintillator bar.

Framework for the CB Tagging System

See Section 6.2.1 for a description of this construction.

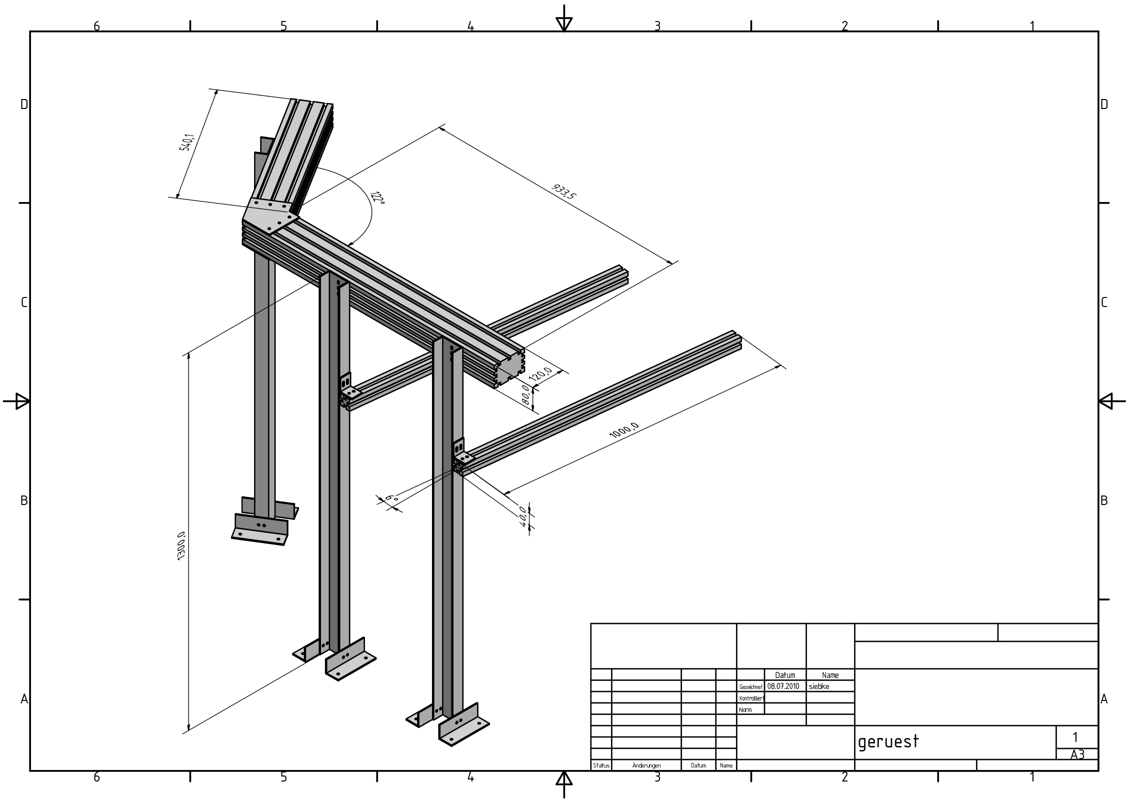

Figure 87. Framework used to mount the prototype detector behind the CB tagging system. All distances are quoted in mm.

B Triple Coincidences

See Section 7.1 for a description of these graphs.

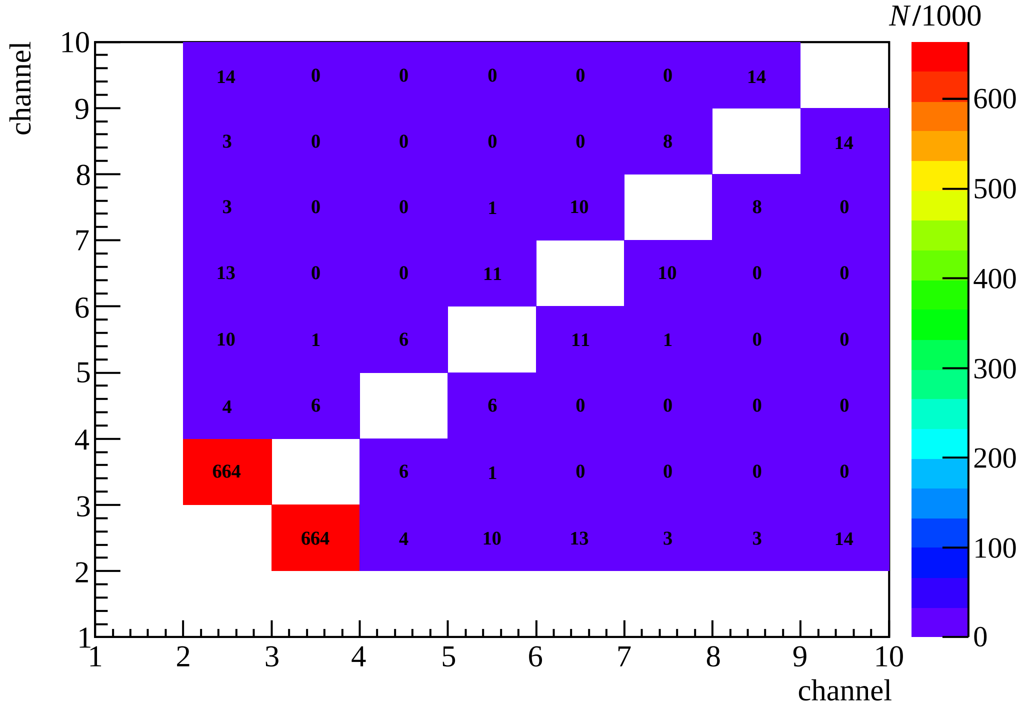

Figure 88. Exclusive coincidences of two channels and channel 1.

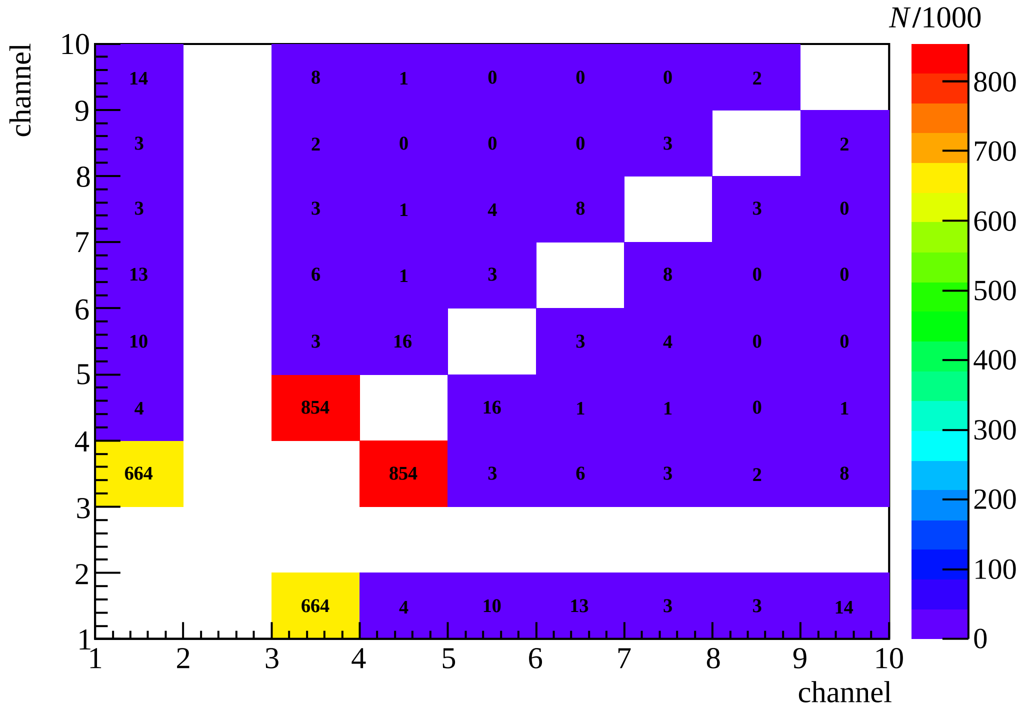

Figure 89. Exclusive coincidences of two channels and channel 2.

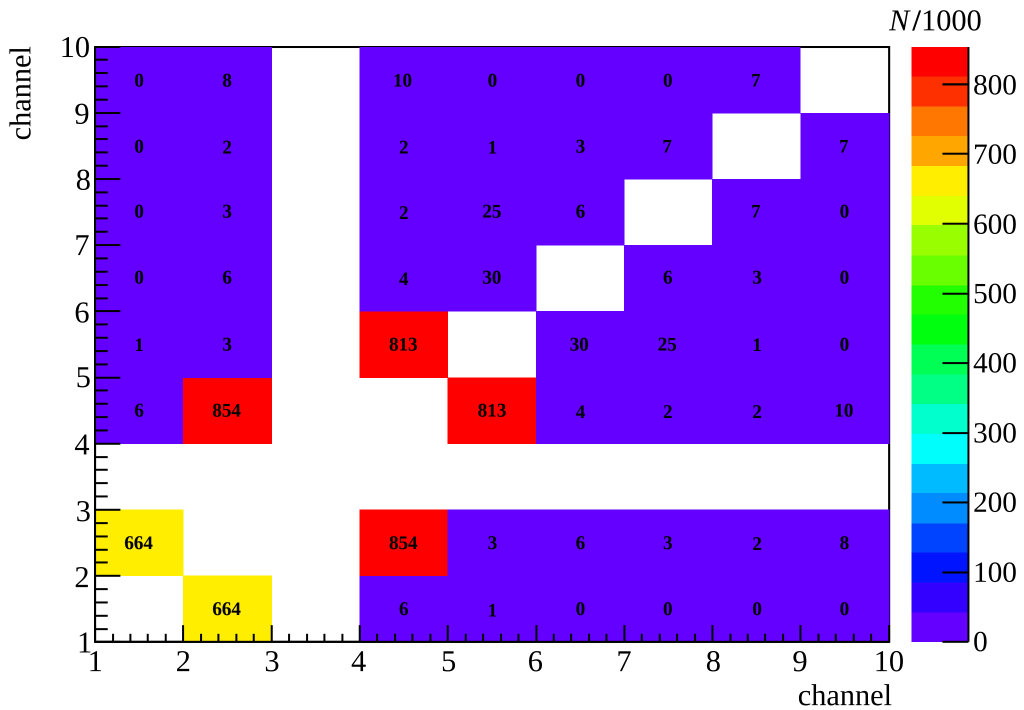

Figure 90. Exclusive coincidences of two channels and channel 3.

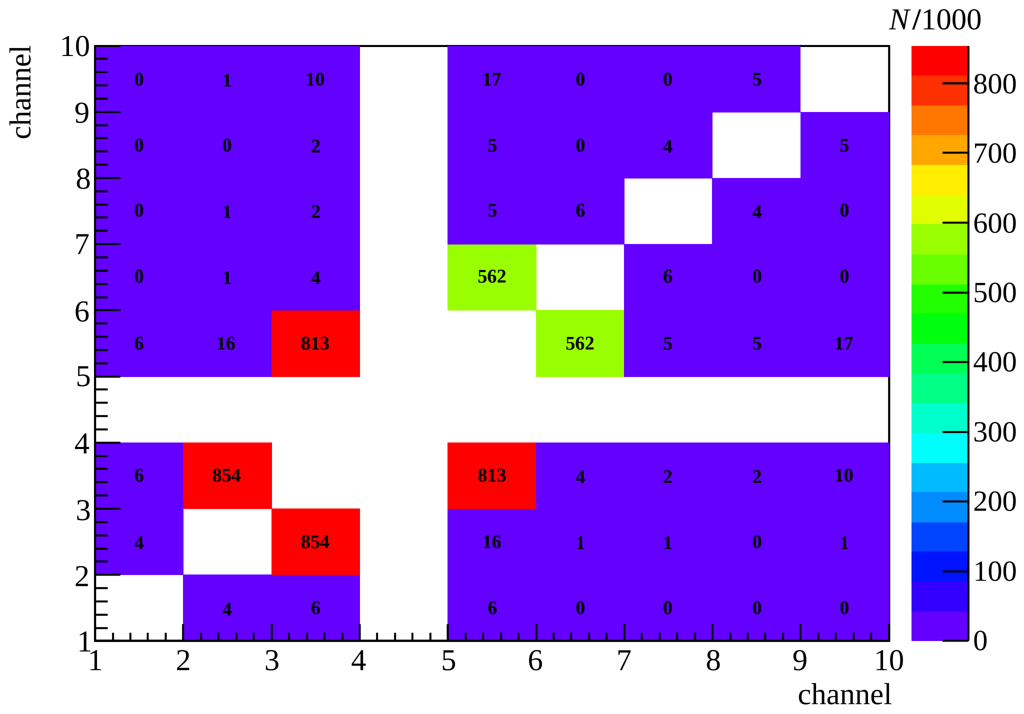

Figure 91. Exclusive coincidences of two channels and channel 4.

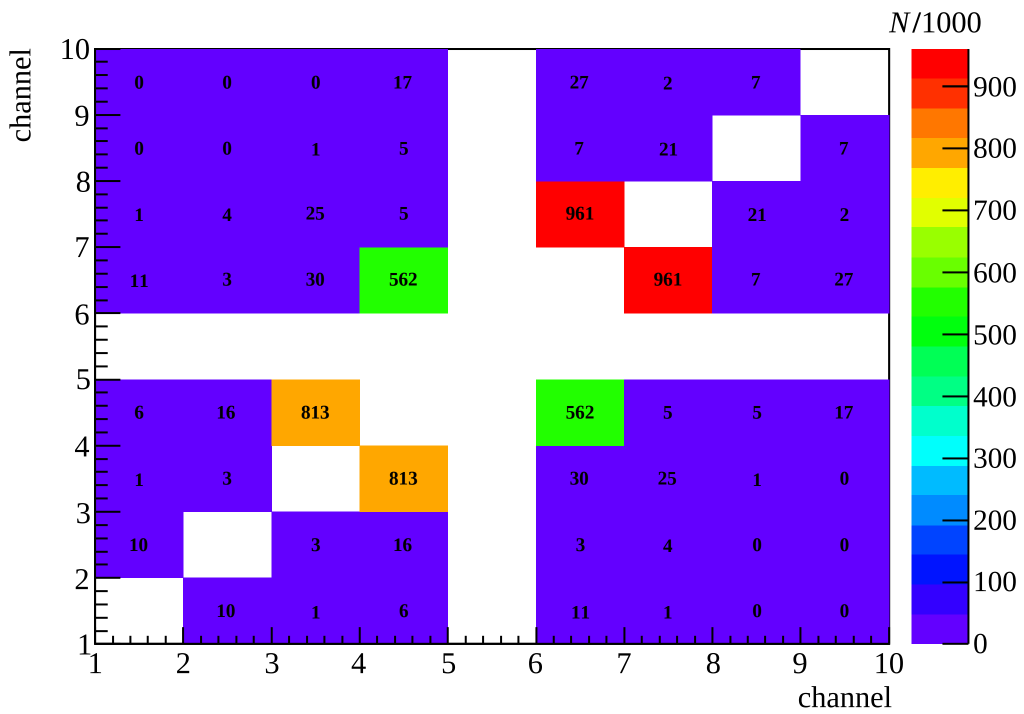

Figure 92. Exclusive coincidences of two channels and channel 5.

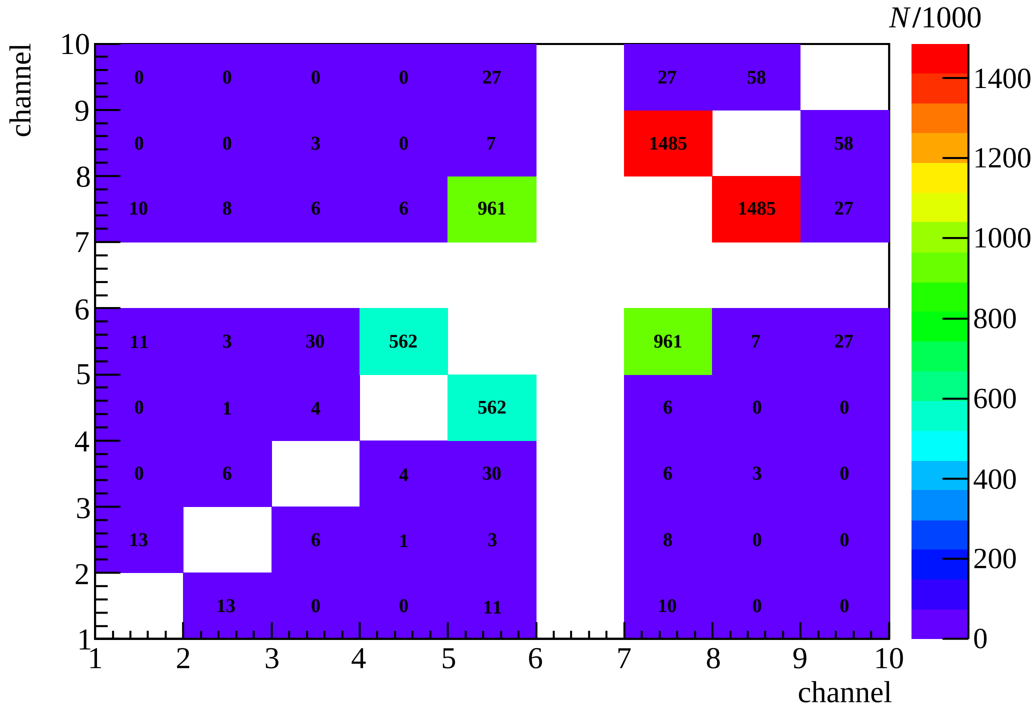

Figure 93. Exclusive coincidences of two channels and channel 6.

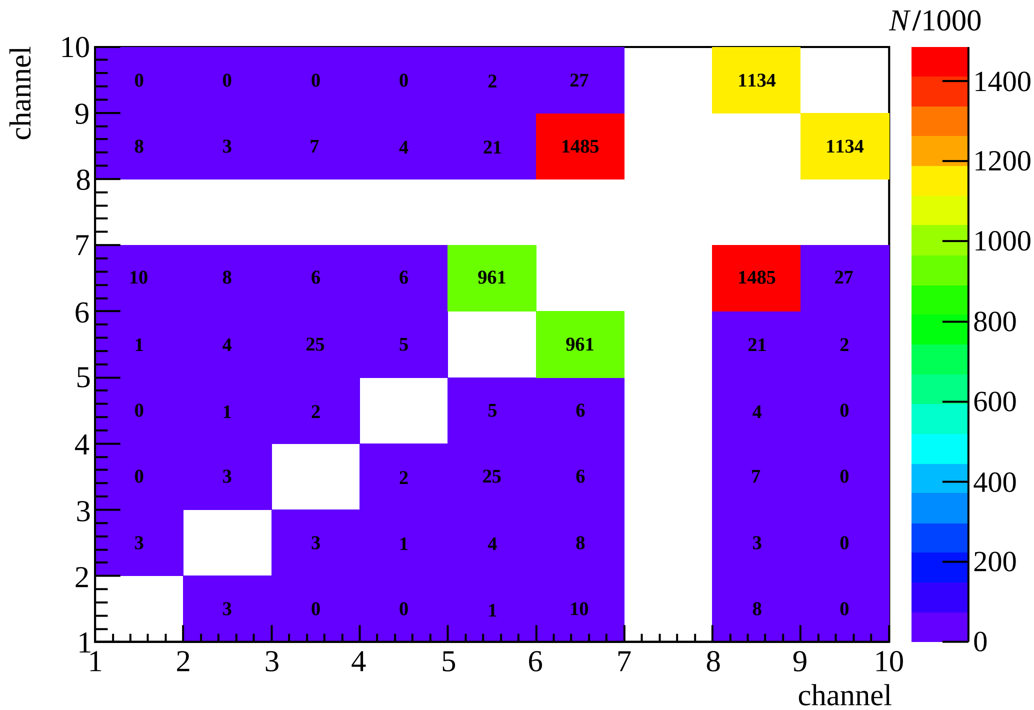

Figure 94. Exclusive coincidences of two channels and channel 7.

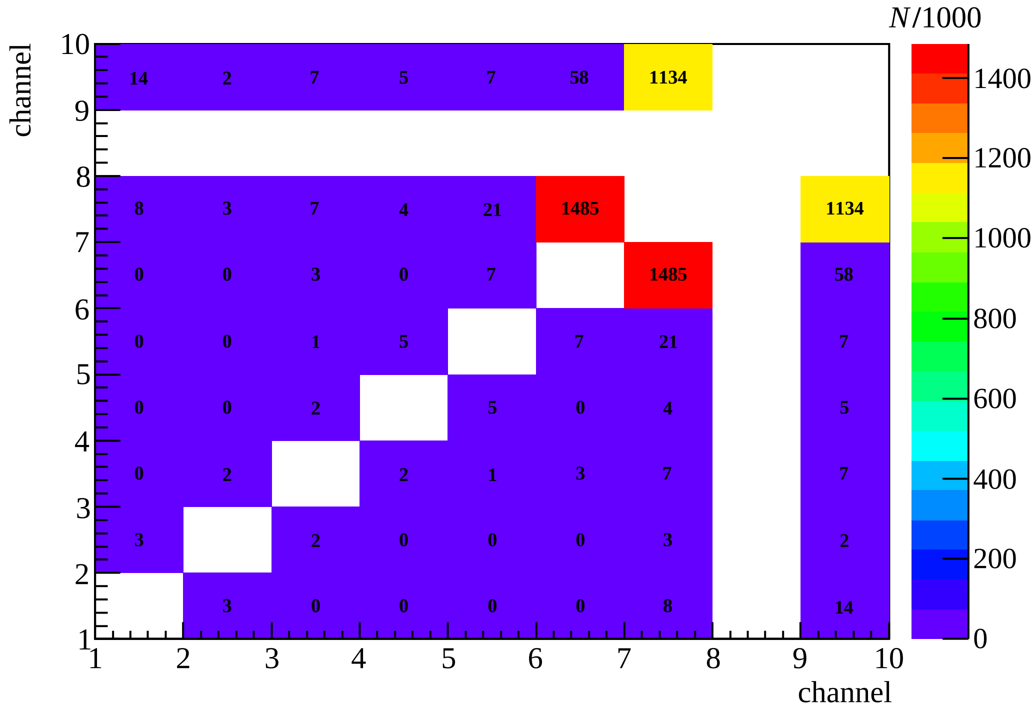

Figure 95. Exclusive coincidences of two channels and channel 8.

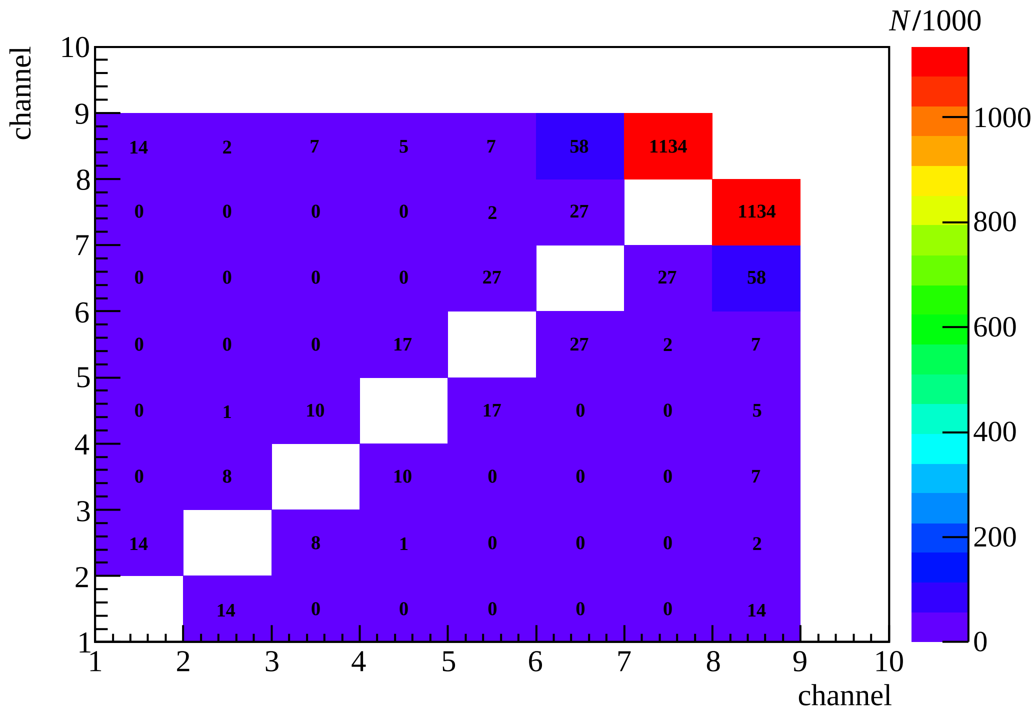

Figure 96. Exclusive coincidences of two channels and channel 9.

C Rates

See Section 7.2 for a description of these graphs.

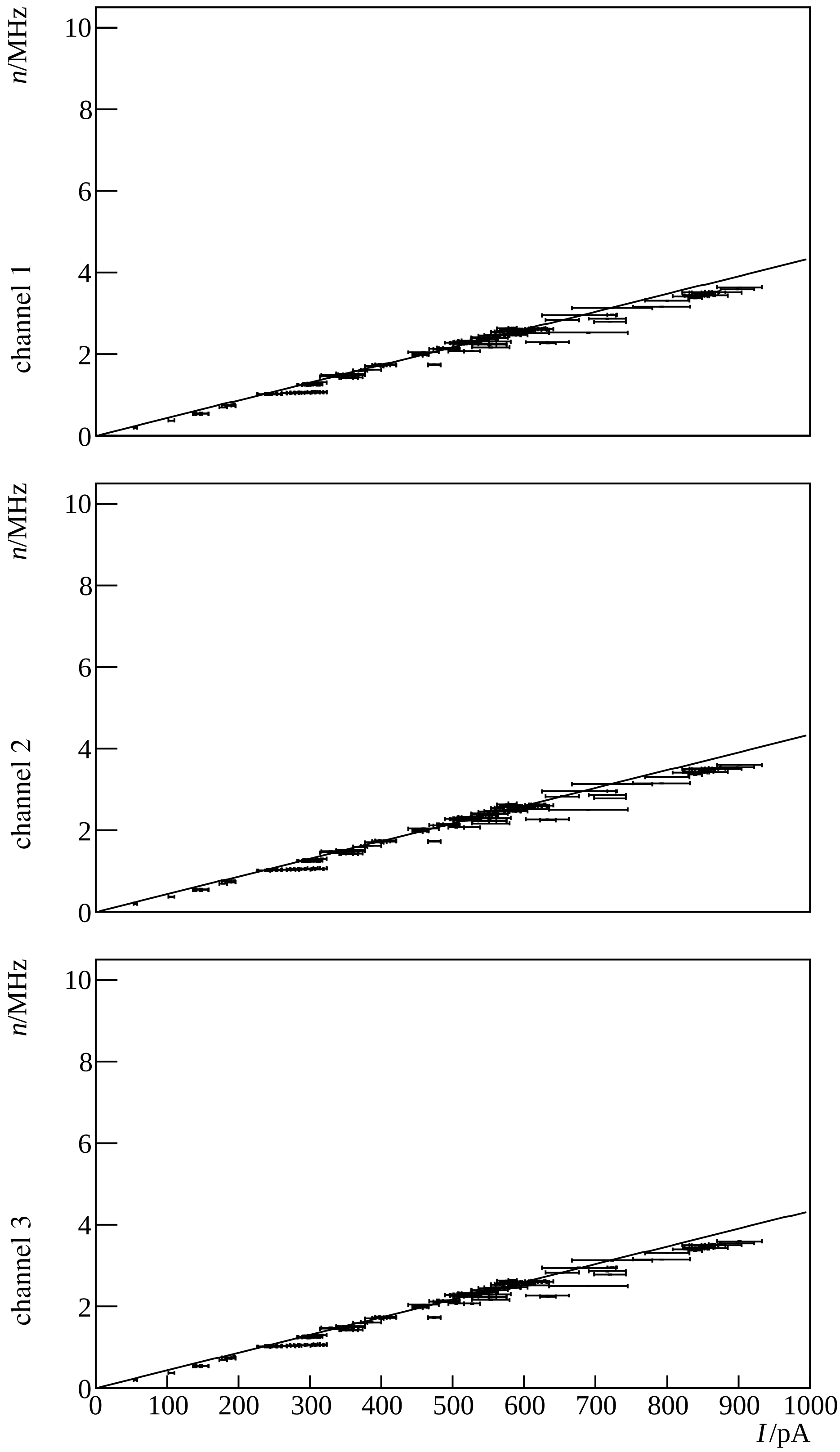

Figure 97. Scaler rate vs. current in ELSA, channel 1–3.

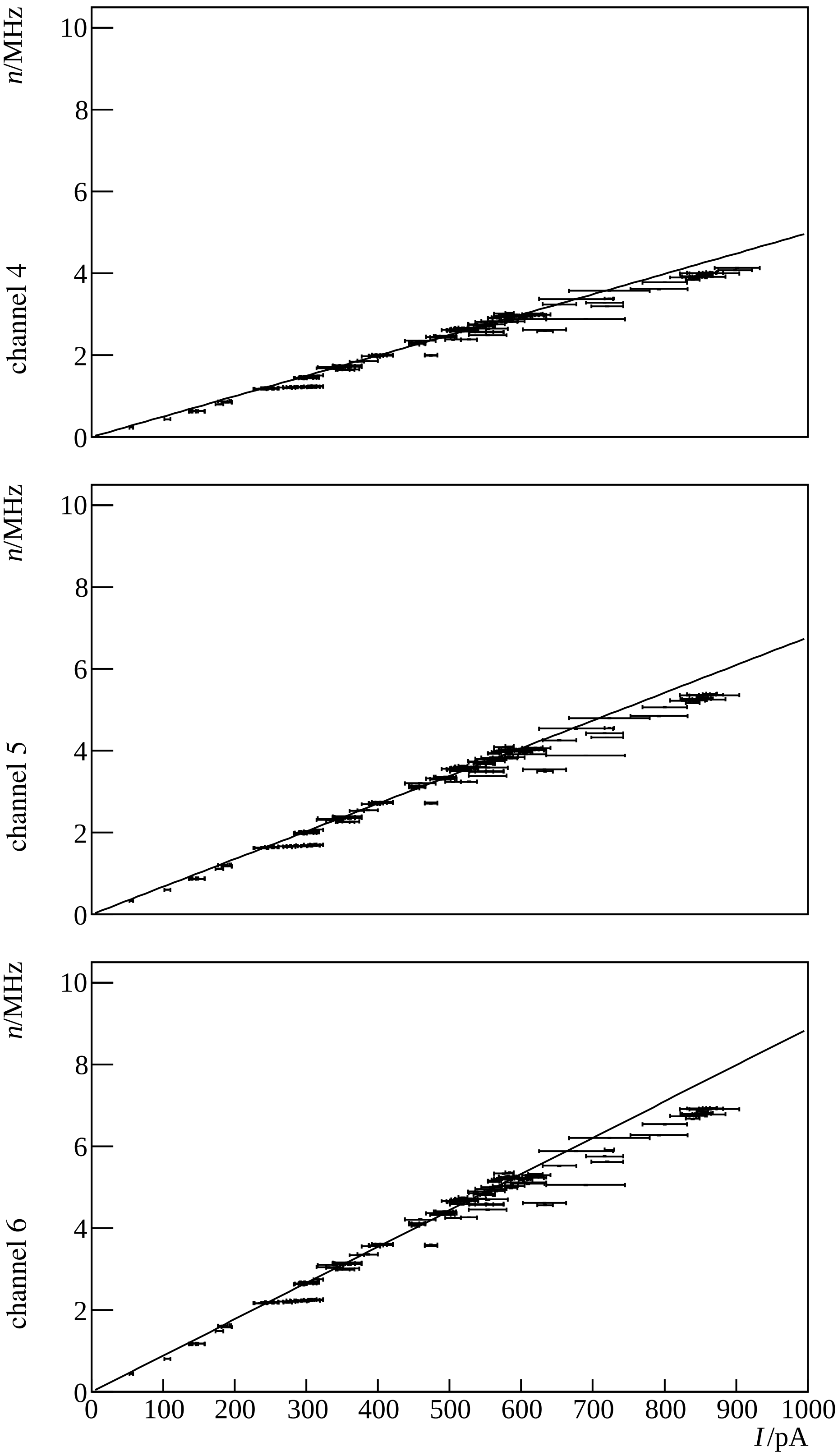

Figure 98. Scaler rate vs. current in ELSA, channel 4–6.

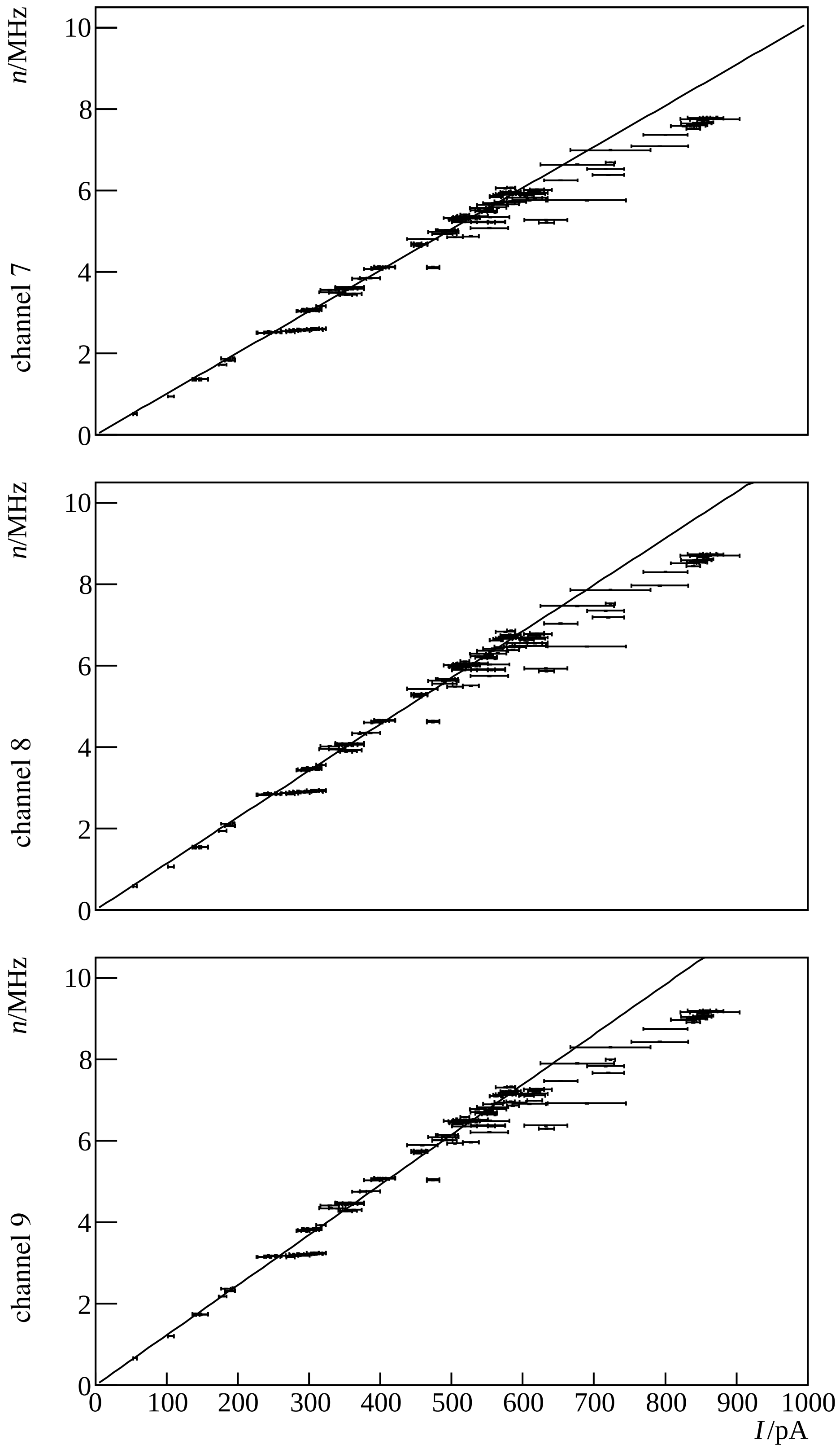

Figure 99. Scaler rate vs. current in ELSA, channel 7–9.

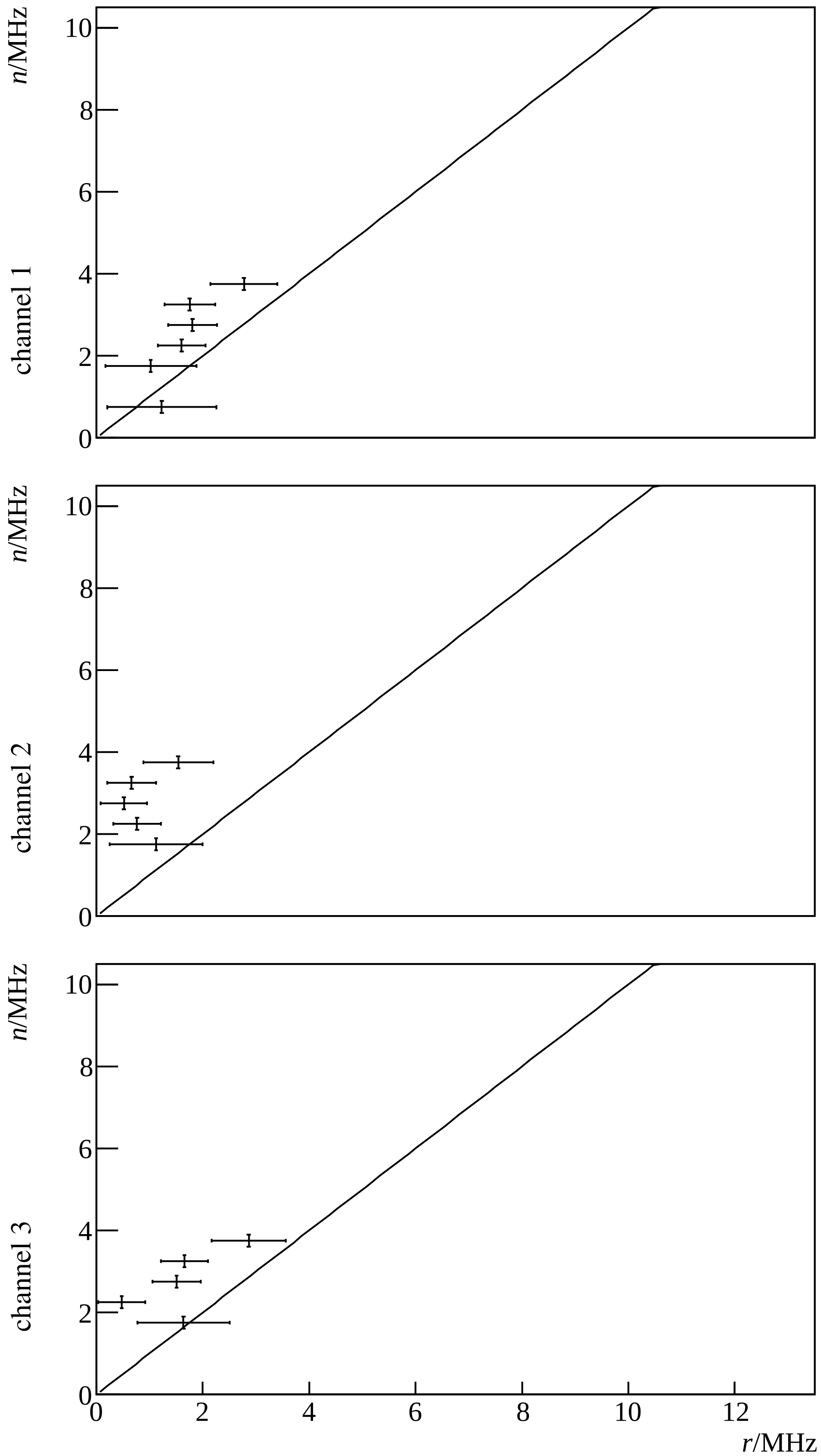

Figure 100. Scaler rate vs. reconstructed rate from the TDC, channels 1–3.

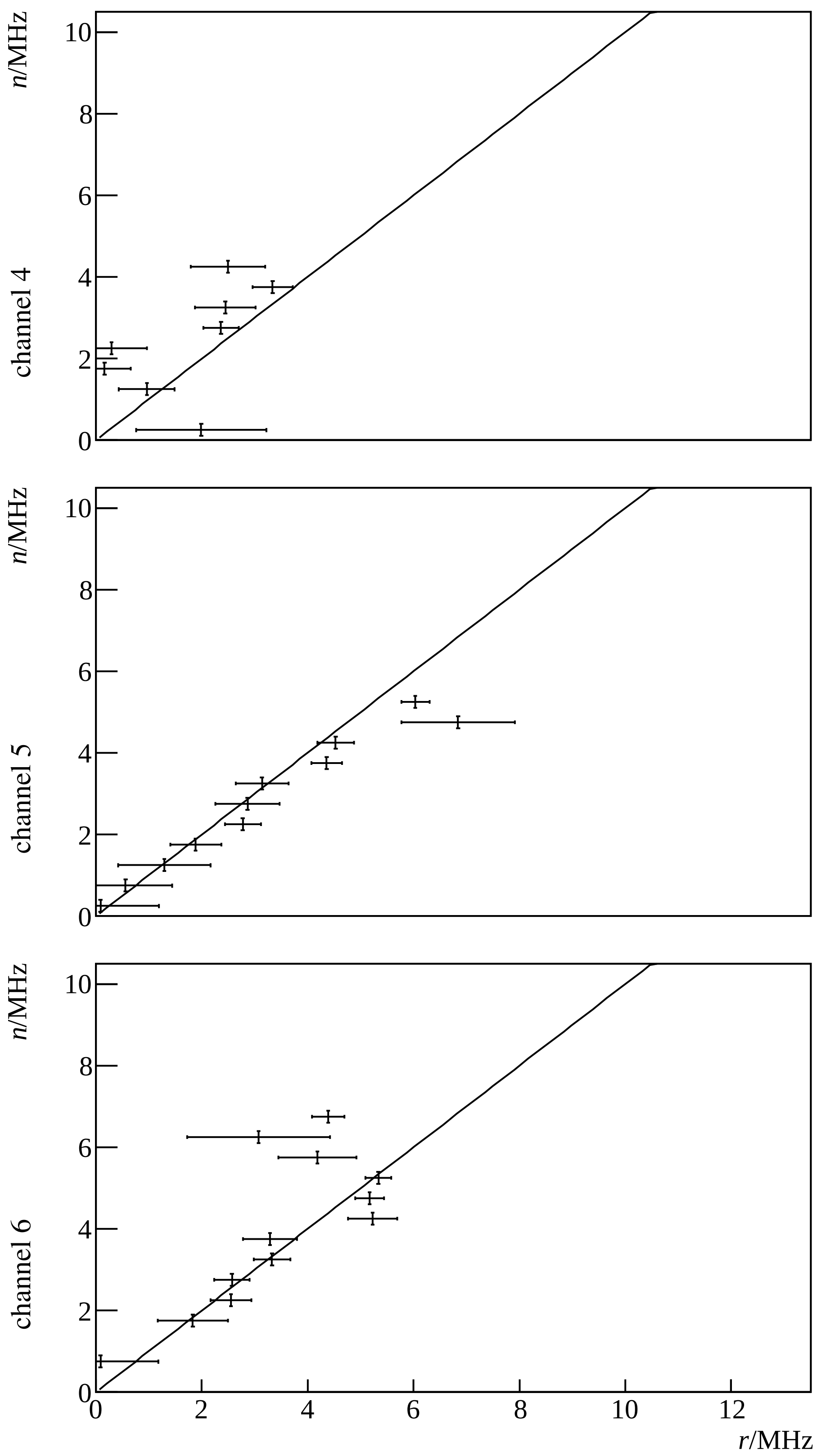

Figure 101. Scaler rate vs. reconstructed rate from the TDC, channels 4–6.

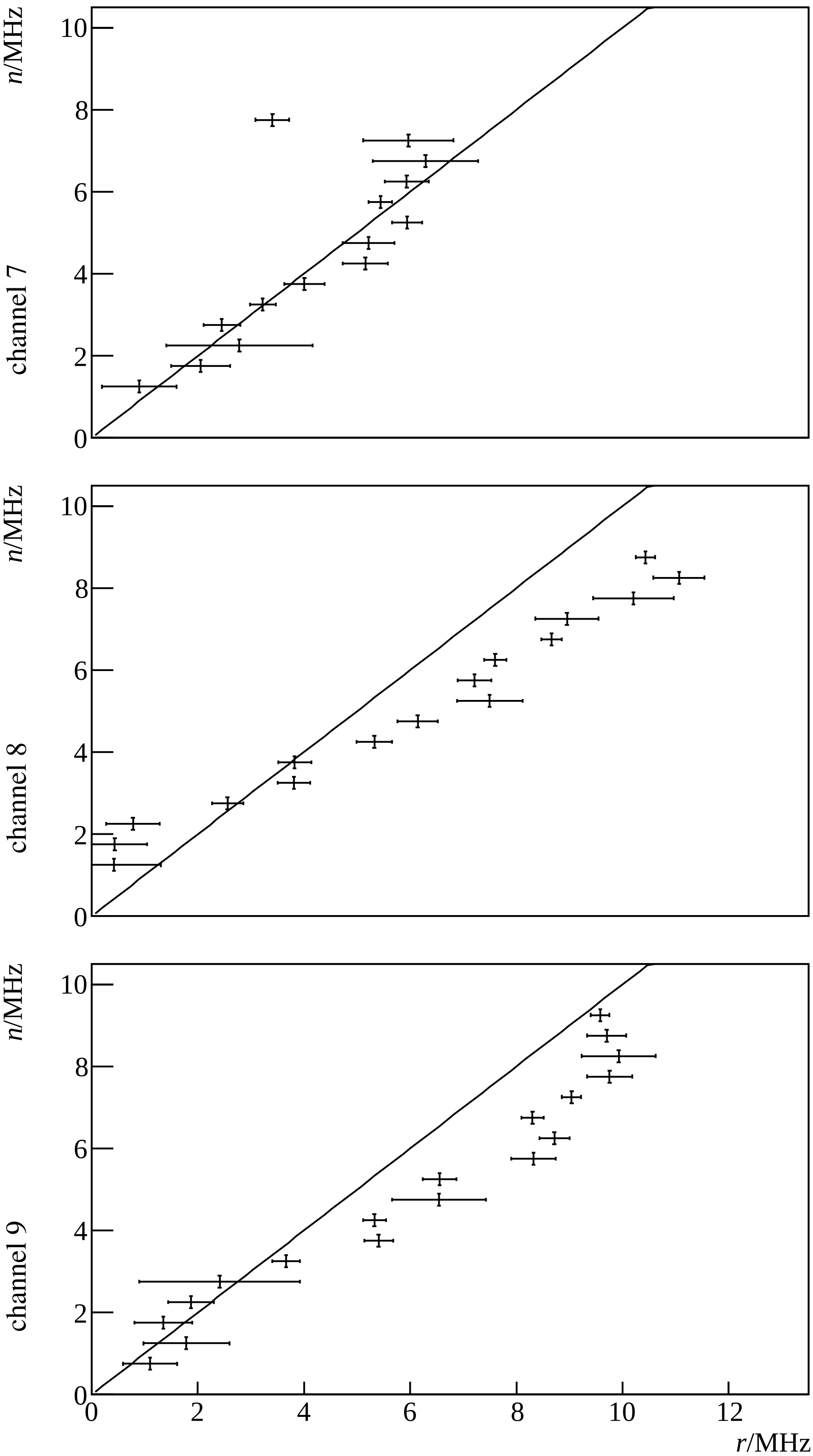

Figure 102. Scaler rate vs. reconstructed rate from the TDC, channels 7–9.

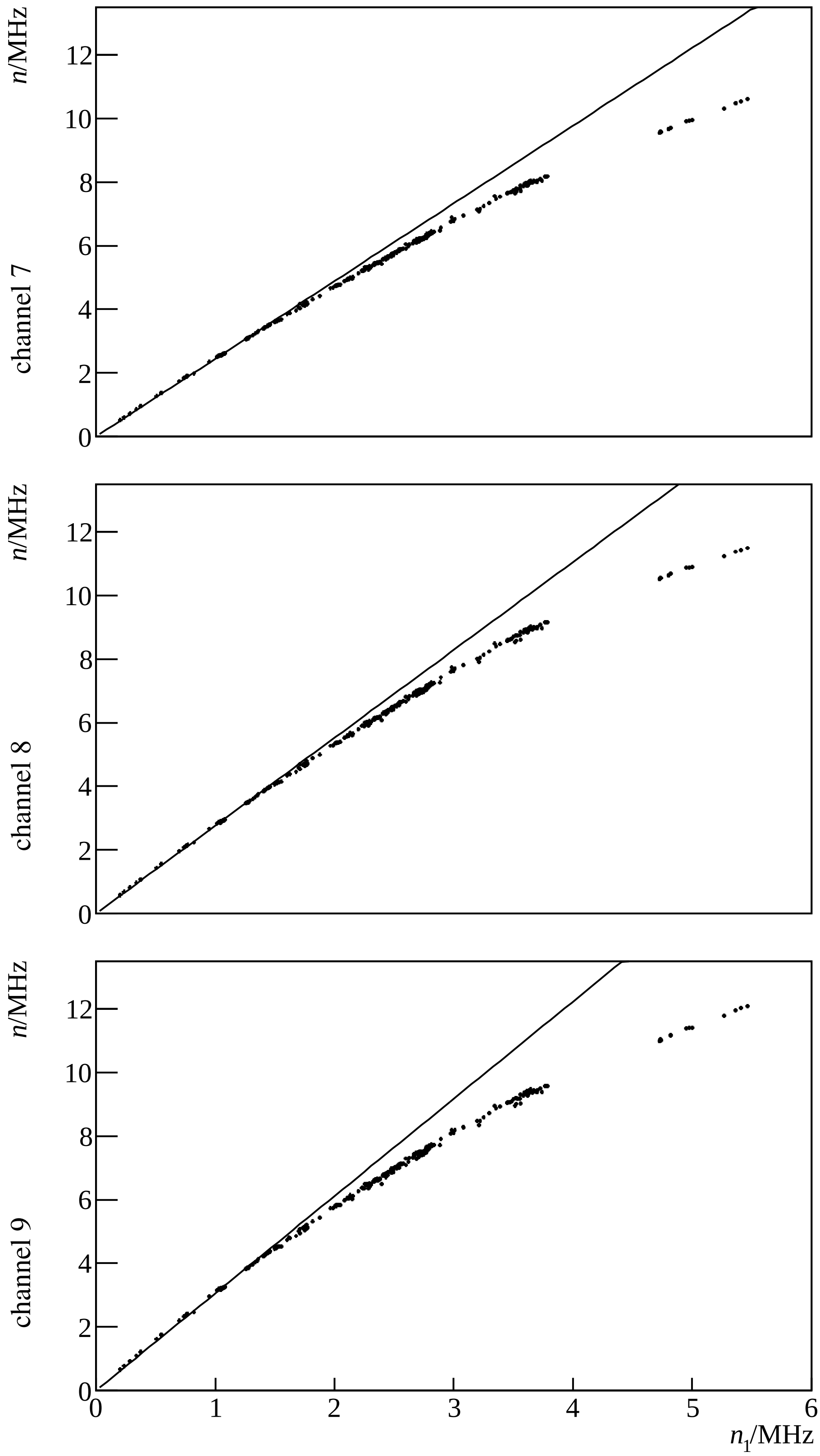

Figure 103. Scaler rate vs. scaler rate from the lowest channel, channels 7–9.

D FPGA Coincidences

See Section 7.3 for a description of these graphs.

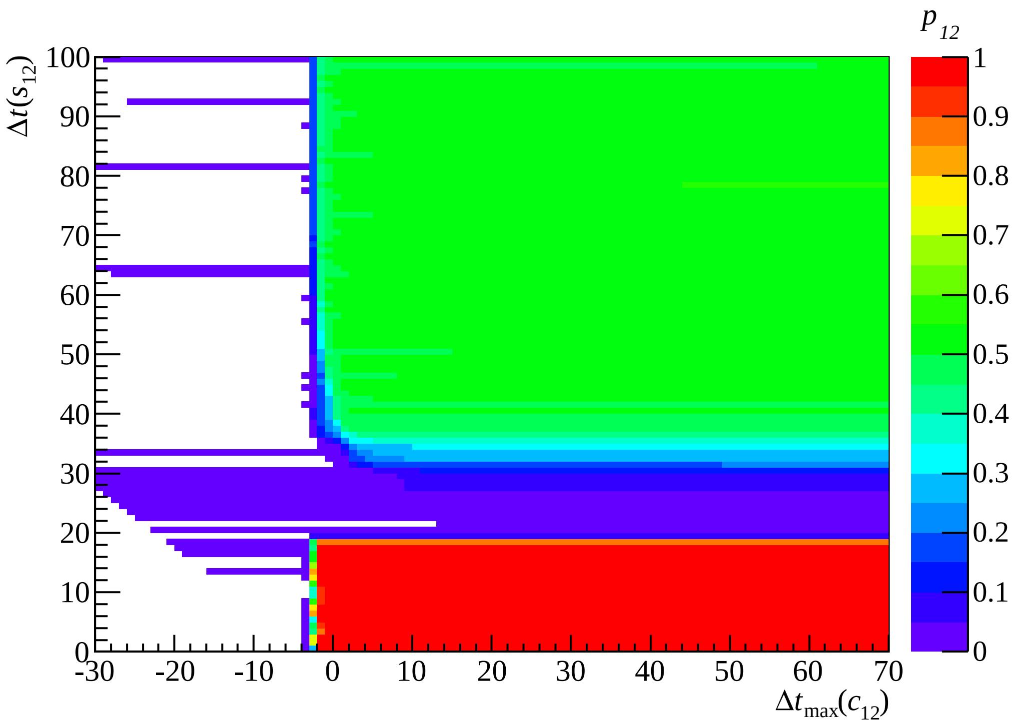

Figure 104. Probability that the FPGA recognizes a coincidence in dependence of the temporal distance (channels 1 and 2).

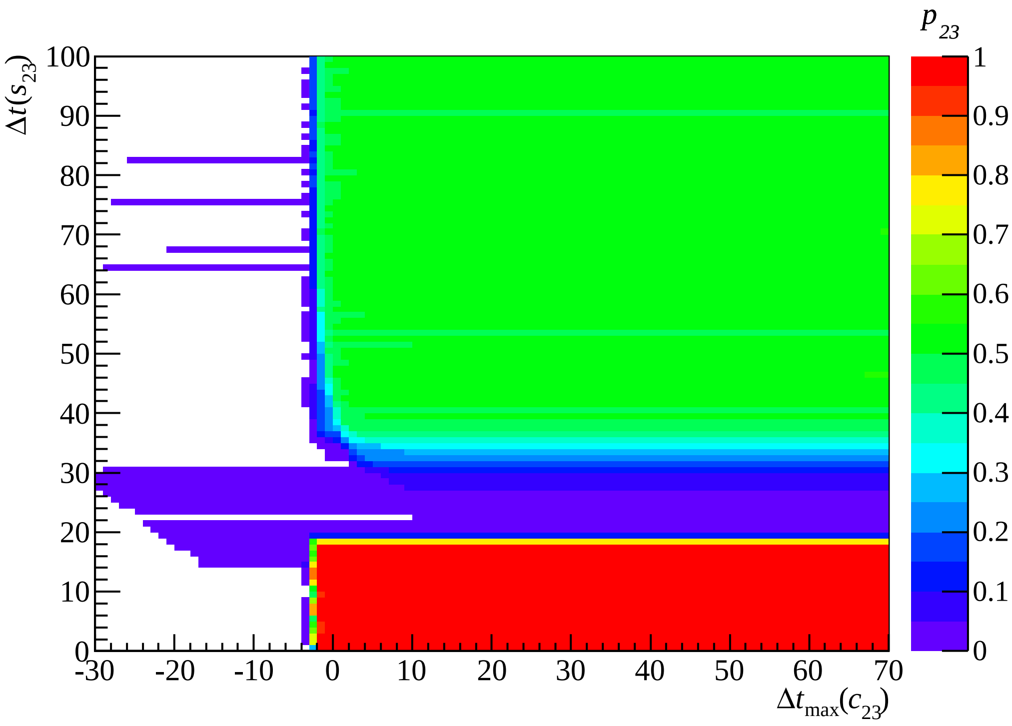

Figure 105. Probability that the FPGA recognizes a coincidence in dependence of the temporal distance (channels 2 and 3).

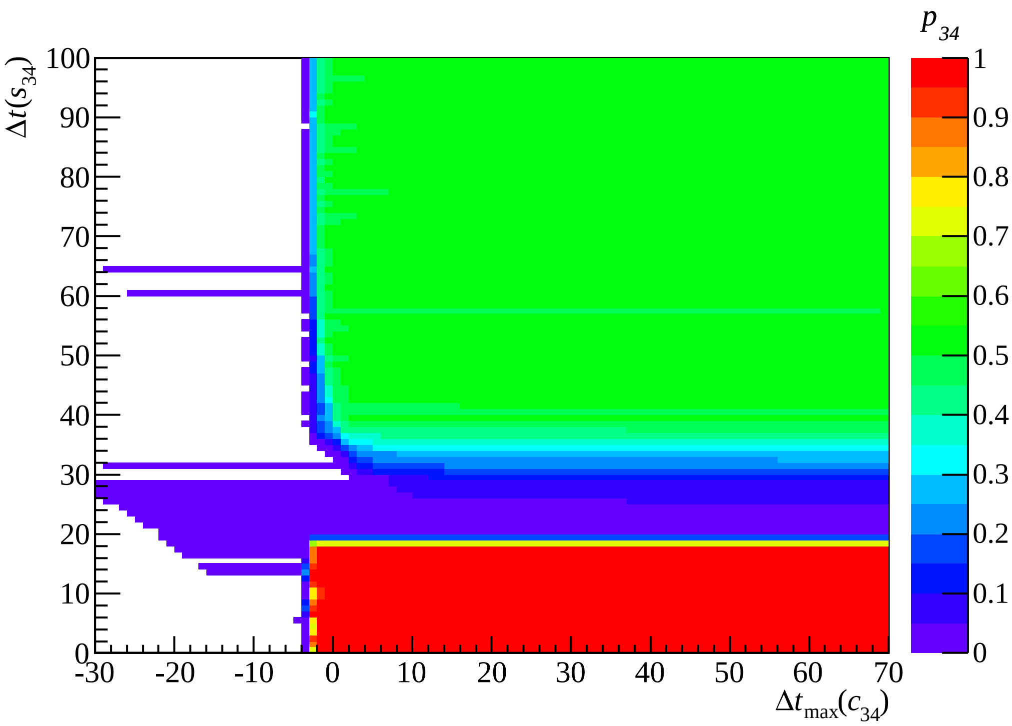

Figure 106. Probability that the FPGA recognizes a coincidence in dependence of the temporal distance (channels 3 and 4).

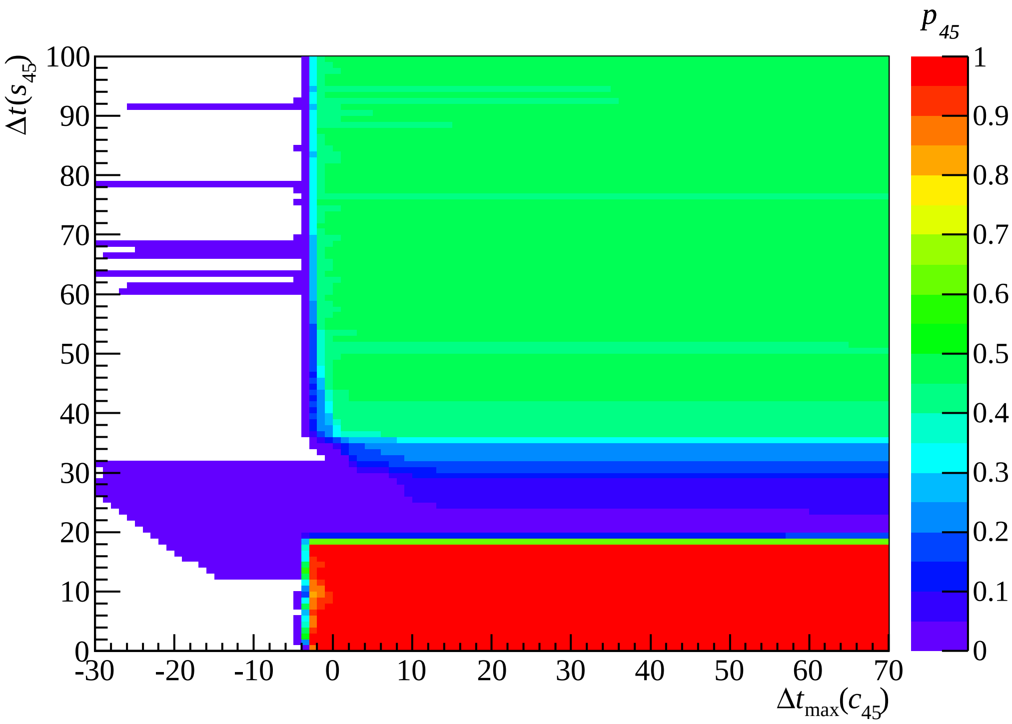

Figure 107. Probability that the FPGA recognizes a coincidence in dependence of the temporal distance (channels 4 and 5).

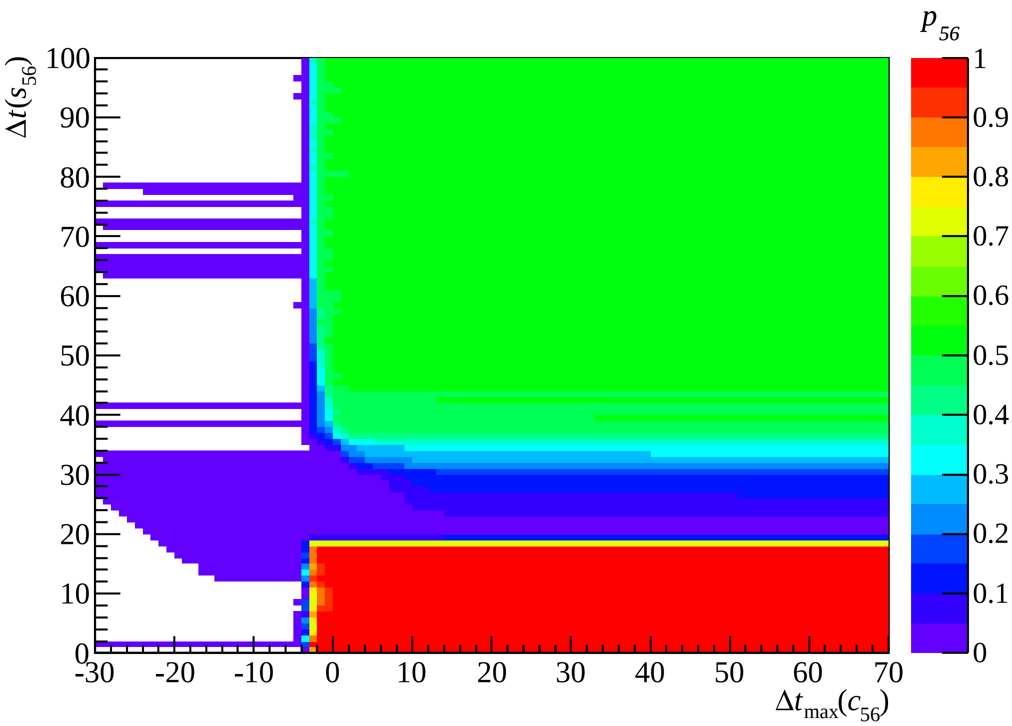

Figure 108. Probability that the FPGA recognizes a coincidence in dependence of the temporal distance (channels 5 and 6).

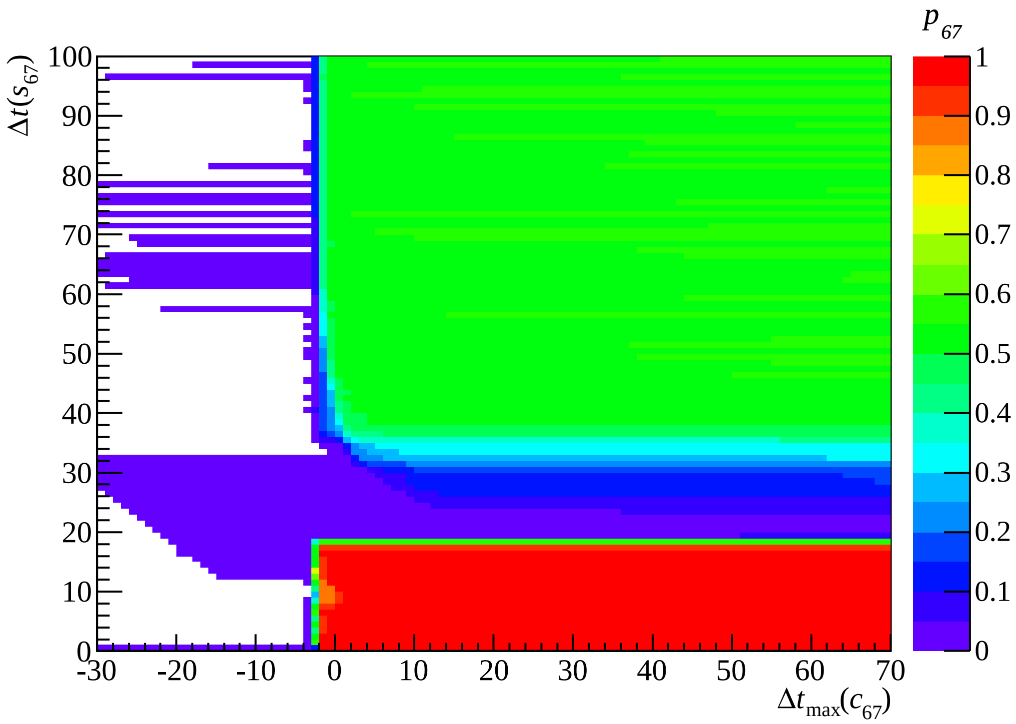

Figure 109. Probability that the FPGA recognizes a coincidence in dependence of the temporal distance (channels 6 and 7).

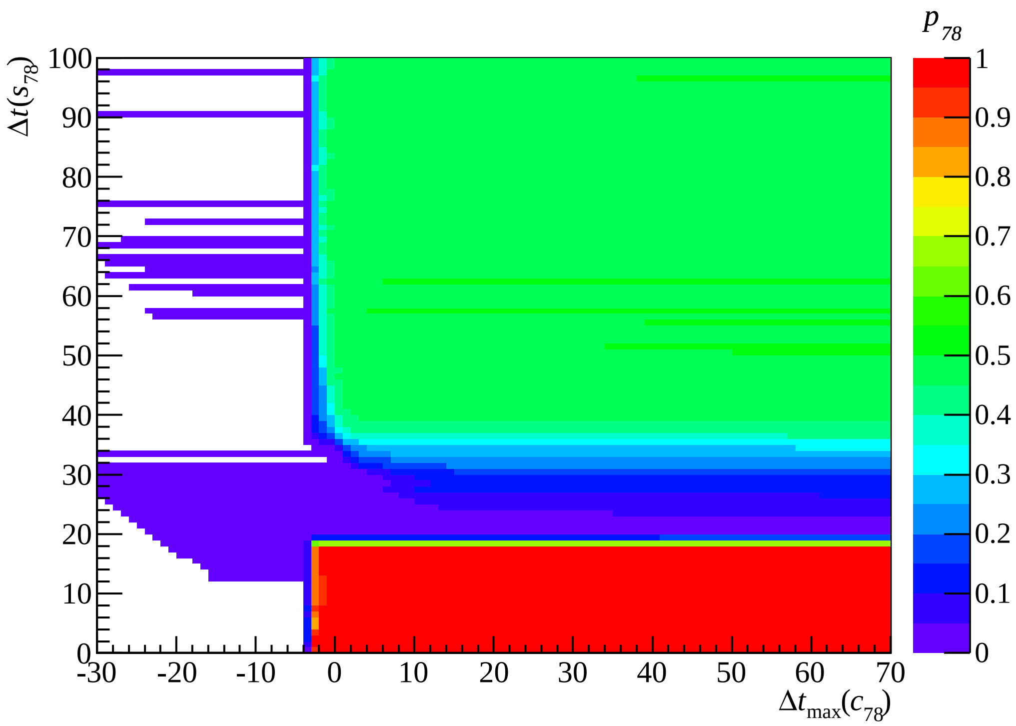

Figure 110. Probability that the FPGA recognizes a coincidence in dependence of the temporal distance (channels 7 and 8).

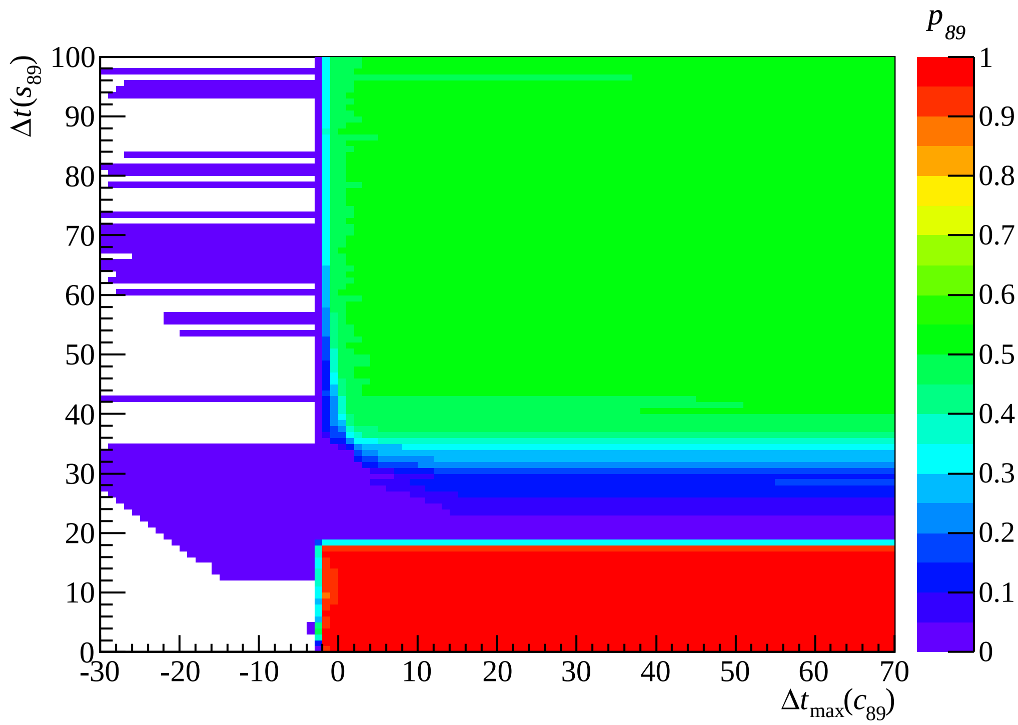

Figure 111. Probability that the FPGA recognizes a coincidence in dependence of the temporal distance (channels 8 and 9).